Dynamic Modeling of Pavements with Application to Deflection Measurements

Madsen, Stine Skov

Publication date:
2016

Document Version
Publisher's PDF, also known as Version of record

Dynamic Modeling of Pavements with Application to Deflection Measurements

PhD Thesis

$$(EIv'')'' = q - \rho A\ddot{v}$$

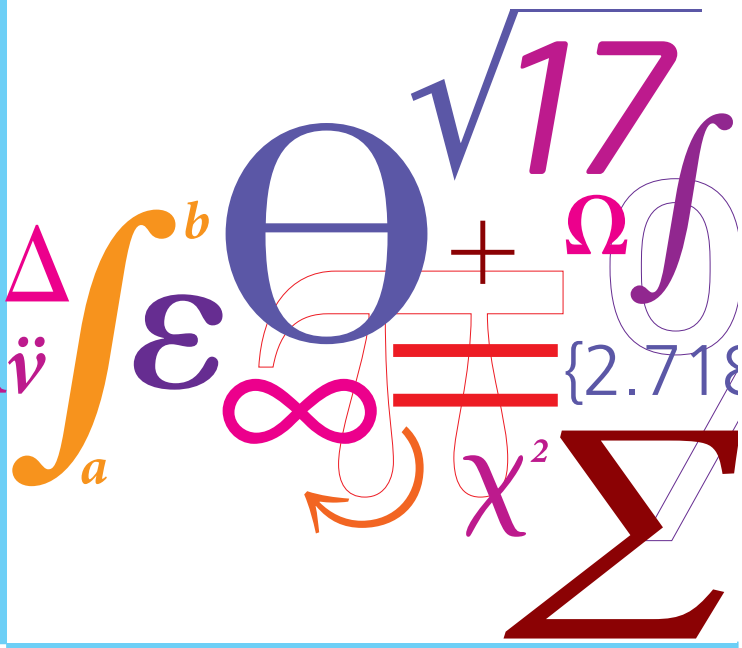

Stine Skov Madsen
DCAMM Special Report No. S210
July 2016

DTU Mechanical Engineering
Department of Mechanical Engineering

Dynamic Modeling of Pavements with Application to Deflection Measurements

Stine Skov Madsen

Kongens Lyngby 2016

Technical University of Denmark
Department of Mechanical Engineering
Nils Koppels Allé, building 404,
2800 Kongens Lyngby, Denmark
Phone +45 4525 1960
www.mek.dtu.dk

Preface

This thesis is submitted in partial fulfilment of the requirements for acquiring the Ph.D. degree in mechanical engineering at the Technical University of Denmark (DTU). The first part of the Ph.D. project was carried out at the department of Civil Engineering (DTU BYG), Geotechnics and Geology, at DTU in the period July 1st 2012 - December 31st 2015 (interspersed with a maternity leave of 10 months). The project was continued at the department of Mechanical Engineering (DTU MEK), Solid Mechanics, at DTU from January 1st 2016 - July 19th 2016. Supervisors was Associate Professor Ole Hededal (in the period July 2012 to January 2014) and Associate Professor Björn Johannesson (in the period November 2014 - December 2015) at the department of Civil Engineering, and Professor Steen Krenk (in the period July 2012 to January 2015) and Associate Professor Niels Leergaard Pedersen from January 2016 until the end of the study at the department of Mechanical Engineering. Matteo Pettinari took part in the project as Post Doc at the department of Civil Engineering from February 2014 to march 2015.

I am very greatful to my supervisors for their support in the various periods of the project; especially Steen Krenk for valuable contributions to the project and for always taking time for in depth discussions. I want to thank my supervisor during the past six months, Niels Leergaard Pedersen for his support and guidance to complete my work and collect it into this thesis. I would also like to thank Associate Professor Eyal Levenberg for providing essential contributions and feedback to our collaborative work. Furthermore, I would like to thank Matteo Pettinari for valuable discussions and ideas during his time as a Post Doc, and for providing support and help with experimental testing after he switched job to work for the Danish Road Directorate.

The Ph.D. has been funded by the Innivation Fund Denmark through the grant 'High-speed Pavement Assessment Tool for Better and Safer Roads' and DTU. The project was carried out in close collaboration with Dynatest and I would like to thank my colleagues there, in particular the RWD team: Mathias Bækbo Andersen, Jack Larsen,

Søren Rasmussen and Albert Navarro Comes. It has been a pleasure to work with you and to be a part of the team. I would like to thank Albert for conducting the FWD experiments used in this work.
A part of the research project was carried out at the Florida Department of Transportation (FDOT) during the fall 2013. In this regard I would like to thank James Green and his team for being very generous hosts. It was a great experience and I learned a lot about pavement testing and measurement equipment. During the three months stay I regularly visited the University of Florida and I would like to express my gratitude to Professor Reynaldo Roque for introducing me to his section of pavement engineering, and for letting me participate in his lectures. I would also like to thank my colleagues from the Dynatest Starke office for their warm welcome and introduction to the company products. A special thanks to Bill Beck for helping me with many practical things during the first weeks of my stay in Florida. I would also like to express my gratitude to Regis Carvalho for showing great interest in my project and sharing his knowledge and ideas with me.
A special thanks to Per Ullidtz, for sharing his great knowledge with me and for inspirational and motivating discussions.
Finally, I would like to express my sincere gratitude to my family; in particular my husband for supporting me during the entire period of my Ph.D. and for valuable discussions and ideas.

Kgs. Lyngby, July 19th 2016.

Stine Skov Madsen

Summary (English)

Pavement surface deflection measurements are the primary means of evaluating the bearing capacity of a pavement. The most common type of device used for measuring pavement surface deflections is the Falling Weight Deflectometer (FWD). However, increasing attention has been given to the Rolling Wheel Deflectometer (RWD) type of device due to its ability to measure deflections continuously while driving at traffic speed. To be able to properly interpret deflection measurements from an RWD device, more knowledge about the structural behavior of a pavement when subjected to transient dynamic loads moving with different speeds is needed.

In this thesis a new Finite Element formulation for transient dynamic loading of a layered half space is developed. Equations are derived in 2D and 3D and include efficient absorbing boundary conditions in the form of the Perfectly Matched Layer (PML) which ensures capability of long time simulations without disruptions from the boundaries. The equations are formulated in a moving frame of reference such that the domain is following the load, which ensures that the size of the model is kept small regardless of simulation time frame.

A parametric study for finding optimal PML parameters is conducted [P1]. The efficiency of the PML formulation is tested in a half space and in a layered halfspace. The effect of load speed is investigated as well as the influence of modulus ratio between surface layer and the underlying soil for different load speeds. Wave propagation is illustrated for various load speeds in both 2D and 3D. The differences in response magnitude and attenuation rate of 2D and 3D waves are illustrated as well.

The model is applied for backcalculation of mechanical properties from FWD experiments with load-time histories of various pulse durations and load magnitudes [P2]. For this purpose, a method for backcalculation of layer moduli and damping as well as geometric nonlinearity in the subgrade is developed.

Summary (Danish)

Bæreevnen af en vejbelægning vurderes primært ved måling af overfladenedbøjningen af vejbelægningen. Den mest anvendte metode til bestemmelse af nedbøjningen er faldlodsmåling (Falling Weight Defelctometer, FWD). Opmærksomheden rettes imidlertid i stigende grad mod et måleinstrument (Rolling Wheel Deflectometer, RWD), som måler nedbøjningen kontinuerligt under kørsel ved trafikhastighed. For at kunne fortolke deflektionsmålingen fra en RWD korrekt, er det nødvendigt at vide hvordan vejen opfører sig under dynamisk belastning ved forskellige hastigheder.

I denne afhandling udvikles en ny Finite Element-formulering til simulering af dynamisk belastning af et lagdelt halvrum. Ligningerne udledes i 2D og 3D og omfatter effektivt absorberende randbetingelser i form af Perfectly Matched Layer (PML), som sikrer at der kan simuleres ubegrænset i tid uden indvirkning fra uønskede randfænomener. Ligningerne er formuleret i en bevægende referenceramme, således at domænet følger belastningen. Dette sikrer, at grid-størrelsen holdes nede, uagtet simulationens længde.

Et parametrisk studie udføres for at bestemme optimale PML-parametre [P1]. Effektiviteten af PML-formuleringen testes i et halvrum og i et lagdelt halvrum. Effekten af forholdet mellem stivheden i overfladelag og den underliggende jord ved forskellige hastigheder af lasten er undersøgt. Bølgeudbredelse illustreres for forskellige hastigheder af lasten i både 2D og 3D. Forskelle i respons-størrelse og -dæmpningsgrad af bølger i 2D og 3D er ligeledes illustreret.

Modellen anvendes til estimering (backcalculation) af mekaniske egenskaber af en vejbelægning ud fra FWD-eksperimenter med belastninger af forskellige impulstider og størrelsesorden [P2]. Til dette formål er der udviklet en metode til backcalculation af lagenes E-moduler og dæmpningsparametre samt den geometriske ikke-linearitet i bærelaget.

Publications

The following publications are part of this thesis

P1 Stine S. Madsen and Steen Krenk. Perfectly Matched Layer (PML) for transient wave propagation in a moving frame of reference. Submitted.

P2 Stine S. Madsen and Eyal Levenberg. Dynamic backcalculation with different load-time histories. Submitted.

The following publication is not appended in this thesis because the topic is more widely covered in [P1].

- Stine S. Madsen, Steen Krenk and Ole Hededal. Perfectly Matched Layer (PML) for transient wave propagation in a moving frame of reference. In *Proceedings of the 4th Eccomas Thematic Conference on Computational Methods in Structural Dynamics and Earthquake Engineering*, pages 4379-4388. Athens, Greece, 2013.

List of Figures

List of Tables

Contents

Chapter 1

Introduction

Pavement surface deflection measurements are the primary means of evaluating the state of a pavement structure. Many characteristics of a pavement can be determined by measuring the deflection response to a load applied to the pavement surface. The magnitude and shape of pavement deflections as response to an applied load is a function of loading, layer stiffness and geometry as well as temperature and viscosity. Furthermore, pavement deflection measurements are non-destructive and can thus be performed without destroying the pavement.

Deflection measurements can be used to determine the pavement bearing capacity. The bearing capacity of a pavement is an important performance parameter since it is acting as a direct indicator of the remaining service life of the pavement. Maintenance and rehabilitation costs can be reduced by frequently estimating the bearing capacity of pavements and use this information in the process of maintenance planning. Estimation of the remaining lifetime of a pavement enables preventive measures to be introduced, which is much more economical than carrying out repairs once serious damage has occurred (see Figure 1.1).

The bearing capacity of a pavement is estimated by using measured pavement surface deflection as input to a parameter estimation method, often referred to as a so-called backcalculation method. The backcalculation method is an iterative procedure wherein model-generated deflections are matched against measured deflections by adjusting the mechanical properties of a modeled pavement structure. The mechanical properties

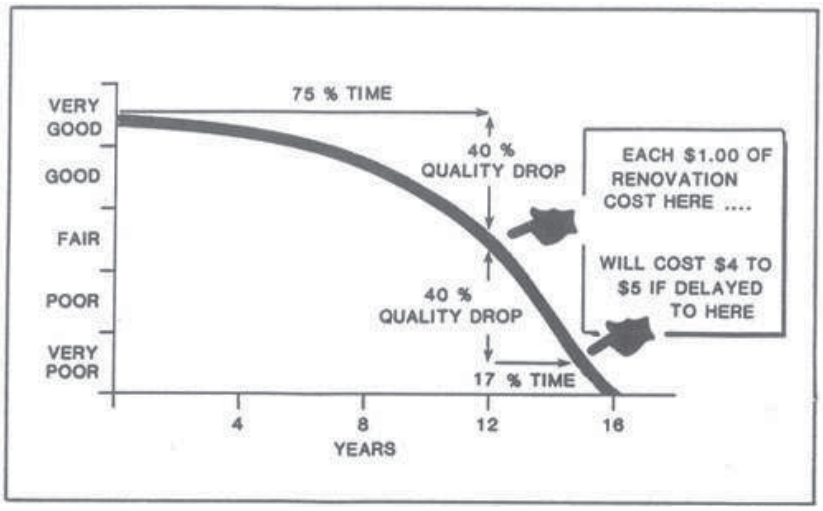

Figure 1.1: Increasing repair cost as a function of pavement deterioration (Elkins et al. [2013])

can be used to estimate stresses and strains in the pavement. Based on this, the bearing capacity and remaining life of the pavement can be estimated.

1.1 Typical pavement structure

In general, there are two types of pavements; asphalt concrete pavements and concrete pavements for which the surface material is asphalt concrete and concrete, respectively. Concrete surfaces can be jointed with or without reinforcement or continuous with reinforcement, while asphalt concrete surfaces are continuous. This thesis deals solely with asphalt concrete pavements.

There are many types of pavement design around the world due to availability of resources and different needs primarily because of different climate conditions. However, in terms of modeling, a pavement structure is typically considered as a three layered continuum structure (see Figure 1.2). On top is a layer of Asphalt Concrete (AC) which consists of primarily two parts; aggregate material and bitumen as binding material. Asphalt concrete is a highly temperature and load rate dependent material due to the nature of the bitumen. It tends to be soft under high temperature or slow loading rates but can be very stiff with cold temperatures or high loading rates.

Most asphalt concrete surfaces are laid on a base consisting of compacted unbound materials such as crushed stone. The base layer is generally at least as thick as the AC layer and serves to spread the load evenly over the subgrade.

The bottom layer is known as the subgrade which most often is natural soil. However in case of very soft natural soil, the subgrade may be stabilized with e.g. cement.

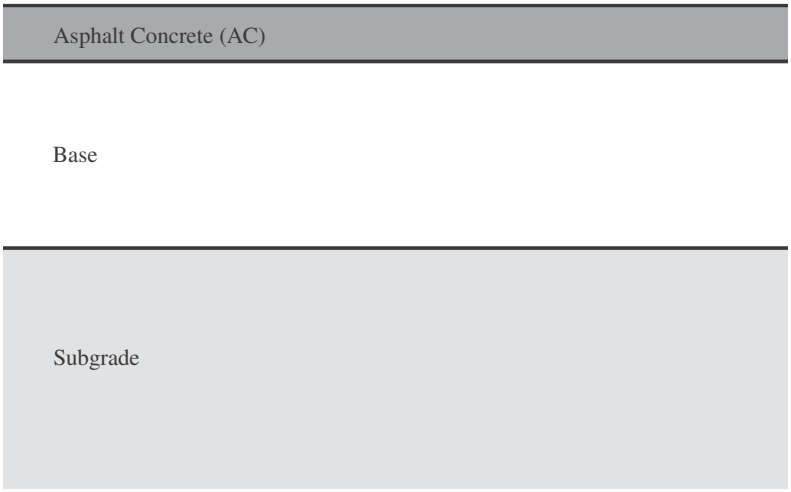

Figure 1.2: Typical pavement structure consisting of Asphalt Concrete (AC), granular base and subgrade.

1.2 Measuring pavement deflections

The general principle of pavement surface deflection measurement is to apply a load of known magnitude to the pavement and measure the vertical deflection of the pavement surface. The measured deflections are interpreted with the aim of identifying the in situ mechanical properties of the individual pavement layers. This is commonly performed by means of backcalculation, wherein model-generated deflections are matched against field-measured deflections.

A number of non-destructive testing devices have been developed over the years for measuring deflections of a pavement due to an applied load. There are in general three categories of non-destructive deflection measurement equipment

- Static load application
- Impact or steady state load application
- Moving load application

The Benkelman beam was one of the first approaches developed in 1953 (Visser and Koesrindartono [2000]). The Benkelman beam which is around 3m long is used with a truck loaded by typically 80kN on a single axle. Deflection measurements are obtained by placing the tip of the beam between the dual tires and measure the rebound of the

pavement surface as the truck is moving away. The load application is considered static since the truck wheel is moving very slow.

The Falling-Weight Deflectometer (FWD) applies an impact type of loading. In general terms, an FWD is designed to generate a short load pulse at the pavement surface, in the order of 30 milliseconds in duration, and record the associated surface deflections. This impact type of loading is achieved by dropping a mass from a predetermined height, and the deflections are measured by an array of geophones. Commercially the FWD has been on the market since the 1970's.
Similar to the FWD are the steady state deflection devices among which the most common are the "Dynaflect" and the "Road Rator". These devices apply a steady state sinusoidal vibration induced through a load plate on the pavement. The devices are stationary when measurements are taken.

The newest development of deflection measurement devices is the Rolling Wheel Deflectometer (RWD). The RWD is a truck loaded by 10 ton on the rear axle and a beam is mounted close to the rear wheel. With a number of lasers mounted on the beam, the RWD continuously measures the pavement deflections while driving with traffic speeds.
For several decades, the FWD has been the industry standard for deflection measurements. There are well established methods for interpretation of FWD deflection measurements in terms of backcalculation of mechanical properties of a pavement. Although the FWD is accurate it is also stationary, which limits the amount of data that can be collected. Furthermore, the cost and safety implications of closing or limiting access to major traffic arteries is preventing FWD measurements from being conducted on important infrastructure assets. The RWD measures at traffic speed and can measure along with normal traffic. Hence it overcomes some of the limitations of the FWD.
However, the two types of devices apply different kind of loading to the pavement. Hence, the deflections measured by an RWD are generally different from deflection measurements obtained by an FWD (Jansen [2015]). Thus, the models currently used for backcalculation of mechanical properties from FWD measurements may not be applicable to RWD measurements. Some studies have tried to compare RWD and FWD center deflection measurements directly and some finds good correlation (Gedafa et al. [2012], MULLER [2015]) and some don't (Elseifi et al. [2012]). In any case, the center deflection alone is not representative for the state of the pavement structure (Ullidtz [1998]). On the other hand, a model capable of taking transient loads moving with various speed into account would be applicable for interpretation of both types of deflection measurements through backcalculation of mechanical properties.

1.3 Pavement modeling

Since the 1940s the layered elastic theory has been the most common tool used to calculate flexible pavement responses to truck loading. In 1943 Burmister et al. [1944] developed a closed-form solution for a two-layered linear elastic half-space, which was later expanded to a three-layer system. The major assumptions in layered elastic theory is:

- Each layer is assumed homogeneous, isotropic and linear elastic
- The subgrade is assumed to be a half-space
- Inertia effects are not taken into account
- The layers are assumed to be fully bonded
- The pavement system is loaded statically over a uniform circular area

A number of computer programs have been developed based on the layered elastic theory. Some of the more well known are Julea, Bisar and Elsym (Ullidtz [1998]). Some programs have introduced modifications to the original layered elastic theory to cover e.g. viscoelastic material models (VERSUS) or to adjust the bonding condition at layer interfaces (BISAR 3.0). However these modifications are only valid under the previous mentioned assumptions for the original layered elastic theory.

Today it is still widely accepted to use static programs as the above mentioned for backcalculation of material parameters from impact loading of the pavement generated by e.g. an FWD, even though a number of works have documented the differences in pavement response from using static and dynamic modeling. Mamlouk and Davies [1984] concluded that dynamic deflections under FWD tests were greater than corresponding static deflections under some circumstances due to dynamic amplification of the pavement structure. Several others such as Chatti et al. [2004] and Al-Khoury et al. [2001] have come to the same conclusion. Kuo and Tsai [2014] stressed the importance of subgrade damping in the dynamic analysis of impact loading.

Analytical models of pavement structures subject to moving loads vary in complexity with regard to the structure such as plates on elastic foundation (Huang and Thambiratnam [2002]) and infinite beam resting on linear or nonlinear viscoelastic foundation (Chen et al. [2001] and Ding et al. [2013], respectively). Compared to FEM, the main advantage of analytical and semi-analytical methods is the relatively short computational time. However, in the analytical and semi-analytical methods, material linearity, homogeneity and no inertia effects are usually assumed in order to solve the equations.

For static and quasi-static situations, FE-models have been available since the late 1970's with the increasing capabilities of computers. Zaghloul and White [1993] were among some of the first to present 3D models for analysis of flexible pavements subject to moving loads. The development of models for pavement response to moving load is still in a relatively early stage. Finite Element modelling of moving loads has been studied with relation to highspeed railways such as Yang et al. [2003] who studied the effect of train speeds on wave propagation in layered soils. Later, 2.5D Finite Element methods have been presented which allows for plane section analysis but with a correct representation of wave propagation in 3D, see e.g. FranÇois et al. [2010] and Galvín et al. [2010]. However, these methods might not be appropriate in relation to deflection measurements obtained by an RWD which measures and correlates the deflections in the longitudinal direction of the pavement. Thus, analysis of the longitudinal section is of importance.

Some advanced 3D Finite Element models for simulating the dynamic behaviour of pavements have been developed. Yoo and Al-Qadi [2007] developed a 3D Finite Element model in Abaqus for dynamic analysis of the pavement response to transient loading. They observed an increase in stresses and strains of up to 39% due to dynamic effects compared to a corresponding static response. This was supported by Beskou et al. [2016] who studied dynamic versus static behaviour of pavement response to moving load in a linear elastic 3D Finite Element model developed in Ansys. They found that the response obtained by dynamic analysis is higher than the corresponding response obtained by static analysis and that increasing vehicle speed increases the pavement response of dynamic analysis. In both works the moving load is simulated by moving nodal loads from element to element across the surface requiring a huge number of elements to ensure high resolution in the entire area the load is moving. Hence, simulations are computational heavy especially if longer simulations are needed.

Lane et al. Lane et al. [2008] presented a mesh movement algorithm where the elements are moved with the same velocity as the load in their study of dynamic vehicle interaction and wave propagation in a 3D Finite Element model. This requires a change of the grid in each time step. On the other hand, Dieterman and Metrikine Dieterman and Metrikine [1997] studied the analytical solution of the steady-state displacement of an Euler-Bernoulli beam resting on an elastic half space due to a uniformly constant moving load by introducing a coordinate transformation into a moving frame of reference. Krenk et al. Krenk et al. [1999] presented 2D formulation in a convected coordinate system moving with the load and using a transmitting boundary condition in the form of a spring-dashpot model for absorption of waves, modified to account for the translation velocity and the difference between compression and shear waves, see also Andersen et al. [2007]. Based on this approach, Zhai and Song [2010] developed a 3D Finite Element model in a moving frame of reference. A review on modelling of the response to moving loads in Finite Element and Boundary Element methods is given by Andersen et al. [2007]. An advantage of modeling in a moving frame of reference is that high mesh resolution can be concentrated around the load without any need

of remeshing. This is especially an advantage in 3D Finite Element modeling where computation time increases rapidly due to increasing number of elements.

1.4 Perfectly Matched Layer (PML)

Solving wave propagation problems in an infinite half space implies that the infinite region exterior to the load source needs to be truncated by some type of artificial boundary such that the computational domain becomes limited. Hence, a boundary condition that absorbs waves, leaving the computational domain independent of propagation direction and frequency, needs to be introduced. Such a boundary condition serves as far as possible as a transparent boundary yielding perfect transmission of the waves and thereby minimizing the non-physical reflections from the boundary. Several absorbing boundary condition techniques have been developed to achieve this purpose. It comprises non-local conditions and local conditions. A non-local condition is an exact representation of the infinite field, which is difficult to implement and difficult to further develop to handle e.g. non-linearity and transformation into convective coordinates. Local boundary conditions, such as Lysmer and Kuhlemeyer [1969] who used dashpots to absorb incident waves, only exhibit good performance under specific circumstances, e.g. dependent on frequency and angle of incidence. The introduction of the Perfectly Matched Layer (PML) in 1994 revolutionized absorbing boundaries for wave equations because it was designed to efficiently absorb outgoing electromagnetic waves regardless of their propagation characteristics and angle of incidence. The PML is a half space with the same properties as the original half space but dispersive such that waves are attenuated exponentially independent of frequency and angle of incidence. A literature review on PML is given in [P1].

1.5 Objective and thesis structure

The present Ph.D. project has been carried out in collaboration with Dynatest who is currently in the process of developing an RWD. In this relation, the objective of the thesis is to develop a model capable of simulating the response of a pavement subjected to vehicular loads of various speed. For decades, the FWD has been the industry standard for deflection measurements and thus, the FWD serves as an important benchmark. In this thesis, the developed model is therefore applied for simulation and interpretation of FWD measurements. A model capable of simulating the pavement response to both stationary impact and transient moving loads can provide a standard of comparison for RWD and FWD measurements.

This thesis serves as an introduction to the work that has been carried out during the Ph.D. study. The thesis consists of four chapters followed by two appended papers.
Chapter 2 presents a new Finite Element formulation for transient dynamic analysis with the Perfectly Matched Layer (PML) as absorbing boundary condition. The formulation is in a moving frame of reference and the equations are derived in 1D, 2D and 3D, followed by an exhaustive survey of the numerical implementation. The chapter also presents a method for generating a Finite Element mesh that balances computational time and numerical accuracy.
In Chapter 3, the model is applied for backcalculation of mechanical properties of a pavement from FWD experiments. For this purpose, the model is presented in an axisymmetric domain and a method for backcalculation is developed.
Finally, some concluding remarks are given in Chapter 4

Chapter 2

Dynamic modeling of flexible pavements

In this chapter a derivation of the governing equation of motion with the Perfectly Matched Layer (PML) as absorbing boundary formulated in a moving frame of reference is given. Section 2.1 presents a derivation of the equations governing PML in relation to elastic wave propagation. First, a closed form solution is given for a 1D problem and next, the more general two- and three-dimensional problems are treated. Section 2.2 treats the transformation of the 3D formulation into a moving frame of reference. Section 2.3 gives an exhaustive survey of the finite element formulation including spatial and temporal discretization. Section 2.4 focuses on aspects specific to the dynamic modeling of pavements. A new method for generating a finite element mesh that balances computational time and numerical accuracy is presented in this section as well. Section 2.5 presents some of the main findings related to the performance of the PML in a moving frame of reference and influence of load speed. Section 2.6 deals with wave propagation in 3D including a comparison with propagation of waves in 2D.

2.1 Perfectly Matched Layer (PML)

The present section introduces the method of a perfectly matched layer for absorbing out-going elastic waves. The method, introduced by Matzen [2011], makes use of a formal coordinate transformation by which a regular wave in the transformed spatial coordinates is recast into an equivalent problem in the original coordinates in such a way that the coordinate transformation appears as coefficients in the governing equations that are subsequently solved by finite elements. The characteristic feature of the method is that the transformation is only introduced in a layer surrounding the computational domain, in which the transformation degenerates to an identity. Thus, the special features of the absorbing boundary condition only appear in the surrounding layer, which is included in the finite element model. The boundary layer is characterized by its thickness and parameters describing its dissipation properties. In order to illustrate the role of the parameters and their calibration the following section introduces a simple one-dimensional problem, which is solved in closed form. The formulation of the more general two- and three-dimensional problems are treated in section 2.1.2 and 2.1.3, respectively.

2.1.1 One-dimensional wave propagation

The one-dimensional propagation of linear elastic waves is governed by the linear elastic constitutive relation

$$\sigma = E\frac{\partial u}{\partial x} \tag{2.1}$$

in which σ is the stress and u is the displacement. The elastic parameter is indicated as Young's modulus E, corresponding to the propagation of unconstrained elastic waves in an elastic bar. In the case of time harmonic motion, represented by the complex factor $\mathrm{e}^{i\omega t}$ with angular frequency ω, the equation of motion takes the form

$$\frac{\partial \sigma}{\partial x} = -\omega^2 \rho u \tag{2.2}$$

where ρ is the mass density. It is seen that these equations permit a solution in the form of a traveling wave of the form

$$u(x,t) = u_0\,\mathrm{e}^{\,i(\omega t - kx)} \tag{2.3}$$

where k is the wave-number, identified by substitution of (2.1) into (2.2) as

$$k = \pm\frac{\omega}{\sqrt{E/\rho}} = \pm\frac{\omega}{c} \tag{2.4}$$

where c is the wave speed. In this formulation the wave-number k is real-valued and the waves therefore propagate without attenuation.

In the boundary layer a transformed coordinate $\tilde{x}$ is defined by the derivative relation

$$\frac{\partial \tilde{x}}{\partial x} = s(x) \tag{2.5}$$

in terms of the stretching function $s(x)$, expressing the local change of the transformed coordinate $\tilde{x}$ with respect to the original coordinate x. This relation corresponds to the integral form

$$\tilde{x} = \int_0^x s(\xi, \omega) d\xi \tag{2.6}$$

of the stretched coordinate. When the constitutive equation (2.1) and the equation of motion (2.2) is given as if the problem was described by the transformed coordinate $\tilde{x}$ they take the form

$$\sigma = E \frac{\partial u}{\partial \tilde{x}}, \qquad \frac{\partial \sigma}{\partial \tilde{x}} = -\omega^2 \rho u \tag{2.7}$$

These equations can now be expressed in terms of the original coordinate x by use of the differentiation relation (2.5), whereby

$$\sigma = s^{-1} E \frac{\partial u}{\partial x}, \qquad \frac{\partial \sigma}{\partial x} = -\omega^2 s \rho u \tag{2.8}$$

In the present one-dimensional case it is seen that the formulation in terms of a transformed spatial coordinate is equivalent to introducing space and frequency dependent factors $s(x, \omega)^{\pm 1}$ on the material parameters E and ρ.

The purpose of the complex stretching function is to introduce appropriate damping. The stretching function is here taken in the form (Chew and Weedon [1994])

$$s(x) = 1 + \frac{\beta(x)}{i\,\omega} \tag{2.9}$$

where $\beta \geq 0$ is a real-valued local reference frequency controlling the attenuation of the wave propagation inside the PML layer. In the bounded domain where no attenuation occurs, $\beta = 0$ and $s(x) = 1$, resulting in the original elastic wave equations (2.1) and (2.2). To avoid numerical reflection from the PML interface caused by an abrupt change in the wave attenuation at the interface, the attenuation function β should increase gradually. A quadratic polynomial profile $\beta(x)$ is used as proposed by Zheng and Huang [2002] and Singer and Turkel [2004]

$$\beta(x) = \beta_{\max} \left(\frac{x^p}{d} \right)^2 \tag{2.10}$$

where x^p is measured from the interface between the computational domain and the PML, and d is the thickness of the PML layer. The parameter $\beta_{\max}$ controls the magnitude of the attenuation within the PML.

The efficiency of the PML is evaluated by examining steady wave propagation. In a steady wave problem, very small reflections from the absorbing boundary can cause a noticeable standing wave in the computational domain. In the 1D example illustrated in Figure 2.1a, a harmonic wave is passed through the computational domain and then passing into the matched layer, which is rigidly supported at its exterior boundary.

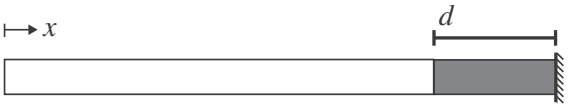

(a) Computational domain with adjacent PML

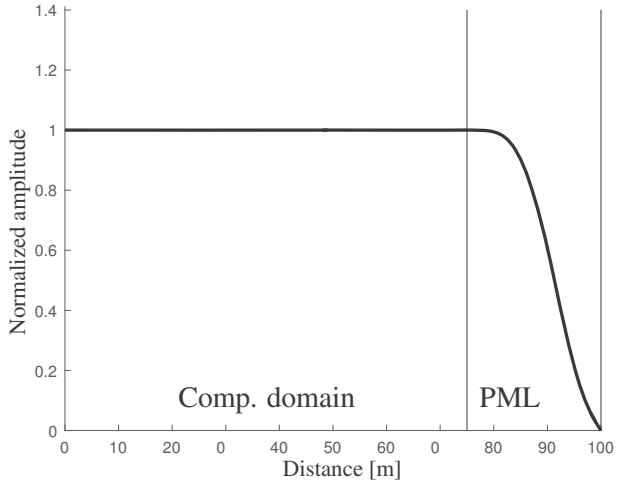

(b) 1D elastic wave propagation with PML

Figure 2.1: Normalized amplitude of 1D elastic wave propagation. The computational domain is truncated by a 1.5λ thick PML.

The analytical solution of the incoming wave is of the form (2.3),

$$u(\tilde{x}, t) = u_0 \, \mathrm{e}^{\,i\,(\omega t - k\tilde{x})} \tag{2.11}$$

The transformed coordinate $\tilde{x}$ is calculated from (2.6) and substitution into (2.11) giving the attenuated wave

$$u(x, t) = u_0 \, \mathrm{e}^{\,i\,(\omega t - kx)} \, \exp\Big[- \frac{\beta_{\max} d}{3c} \Big(\frac{x}{d} \Big)^3 \Big] \tag{2.12}$$

where the wave speed $c = \omega / k$ has been introduced.

The quality of the PML radiation condition can be characterized by the ratio of the wave amplitude at the outside of the PML layer relative to the amplitude of the wave

when entering the layer at the inside. When introducing the wave speed in the form $c = \lambda\omega/2\pi$, the amplitude reduction takes the form

$$A_0 = \exp\Big(-\frac{\beta_{\max} d}{3c}\Big) = \exp\Big(-\frac{2\pi}{3}\frac{\beta_{\max}}{\omega}\frac{d}{\lambda}\Big) \tag{2.13}$$

The attenuation obtained at the exterior boundary of the PML is seen to depend on the ratio of layer thickness to wave length, d/λ, and on the ratio of intensity parameter to frequency, $\beta_{\max}/\omega$.

Figure 2.1b shows the numerical result of the normalized amplitude of the propagating wave. In this example the computational domain has a compressional wave speed $c_p = 250$m/s and a density $\rho = 2000\text{kg/m}^3$. All elastic waves are excited continuously at a frequency of $f = 15\,\text{Hz}$. The thickness of the PML is $d = 1.5\lambda$. In the computational domain, the wave amplitude is nearly uniform which means there is almost no reflections occurring from the PML. The transmitted wave dissipates very well in the PML.

2.1.2 Two-dimensional wave propagation

In this section, a set of equations is set up for a stretched 2D elasticity problem. These equations incorporate damping if the coordinates are stretched, and specialize to the classic undamped elasticity equations if the original coordinates are retained without stretching. The equations of two-dimensional isotropic linear elasticity consist of the constitutive equations and the equations of motion. The constitutive equations relating the stresses $\boldsymbol{\sigma}$ (matrix) and the derivatives of the displacements $\mathbf{u}$ are

$$\boldsymbol{\sigma} = \lambda\,(\boldsymbol{\nabla}^T\mathbf{u})\,\mathbf{I} + \mu\,[(\boldsymbol{\nabla}\mathbf{u}^T) + (\boldsymbol{\nabla}\mathbf{u}^T)^T] \tag{2.14}$$

where the gradient operator is defined by

$$\boldsymbol{\nabla}^T = \Big[\frac{\partial}{\partial x_1}, \frac{\partial}{\partial x_2}\Big] \tag{2.15}$$

and λ and μ are the Lamé parameters. When considering harmonic time variation represented via the factor $e^{i\omega t}$, the equation of motion takes the form

$$(\boldsymbol{\nabla}^T\boldsymbol{\sigma})^T = -\omega^2\rho\,\mathbf{u} \tag{2.16}$$

where ρ is the mass density.

The original elasticity problem is now reformulated by using the notion of stretched coordinates. Similar to the 1D case, stretched coordinates $\tilde{x}_j = \tilde{x}_j(x_j)$ are introduced, defined in terms of the original coordinates x_j by the relation

$$\frac{\partial\tilde{x}_j}{\partial x_j} = s_j\,, \quad j = 1,2 \tag{2.17}$$

for the derivatives. It is noted that by this assumption each coordinate is stretched independently. The stretching functions s_1 and s_2 are in the form

$$s_j(x_j) = 1 + \frac{\beta_j(x_j)}{i\,\omega}\,, \quad j = 1, 2. \tag{2.18}$$

The stretching functions deviate from unity by an additive term consisting of an attenuation function $\beta(x)$ depending on the coordinate x and assumed increasing through the bounding layer. The attenuation function is divided by the imaginary frequency factor $i\omega$. When converting the frequency representation to the time domain, the frequency factor $(i\omega)^{-1}$ corresponds to time integration in the same way the factor $i\omega$ corresponds to time differentiation. The role of the attenuation functions is to introduce an imaginary part that increases gradually from the interface between the elastic domain and the surrounding boundary layer. This is accomplished by selecting the attenuation functions in the form (as proposed by (Zheng and Huang [2002] and Singer and Turkel [2004])

$$\beta_j(x_j) \;=\; \beta_{\max}\left(\frac{x_j^p}{d}\right)^2 \tag{2.19}$$

where the superscript p denotes the corresponding coordinate with origin at the interface between the elastic domain and the boundary layer. The boundary layer surrounds the elastic region as illustrated in Figure 2.2 showing three side regions and two corner regions. In the side regions only the coordinate orthogonal to the interface is transformed, while both coordinates are transformed in the corner regions.

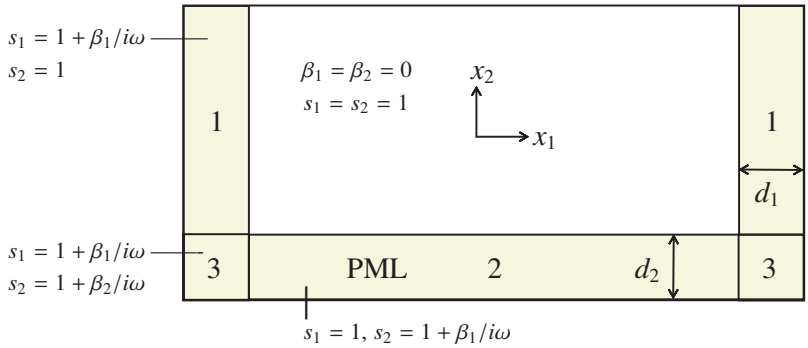

Figure 2.2: Computational domain surrounded by PML. Region 1: $s_1 = 1 + \beta_1/i\omega$ and $s_2 = 1$, region 2: $s_1 = 1$ and $s_2 = 1 + \beta_2/i\omega$, region 3: $s_1 = 1 + \beta_1/i\omega$ and $s_2 = 1 + \beta_2/i\omega$. In the computational domain $s_1 = s_2 = 1$.

The idea is to formulate a formal elasticity problem by using derivatives in terms of the stretched coordinates, and by introducing a suitable formal stress definition. Once the equations are formulated, the stretching parameters are absorbed into the constitutive parameters and the mass density corresponding to time differentiation and integration

operators on the physical parameters λ, μ and ρ. The first step is to introduce the transformed gradient operator

$$\tilde{\boldsymbol{\nabla}} \;=\; \Big[\frac{\partial}{\partial \tilde{x}_1}, \frac{\partial}{\partial \tilde{x}_2}\Big]^T \;=\; \Big[\frac{1}{s_1}\frac{\partial}{\partial x_1}, \frac{1}{s_2}\frac{\partial}{\partial x_2}\Big]^T \tag{2.20}$$

in terms of the stretched coordinates. In the boundary layer the use of this gradient operator would define a formal stress

$$\boldsymbol{\sigma} \;=\; \lambda\,(\tilde{\boldsymbol{\nabla}}^T\mathbf{u})\,\mathbf{I} \;+\; \mu\,[(\tilde{\boldsymbol{\nabla}}\mathbf{u}^T) + (\tilde{\boldsymbol{\nabla}}\mathbf{u}^T)^T]. \tag{2.21}$$

It follows from the format of this formal stress definition that the stress component matrix is symmetric, $\sigma_{12} = \sigma_{21}$. However, the formal strain matrix, given by the square brackets in (2.21), is now no longer symmetric, and the off-diagonal elements are defined in terms of the classic shear strain as well as the rotation. Thus, there are essentially four deformation components, but only three components in the formal stress matrix $\boldsymbol{\sigma}$. A resolution to the problem is suggested by the formal equation of motion,

$$(\tilde{\boldsymbol{\nabla}}^T\boldsymbol{\sigma})^T \;=\; -\omega^2\rho\,\mathbf{u} \tag{2.22}$$

The transformation of the gradient operator introduces factors s_j^{-1} on the derivatives corresponding to the first index of σ_{jk}. This suggests the use of a formal stress with components defined by, Chew and Liu [1996],

$$\tilde{\boldsymbol{\sigma}} \;=\; s_1 s_2 \begin{bmatrix} 1/s_1 & \\ & 1/s_2 \end{bmatrix} \boldsymbol{\sigma}\,. \tag{2.23}$$

The factor $s_1 s_2$ in this relation is suggested by the consideration that the final form of the formal stress-strain relation should not contain powers of s_j less than of degree -1 in order to enable a direct interpretation of the frequency problem in the time domain as discussed later.

When introducing the definition (2.23), the formal stress $\tilde{\boldsymbol{\sigma}}$ is related to a set of formal strains including the rotation component by a relation of the form

$$\tilde{\boldsymbol{\sigma}} \;=\; \tilde{\mathbf{C}}\,\boldsymbol{\varepsilon}\,. \tag{2.24}$$

In this relation it is convenient to introduce the formal stress in the vector format

$$\bar{\boldsymbol{\sigma}} \;=\; \begin{bmatrix} \tilde{\sigma}_{11} \\ \tilde{\sigma}_{22} \\ \frac{1}{2}(\tilde{\sigma}_{21} + \tilde{\sigma}_{12}) \\ \frac{1}{2}(\tilde{\sigma}_{21} - \tilde{\sigma}_{12}) \end{bmatrix} \tag{2.25}$$

and the formal strains in the corresponding array format

$$\boldsymbol{\varepsilon} \;=\; \boldsymbol{\partial}\mathbf{u} \;=\; \begin{bmatrix} \partial_{x_1} & 0 \\ 0 & \partial_{x_2} \\ \partial_{x_2} & \partial_{x_1} \\ \partial_{x_2} & -\partial_{x_1} \end{bmatrix} \begin{bmatrix} u_1 \\ u_2 \end{bmatrix} \tag{2.26}$$

Straightforward substitution of (2.23) into the constitutive equations (2.21) then gives the constitutive matrix $\tilde{\mathbf{C}}$ in the form

$$\tilde{\mathbf{C}} = \mathbf{C}_0 + \frac{s_1}{s_2}\mathbf{C}_1 + \frac{s_2}{s_1}\mathbf{C}_2 \tag{2.27}$$

The non-stretched part $\mathbf{C}_0$ and the two stretched parts $\mathbf{C}_1$ and $\mathbf{C}_2$ are given by

$$\mathbf{C}_0 = \begin{bmatrix} 0 & \lambda & 0 & 0 \\ \lambda & 0 & 0 & 0 \\ 0 & 0 & \mu/2 & 0 \\ 0 & 0 & 0 & -\mu/2 \end{bmatrix}, \quad \mathbf{C}_1 = \begin{bmatrix} 0 & 0 & 0 & 0 \\ 0 & \lambda+2\mu & 0 & 0 \\ 0 & 0 & \mu/4 & \mu/4 \\ 0 & 0 & \mu/4 & \mu/4 \end{bmatrix},$$

$$\mathbf{C}_2 = \begin{bmatrix} \lambda+2\mu & 0 & 0 & 0 \\ 0 & 0 & 0 & 0 \\ 0 & 0 & \mu/4 & -\mu/4 \\ 0 & 0 & -\mu/4 & \mu/4 \end{bmatrix} \tag{2.28}$$

In the special case $s_1 = s_2 = 1$, used in the computational domain, the matrix takes the form

$$\mathbf{C} = \mathbf{C}_0 + \mathbf{C}_1 + \mathbf{C}_2 \tag{2.29}$$

corresponding to plane strain with symmetric stress components.

The equation of motion is obtained from (2.23), when disregarding the spatial derivatives of the factors s_1 and s_2. Hereby the equations of motion in terms of the formal stress $\bar{\boldsymbol{\sigma}}$ in the array format (2.25) take the form

$$\boldsymbol{\partial}^T \bar{\boldsymbol{\sigma}} = -\rho\, s_1 s_2 \omega^2\, \mathbf{u}\,, \tag{2.30}$$

where $\boldsymbol{\partial}$ is the spatial differential operator introduced in the strain definition (2.26).

2.1.2.1 Time domain equations

The frequency-dependent system of equations consisting of the constitutive equation (2.24) is transformed into time domain using the inverse Fourier transform. The constitutive equation takes the form

$$\bar{\boldsymbol{\sigma}} = C * \boldsymbol{\varepsilon}\,, \tag{2.31}$$

where the symbol $*$ implies convolution with the time-dependent constitutive matrix defined by

$$C = \mathbf{C} + \mathcal{F}_1(t)\mathbf{C}_1 + \mathcal{F}_2(t)\mathbf{C}_2 \tag{2.32}$$

It is noted that the matrix **C** corresponds to the standard time-independent form defined in (2.29). Thus, the functions $\mathcal{F}_1(t)$ and $\mathcal{F}_2(t)$ are the inverse Fourier transforms of $s_1/s_2 - 1$ and $s_2/s_1 - 1$, respectively,

$$\mathcal{F}_1(t) = (\beta_1 - \beta_2)e^{-\beta_2 t}, \quad t \geq 0 \tag{2.33a}$$

$$\mathcal{F}_2(t) = (\beta_2 - \beta_1)e^{-\beta_1 t}, \quad t \geq 0 \tag{2.33b}$$

The implementation of this formulation makes use of a time-step form in which the convolution integrals involving $\mathcal{F}_1(t)$ and $\mathcal{F}_2(t)$ are replaced by increments, thereby limiting the computations to the current time increment.

In the time domain the equation of motion (2.30) takes the form

$$\boldsymbol{\partial}^T \bar{\boldsymbol{\sigma}} = \mathcal{D}_0(t)\,\rho\,\mathbf{u}\,. \tag{2.34}$$

The operator $\mathcal{D}_0(t)$ is the inverse Fourier transform of $-\omega^2 s_1 s_2$ given by

$$\mathcal{D}_0(t) = \frac{d^2}{dt^2} + (\beta_1 + \beta_2)\frac{d}{dt} + \beta_1\beta_2 \tag{2.35}$$

The first term represents the inertia term, while the second term represents a velocity proportional viscous damping and the last term a mass-proportional stiffness, both acting on the absolute motion.

2.1.3 Three-dimensional wave propagation

In this section, the three-dimensional equation of motion with PML in the time domain is derived following the same procedure as for the two-dimensional equations. The three-dimensional equation of motion takes the equivalent form as the two-dimensional (2.16)

$$(\boldsymbol{\nabla}^T \boldsymbol{\sigma})^T = -\omega^2 \rho\,\mathbf{u} \tag{2.36}$$

in which the gradient is defined by $\nabla_i = \partial_{x_i}$, $i = 1, 2, 3$ with $\partial_{x_i} = \partial/\partial x_1$, u is the three-dimensional displacement vector and the stresses are governed by (2.14) in the case of isotropic linear elasticity. After mapping (2.36) into the complex stretching coordinates defined in (2.17) (only with $j = 1, 2, 3$) equation (2.36) is rewritten in real coordinates based on the chain rule $\partial_{\tilde{x}_i} = 1/s_i \partial_{x_i}$

$$(\tilde{\nabla}^T \boldsymbol{\sigma})^T = -\omega^2 \rho \mathbf{u} \tag{2.37a}$$

$$\boldsymbol{\sigma} = \lambda\,(\tilde{\boldsymbol{\nabla}}^T \mathbf{u})\,\mathbf{I} + \mu\,[(\tilde{\boldsymbol{\nabla}}\mathbf{u}^T) + (\tilde{\boldsymbol{\nabla}}\mathbf{u}^T)^T]. \tag{2.37b}$$

where $\tilde{\boldsymbol{\nabla}}_i = (1/s_i)\partial_{x_i}$. In order to obtain a formulation in time domain based on the displacement vector, (2.37) is reformulated by multiplying by $s_1 s_2 s_3$ on both sides of

the equation of motion (Xie et al. [2014])

$$s_1 s_2 s_3 (\tilde{\nabla}^T \boldsymbol{\sigma})^T = -\omega^2 s_1 s_2 s_3 \rho \mathbf{u} \tag{2.38a}$$

$$\boldsymbol{\sigma} = \lambda (\tilde{\boldsymbol{\nabla}}^T \mathbf{u}) \mathbf{I} + \mu [(\tilde{\boldsymbol{\nabla}} \mathbf{u}^T) + (\tilde{\boldsymbol{\nabla}} \mathbf{u}^T)^T]. \tag{2.38b}$$

In vector components equation (2.38) can be written as

$$\begin{aligned} -\rho\, s_i\, s_j\, s_k\, \omega^2\, u_i &= \partial_{x_i} \left((\lambda + 2\mu) \frac{s_j s_k}{s_i} \partial_{x_i} u_i + \lambda\, s_k\, \partial_{x_j} u_j + \lambda\, s_j\, \partial_{x_k} u_k \right) \\ &+ \partial_{x_j} \left(\mu\, s_k\, \partial_{x_i} u_j + \mu \frac{s_i s_k}{s_j} \partial_{x_j} u_i \right) \\ &+ \partial_{x_k} \left(\mu\, s_j\, \partial_{x_i} u_k + \mu \frac{s_i s_j}{s_k} \partial_{x_k} u_i \right) \end{aligned} \tag{2.39}$$

where $i, j, k = 1, 2, 3$ and $i \neq j \neq k$. Following the procedure given in the 2D formulation, a new definition of the formal stresses is introduced

$$\tilde{\boldsymbol{\sigma}} = s_1 s_2 s_3 \begin{bmatrix} 1/s_1 & & \\ & 1/s_2 & \\ & & 1/s_3 \end{bmatrix} \boldsymbol{\sigma} \tag{2.40}$$

such that the gradient can be kept in an unstretched format. Equivalent to Equations (2.25) and (2.26) in 2D, the constitutive relation is given in an array format by

$$\begin{bmatrix} \tilde{\sigma}_{11} \\ \tilde{\sigma}_{22} \\ \tilde{\sigma}_{33} \\ \frac{1}{2}(\tilde{\sigma}_{12} + \tilde{\sigma}_{21}) \\ \frac{1}{2}(\tilde{\sigma}_{13} + \tilde{\sigma}_{31}) \\ \frac{1}{2}(\tilde{\sigma}_{23} + \tilde{\sigma}_{32}) \\ \frac{1}{2}(\tilde{\sigma}_{12} - \tilde{\sigma}_{21}) \\ \frac{1}{2}(\tilde{\sigma}_{13} - \tilde{\sigma}_{31}) \\ \frac{1}{2}(\tilde{\sigma}_{23} - \tilde{\sigma}_{32}) \end{bmatrix} = \tilde{C} \begin{bmatrix} \partial_{x_1} & & \\ & \partial_{x_2} & \\ & & \partial_{x_3} \\ \partial_{x_2} & \partial_{x_1} & \\ \partial_{x_3} & & \partial_{x_1} \\ & \partial_{x_3} & \partial_{x_2} \\ \partial_{x_2} & -\partial_{x_1} & \\ \partial_{x_3} & -\partial_{x_1} & \\ & \partial_{x_3} & -\partial_{x_2} \end{bmatrix} \begin{bmatrix} u_1 \\ u_2 \\ u_3 \end{bmatrix} \tag{2.41}$$

and in short matrix notation

$$\bar{\boldsymbol{\sigma}} = \tilde{C} \partial \mathbf{u} = \tilde{C} \boldsymbol{\varepsilon} \tag{2.42}$$

The constitutive matrix $\tilde{\mathbf{C}}$ obtained from substitution of (2.40) into (2.37b) is given in Appendix A, Equation (A.2) (Harari and Albocher [2006]).

2.1.3.1 Time domain equations

Applying the new definition of the formal stresses (2.40) in (2.37) the equation of motion in terms of the formal stresses in the array format (2.41) takes the form

$$\boldsymbol{\partial}^T \bar{\boldsymbol{\sigma}} = \rho\, \mathcal{D}_0(t) * \mathbf{u} \tag{2.43a}$$

$$\bar{\boldsymbol{\sigma}} = C * \boldsymbol{\varepsilon} \tag{2.43b}$$

where the symbol $*$ denotes convolution. Applying the stretching function defined in (2.18) (with $j = 1, 2, 3$) the operator $\mathcal{D}_0(t)$ comes from inverse Fourier transformation of $-\omega^2 s_1 s_2 s_3$ yielding

$$\mathcal{D}_0(t) = \frac{\partial^2}{\partial t^2} + (\beta_1 + \beta_2 + \beta_3)\frac{\partial}{\partial t} + (\beta_1\beta_2 + \beta_1\beta_3 + \beta_2\beta_3) + \mathcal{L}_0(t) \tag{2.44}$$

where $\mathcal{L}_0(t)$ is given by

$$\mathcal{L}_0(t) = \frac{1}{2}\beta_1\beta_2\beta_3\,, \quad t \geq 0 \tag{2.45}$$

The time dependent constitutive matrix is defined by

$$C = \mathbf{C} + \mathcal{F}_{12/3}\mathbf{C}_{12/3} + \mathcal{F}_{13/2}\mathbf{C}_{13/2} + \mathcal{F}_{23/1}\mathbf{C}_{23/1} + \mathcal{H}_1\mathbf{C}_1 + \mathcal{H}_2\mathbf{C}_2 + \mathcal{H}_3\mathbf{C}_3 \tag{2.46}$$

The matrix $\mathbf{C}$ corresponds to the standard time-independent constitutive matrix obtained by setting $s_1 = s_2 = s_3 = 1$ in Equation (A.2). The functions $\mathcal{F}_{ij/k}$ and $\mathcal{H}_i$ are the inverse Fourier transforms of $s_i\, s_j \,/\, s_k - 1$ and $s_i - 1$, respectively, given by

$$\mathcal{F}_{ij/k}(t) = \frac{1}{\beta_k}(\beta_j - \beta_k)(\beta_i - \beta_k)e^{-\beta_k t} + \frac{1}{2}\frac{\beta_i\beta_j}{\beta_k}\,, \quad t \geq 0 \tag{2.47a}$$

$$\mathcal{H}_i(t) = \frac{1}{2}\beta_i\,, \quad t \geq 0 \tag{2.47b}$$

in which $i, j, k = 1, 2, 3$ and $i \neq j \neq k$. The subscripts i, j and k in $\mathcal{F}_{ij/k}$ and $\mathcal{H}_i$ corresponds to the indices of the inverse Fourier transforms of $F^{-1}[s_i s_j / s_k - 1]$ and $F^{-1}[s_i - 1]$, respectively, with F^{-1} denoting inverse Fourier transformation. In other words, $\mathcal{F}_{12/3} = F^{-1}[s_1 s_2 / s_3 - 1]$ and $\mathcal{H}_2 = F^{-1}[s_2 - 1]$. The corresponding constitutive matrices $C_{ij/k}$ and C_i contain the stretched entries of $\tilde{\mathbf{C}}$ relating to $s_i s_j / s_k$ and s_i, respectively, which may be found in Appendix A. The numerical solution to the convolution integrals is discussed in section 2.3.

2.2 Convected Mesh Model

Following Krenk et al. [1999] a convected coordinate system moving with the load is introduced via the relation

$$x = X - Vt \tag{2.48}$$

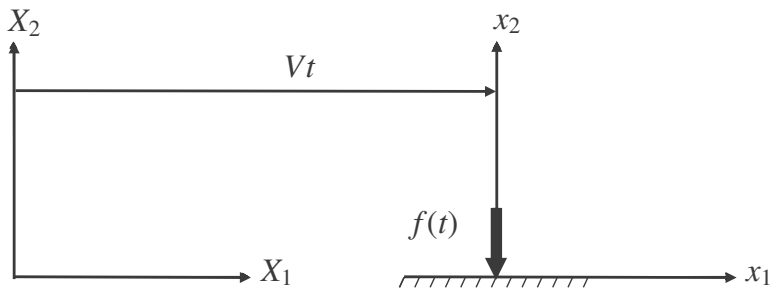

Figure 2.3: Moving surface load in fixed X_i-coordinate system

where X is the coordinate of the moving load in the fixed reference coordinate system, while x is the coordinate in the coordinate system following the load that is moving with velocity V (see Figure 2.3). The relation (2.48) implies the following differentiation relations

$$\left.\frac{\partial}{\partial X}\right|_t = \left.\frac{\partial}{\partial x}\right|_t, \qquad \left.\frac{\partial}{\partial t}\right|_X = \left.\frac{\partial}{\partial t}\right|_x - V\frac{\partial}{\partial x} \tag{2.49}$$

Note that for convenience x is used instead of x_1 in the derivative with respect to x_1.

Substitution of these operators into the equation of motion (2.43) leads to the following modified form of the equilibrium equation in the moving coordinate system

$$\boldsymbol{\partial}^T \bar{\boldsymbol{\sigma}} = \rho \tilde{\mathcal{D}}_0(t) * \mathbf{u} \tag{2.50}$$

with the convected time differentiation operator

$$\bar{\mathcal{D}}_0(t) = \left(\frac{\partial}{\partial t} - V\frac{\partial}{\partial x}\right)^2 + (\beta_1 + \beta_2 + \beta_3)\left(\frac{d}{dt} - V\frac{d}{dx}\right) \tag{2.51}$$

$$+ \quad \beta_1\beta_2 + \beta_1\beta_3 + \beta_2\beta_3 + \mathcal{L}_0(t), \quad t \geq 0 \tag{2.52}$$

When using this operator in the dynamic equation (2.50) the following form of the equation is obtained

$$\begin{aligned}\boldsymbol{\partial}^T \bar{\boldsymbol{\sigma}} = \rho &\left(\frac{\partial^2 \mathbf{u}}{\partial t^2} + (\beta_1 + \beta_2 + \beta_3)\frac{\partial \mathbf{u}}{\partial t} + (\beta_1\beta_2 + \beta_1\beta_3 + \beta_2\beta_3)\mathbf{u}\right) \\ &+ V^2\frac{\partial^2(\rho\mathbf{u})}{\partial x^2} - (\beta_1 + \beta_2 + \beta_3)V\frac{\partial(\rho\mathbf{u})}{\partial x} - 2V\frac{\partial^2(\rho\mathbf{u})}{\partial x \partial t} \\ &+ \frac{1}{2}\rho\beta_1\beta_2\beta_3 * u(t), \quad t \geq 0\end{aligned} \tag{2.53}$$

The first three terms on the right correspond to the representation in a fixed coordinate system, while the three next represent the effect of translation.

The convolution integrals in the constitutive relation (2.43b) are related to the artificial properties of the boundary layer, and when assuming these properties convected with

the load the form of the constitutive equation remains unchanged by the translation. Hereby the transformation from fixed to moving coordinates only modifies the dynamic equation, permitting a fairly straight forward implementation of the PML formulation in the translating formulation.

2.3 FE implementation

The formulation is written in a finite element formulation using the principle of virtual work by multiplying by a virtual displacement and integrating over the volume yielding

$$\int_V \tilde{\mathbf{u}}^T \boldsymbol{\partial}^T \bar{\boldsymbol{\sigma}} dV - \rho \int_V \tilde{\mathbf{u}}^T \tilde{\mathcal{D}}_0(t) * \mathbf{u} dV = 0 \tag{2.54}$$

The spatial variation of the actual and the virtual displacement fields are represented by shape functions as

$$\mathbf{u}(\mathbf{x}, t) = \mathbf{N}(\mathbf{x})\, \mathbf{d}(t) \tag{2.55}$$

$$\tilde{\mathbf{u}}(\mathbf{x}, t) = \tilde{\mathbf{N}}(\mathbf{x})\, \tilde{\mathbf{d}}(t) \tag{2.56}$$

with the shape function matrix $\mathbf{N}(\mathbf{x})$ in the form

$$\mathbf{N} = \begin{bmatrix} N_1 & 0 & N_2 & 0 & \cdots & N_n & 0 \\ 0 & N_1 & 0 & N_2 & \cdots & 0 & N_n \end{bmatrix} \tag{2.57}$$

and $\tilde{\mathbf{N}}$ on a similar form.

The shape functions are inserted in (2.54) which is reformulated using integration by parts in order to obtain a symmetric formulation

$$\begin{aligned} &\int_V \Bigg[\tilde{\boldsymbol{\varepsilon}}^T \boldsymbol{\sigma} + \rho \tilde{\mathbf{u}}^T \ddot{\mathbf{u}} - \rho V^2 \frac{\partial \tilde{\mathbf{u}}}{\partial x}^T \frac{\partial \mathbf{u}}{\partial x} - \rho V \left(\left(\frac{\partial \tilde{\mathbf{u}}}{\partial x} \right)^T \dot{\mathbf{u}} - \tilde{\mathbf{u}}^T \frac{\partial \dot{\mathbf{u}}}{\partial x} \right) \\ &+ (\beta_1 + \beta_2 + \beta_3)\rho \left(\tilde{\mathbf{u}}^T \dot{\mathbf{u}} + \frac{1}{2} V \left(\left(\frac{\partial \tilde{\mathbf{u}}}{\partial x} \right)^T \mathbf{u} - \tilde{\mathbf{u}}^T \frac{\partial \mathbf{u}}{\partial x} \right) \right) \\ &+ (\beta_1\beta_2 + \beta_1\beta_3 + \beta_2\beta_3)\rho \tilde{\mathbf{u}}^T \mathbf{u} + \tilde{\mathbf{u}}^T \mathcal{L}_0(t) * u(t) \Bigg] dV \\ &= \int_S \left[\tilde{\mathbf{u}}^T \boldsymbol{\sigma} \mathbf{n} + V^2 \tilde{\mathbf{u}}^T \frac{\partial \mathbf{u}}{\partial x} - V \tilde{\mathbf{u}}^T \dot{\mathbf{u}} - \frac{1}{2}(\beta_1 + \beta_2 + \beta_3) V \tilde{\mathbf{u}}^T \mathbf{u} \right] dS \end{aligned} \tag{2.58}$$

in which dV denotes integration over volume and dS denotes integration over surface areas and $\mathbf{n} = [n_1, n_2, n_3]^T$ denotes the outward unit vector normal to the boundary. The

PML is terminated by Dirchlet conditions, i.e. zero displacement, hence the loaded surface is the only free boundary. Since the load is traveling in the x_1-direction, the velocity dependent terms under the surface integral vanish. The velocity independent term represents the exterior load.

Separating the convolution terms in the constitutive relation C and the operator $\mathcal{D}_0(t)$, the following set of ordinary differential equations is obtained

$$\mathbf{M}\ddot{\mathbf{u}} + \mathbf{Z}\dot{\mathbf{u}} + \mathbf{K}\mathbf{u} + \mathbf{g} = \mathbf{f} \tag{2.59}$$

where $\mathbf{u}$ is the global displacement vector and $\mathbf{f}$ is the global force vector, assumed to represent surface loads, whereby

$$\mathbf{f} = \int_S \tilde{\mathbf{N}}^T \boldsymbol{\sigma}\mathbf{n}\, dS \tag{2.60}$$

The element mass, damping and stiffness matrices are given by

$$\begin{aligned}
\mathbf{M} &= \int_V \rho\tilde{\mathbf{N}}^T\mathbf{N}dV \\
\mathbf{Z} &= \int_V -\rho V(\tilde{\mathbf{N}}_x^T\mathbf{N} - \tilde{\mathbf{N}}^T\mathbf{N}_x) + \rho(\beta_1+\beta_2+\beta_3)\tilde{\mathbf{N}}^T\mathbf{N}dV \\
\mathbf{K} &= \int_V \Big\{\tilde{\mathbf{B}}^T\mathbf{C}\mathbf{B} - \rho V^2\tilde{\mathbf{N}}_x^T\mathbf{N}_x + \tfrac{1}{2}\rho V\,(\beta_1+\beta_2+\beta_3)\left(\tilde{\mathbf{N}}_x^T\mathbf{N} - \tilde{\mathbf{N}}^T\mathbf{N}_x\right) \\
&\quad + \rho(\beta_1\beta_2+\beta_1\beta_3+\beta_2\beta_3)\tilde{\mathbf{N}}^T\mathbf{N}\Big\}dV
\end{aligned} \tag{2.61}$$

where $\mathbf{B}$ denotes the strain-displacement matrix and $\mathbf{N}$ the shape functions with x-derivative $\mathbf{N}_x = \partial\mathbf{N}/\partial x$. Following Matzen [2011], the convolution integrals from the constitutive relation, representing artificial damping in the PML, are now associated with the nodal displacements, whereby the corresponding vector $\mathbf{g}$ takes the form

$$\begin{aligned}
\mathbf{g} &= \mathbf{K}_{12/3}\,\mathcal{F}_{12/3} * \mathbf{u}(t) + \mathbf{K}_{23/1}\,\mathcal{F}_{23/1} * \mathbf{u}(t) + \mathbf{K}_{13/2}\,\mathcal{F}_{13/2} * \mathbf{u}(t) + \mathbf{K}_1\,\mathcal{H}_1 * \mathbf{u}(t) \\
&+ \mathbf{K}_2\,\mathcal{H}_2 * \mathbf{u}(t) + \mathbf{K}_3\,\mathcal{H}_3 * \mathbf{u}(t) + \mathbf{M}\mathcal{L}_0(t) * \mathbf{u}(t)
\end{aligned} \tag{2.62}$$

where the element matrices $\mathbf{K}_p$ and $\mathbf{K}_{pq/r}$ are given by

$$\begin{aligned}
\mathbf{K}_p &= -\int_\Omega \mathbf{B}^T\mathbf{C}_p\mathbf{B}\, dV\,, \quad p = 1,2,3 \\
\mathbf{K}_{pq/r} &= -\int_\Omega \mathbf{B}^T\mathbf{C}_{pq/r}\mathbf{B}\, dV\,, \quad p,q,r = 1,2,3, \quad p \neq q \neq r
\end{aligned} \tag{2.63}$$

and the convolution terms $\mathcal{F}_{pq/r}$ and $\mathcal{H}_p$ are given by

$$\begin{aligned}\mathcal{F}_{pq/r} * \mathbf{u}(t) &= \int_0^t \frac{1}{\beta_r}(\beta_q - \beta_r)(\beta_p - \beta_r)e^{-\beta_r \tau}\,\mathbf{u}(t-\tau)d\tau \\ &+ \int_0^t \frac{1}{2}\frac{\beta_p \beta_q}{\beta_r}\,\mathbf{u}(t-\tau)d\tau, \quad p,q,r = 1,2,3, \quad p \neq q \neq r \end{aligned} \tag{2.64a}$$

$$\mathcal{H}_p * \mathbf{u}(t) = \int_0^t \frac{1}{2}\beta_p\,\mathbf{u}(t-\tau)d\tau, \quad p = 1,2,3 \tag{2.64b}$$

For convenience, the sum of integrals in (2.64a) are divided into two functions

$$\mathcal{F}^a_{pq/r} * \mathbf{u}(t) = \int_0^t \frac{1}{\beta_r}(\beta_q - \beta_r)(\beta_p - \beta_r)e^{-\beta_r \tau}\,\mathbf{u}(t-\tau)d\tau \tag{2.65a}$$

$$\mathcal{F}^b_{pq/r} * \mathbf{u}(t) = \int_0^t \frac{1}{2}\frac{\beta_p \beta_q}{\beta_r}\,\mathbf{u}(t-\tau)d\tau \tag{2.65b}$$

with $p,q,r = 1,2,3, \quad p \neq q \neq r$ such that

$$\mathcal{F}_{pq/r} * \mathbf{u}(t) = \mathcal{F}^a_{pq/r} * \mathbf{u}(t) + \mathcal{F}^b_{pq/r} * \mathbf{u}(t) \tag{2.66}$$

Thus, the convolution functions in (2.45), (2.47b), (2.65a) and (2.65b) can be presented in one of the following two general forms

$$Q^1 * \mathbf{u}(t) = \int_0^t ae^{-b\tau}\mathbf{u}(t-\tau)d\tau \tag{2.67a}$$

$$Q^2 * \mathbf{u}(t) = \int_0^t c\mathbf{u}(t-\tau)d\tau \tag{2.67b}$$

In the integrals, the argument τ and $t-\tau$ can be interchanged and differentiation with respect to t leads to

$$\frac{d}{dt}\left(Q^1 * \mathbf{u}(t)\right) = a\mathbf{u}(t) - b\left(Q^1 * \mathbf{u}(t)\right) \tag{2.68a}$$

$$\frac{d}{dt}\left(Q^2 * \mathbf{u}(t)\right) = c\mathbf{u}(t) \tag{2.68b}$$

When using this form, the functions $\mathbf{v}(t) = Q^1 * \mathbf{u}(t)$ and $\mathbf{w}(t) = Q^2 * \mathbf{u}(t)$ with dimension of displacement, can be considered as state-space variables and can be updated explicitly via a finite difference approximation. Applying a central difference, the solution to the differential equations in (2.67) are given by

$$\frac{1}{2\Delta t}\left(\mathbf{v}^{n+1} - \mathbf{v}^{n-1}\right) + b\mathbf{v}^n = a\mathbf{u}^n \tag{2.69a}$$

$$\frac{1}{2\Delta t}\left(\mathbf{w}^{n+1} - \mathbf{w}^{n-1}\right) = c\mathbf{u}^n \tag{2.69b}$$

Thus, the solution to Equation (2.65a) is found using (2.69a) and solutions to Equations (2.45), (2.47b), and (2.65b) are found using (2.69b). Doing this, the solution of g^{n+1} can be written in discrete format as

$$\begin{aligned} g^{n+1} &= \mathbf{K}_{12/3}\left(v_{12/3}^{n+1} + w_{12/3}^{n+1}\right) + \mathbf{K}_{23/1}\left(v_{23/1}^{n+1} + w_{23/1}^{n+1}\right) + \mathbf{K}_{13/2}\left(v_{13/2}^{n+1} + w_{13/2}^{n+1}\right) \\ &+ \mathbf{K}_1 w_1^{n+1} + \mathbf{K}_2 w_2^{n+1} + \mathbf{K}_3 w_3^{n+1} + \mathbf{M} w_{\mathcal{L}_0}^{n+1} \end{aligned} \tag{2.70}$$

2.3.1 Correction for moving frame

The translation of the coordinate system leads to terms proportional to V and V^2 in (2.53). These terms make the equations loose the original self-adjointness. In principle this can be compensated for by a modification of the shape functions. However, in the present problem it is simpler to use a technique developed by Krenk et al. [1999] in which the terms $2\rho V\dot{\mathbf{u}}_x$ and $\rho V(\beta_1 + \beta_2)\mathbf{u}_x$ are modified to account for the convection effect. A Taylor series expansion demonstrates that a straight-forward Galerkin representation of these terms implies an error illustrated by the two-term Taylor expansion

$$\dot{\mathbf{u}}_x \simeq \frac{-\Delta\dot{\mathbf{u}}}{h} + \frac{1}{2}h\dot{\mathbf{u}}_{xx} \tag{2.71}$$

where h denotes the length of the increment Δx in the opposite direction of the load velocity. The subscripts $(\,)_x$ and $(\,)_{xx}$ refers to first and second derivative with respect to x. The first term on the right hand side of (2.71) is already properly represented by linear interpolation, hence the second term should be inserted in (2.53) for an improved formulation. The same procedure is used for the term $\rho V(\beta_1 + \beta_2)\mathbf{u}_x$ and insertion of the terms of improvement in Eq. (2.53) yields

$$\begin{aligned} \boldsymbol{\partial}^T\bar{\boldsymbol{\sigma}} - \rho\Bigg(&\frac{\partial^2\mathbf{u}}{\partial t^2} + V^2\frac{\partial^2\left(\mathbf{u} - (h/V)\dot{\mathbf{u}} - \frac{1}{2}(h/V)(\beta_1+\beta_2+\beta_3)\mathbf{u}\right)}{\partial x^2} \\ &-2V\frac{\partial\dot{\mathbf{u}}}{\partial x} + (\beta_1+\beta_2+\beta_3)\frac{\partial\mathbf{u}}{\partial t} - (\beta_1+\beta_2+\beta_3)V\frac{\partial\mathbf{u}}{\partial x} + \\ &(\beta_1\beta_2+\beta_1\beta_3+\beta_2\beta_3)\mathbf{u} + \mathcal{L}_0(t) * u(t)\Bigg) \end{aligned} \tag{2.72}$$

The introduction of the correction terms yields an extra contribution to the volume terms of the damping and stiffness matrix. The additional volume damping and stiffness matrices are

$$\begin{aligned} \mathbf{Z}_V &= h\int_V \rho V\tilde{\mathbf{N}}_x^T\mathbf{N}_x\,dV \\ \mathbf{K}_V &= h\int_V \tfrac{1}{2}\rho V(\beta_1+\beta_2+\beta_3)\tilde{\mathbf{N}}_x^T\mathbf{N}_x\,dV \end{aligned} \tag{2.73}$$

The effect of the improved formulation is an additional convection term proportional to the second order derivative in space added to the full system in terms of damping and to the boundary layer in terms of stiffness. A suitable value for the convection correction parameter h was found by Krenk et al. [1999] to be around $0.3 - 0.4$ times the length of the elements in the x-direction.

2.3.2 Time integration

The first and second order time derivatives are approximated using a central difference scheme which is of second order accuracy

$$\dot{\mathbf{u}} \simeq \frac{\mathbf{u}^{n+1} - \mathbf{u}^{n-1}}{2\Delta t} \tag{2.74a}$$

$$\ddot{\mathbf{u}} \simeq \frac{\mathbf{u}^{n+1} - 2\mathbf{u}^{n} + \mathbf{u}^{n-1}}{\Delta t^2} \tag{2.74b}$$

where Δt is the time step. The displacements, external load vector and convolution vector are approximated using a weighted average

$$\mathbf{u} \simeq \beta\mathbf{u}^{n+1} + (1-2\beta)\mathbf{u}^{n} + \beta\mathbf{u}^{n-1} \tag{2.75a}$$

$$\mathbf{f} \simeq \beta\mathbf{f}^{n+1} + (1-2\beta)\mathbf{f}^{n} + \beta\mathbf{f}^{n-1} \tag{2.75b}$$

$$\mathbf{g} \simeq \beta\mathbf{g}^{n+1} + (1-2\beta)\mathbf{g}^{n} + \beta\mathbf{g}^{n-1} \tag{2.75c}$$

where β is a parameter that takes a value between 0 and 1. Note that the symbol β is used since it refers to the Newmark-Beta method, thus it does not relate to the attenuation function used with PML. Substitution of Equation (2.74)-(2.75) into the equation of motion (2.59) leads to the Newmark-Beta time integration scheme (Newmark [1959])

$$\begin{aligned}
&\left(\frac{1}{\Delta t^2}\mathbf{M} + \frac{1}{2\Delta t}\mathbf{Z} + \beta\mathbf{K}\right)\mathbf{u}^{n+1} \\
&= \left(\frac{2}{\Delta t^2}\mathbf{M} - (1-2\beta)\mathbf{K}\right)\mathbf{u}^{n} - \left(\frac{1}{\Delta t^2}\mathbf{M} - \frac{1}{2\Delta t}\mathbf{Z} + \beta\mathbf{K}\right)\mathbf{u}^{n-1} \\
&\quad - \beta\mathbf{g}^{n+1} - (1-2\beta)\mathbf{g}^{n} - \beta\mathbf{g}^{n-1} + \beta\mathbf{f}^{n+1} + (1-2\beta)\mathbf{f}^{n} + \beta\mathbf{f}^{n-1}
\end{aligned} \tag{2.76}$$

The parameter, β, controls the interpolation between explicit and implicit time integration schemes. Explicit time integration can be an advantage if the matrix on the left hand side can be represented in a diagonal form. In that case, time integration can be performed without solving a linear equation system at each time step. However, the time step size Δt is bounded by the CFL condition. In contrary, implicit methods are

not limited in terms of the time step. And due to the presence of the damping matrix $\mathbf{Z}$ the left hand side of (2.76) can not be represented as a diagonal matrix. Hence, the time integration scheme must be solved implicitly. The 3D formulation of the equation of motion with PML in a moving frame of reference is implemented in Matlab following the algorithm presented in Algorithm 1.

Algorithm 1 PML formulation in moving coordinates

1: Specify domain and PML size, load area and parameters in (2.78)
2: Generate mesh
3: Initialize $\mathbf{u}, \Delta t, V$
4: Build matrices $\mathbf{K}, \mathbf{M}, \mathbf{Z}$ ▷ eq. (2.61), (2.73)
5: $t = 0$
6: **for** $t = t_1 : t_{max}$ **do**
7: update $\mathbf{u}_n$, $\mathbf{u}_{n-1}$, $\mathbf{g}_n$, $\mathbf{g}_{n-1}$, $\mathbf{f}_n$, $\mathbf{f}_{n-1}$ from previous time
8: Calculate $\mathbf{f}_{n+1}$ ▷ eq. (2.60)
9: Calculate $\mathbf{g}_{n+1}$ ▷ eq. (2.70)
10: Solve for $\mathbf{u}_{n+1}$ ▷ eq. (2.76)
11: **end for**
12: Post processing

2.4 Dynamic modeling of pavements

The finite element formulation of elastic wave propagation in convected coordinates with PML as absorbing boundaries, presented in the previous sections, is to be used to simulate pavements subjected to dynamic surface loading. As mentioned in the introduction, a pavement structure is typically modelled as a three layer structure consisting of asphalt concrete on top, granular base layer underneath and subgrade at the bottom. In the modeling, all layers are considered fully bonded and are distinguished by the material properties given to the layers. Debonding between layers is more often an issue in jointed concrete pavements caused by vertical detachment of the concrete plates at the joints which is not in the current scope of this thesis.

The subgrade may consist of several types of material depending on local conditions and the soil modulus may increase with depth (Nazarian et al. [1987]). In the developed model, non-linearity of the subgrade is taken into account by introducing an exponential variation of Young's modulus as function of depth given by (Ullidtz [1998])

$$E(z) = E_0 \left(\frac{z}{z_0} \right)^{\alpha} \tag{2.77}$$

in which E_0 is the modulus at the top of the subgrade, z is the depth, z_0 is a reference depth and $\alpha \geq 0$ is the exponent governing the exponential rate of increase in modulus. In the discrete model, E is considered constant for each element and the modulus value is determined using the z-coordinate at the center of the element.

The application of the model is focused on surface displacements. Thus, it is of importance to have a high resolution of the displacement field in the area around the applied load. However, simulations in a three-dimensional domain of high resolution quickly becomes computational expensive. Hence, it is beneficial to limit the area of high resolution to an area of interest. For this purpose a method of efficient mesh generation is developed. This method is presented in the following section.

2.4.1 Mesh generation

This section presents a method for generating a finite element mesh that balances computational time and numerical accuracy. For the problem at hand, waves generated at the surface propagate into the medium while decaying with increasing distance from the source. Accordingly, an efficient mesh capturing this behaviour consists of placing the smallest elements near the load center and then placing larger and larger elements as distance increases. Such a domain discretization approach is presented in Figure 2.4. More specifically, the mesh generation strategy devised herein is governed by

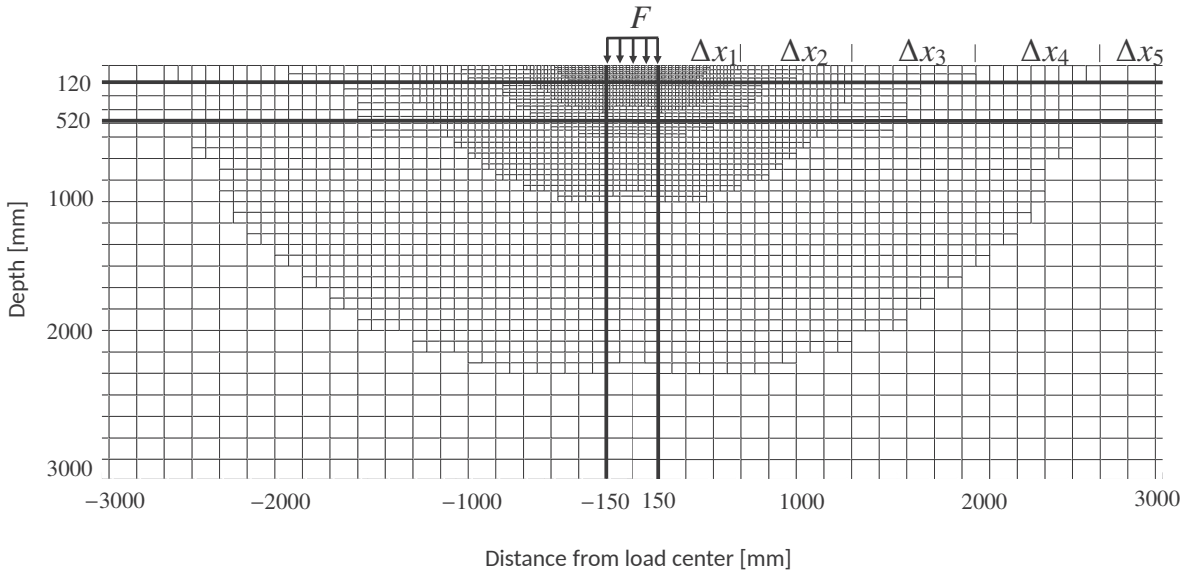

Figure 2.4: Illustration of elements increasing in size with distance from the loading area. PML situated outside this region of the computational domain.

four parameters: a minimum element size Δx_{min}, a maximum element size Δx_{max}, a

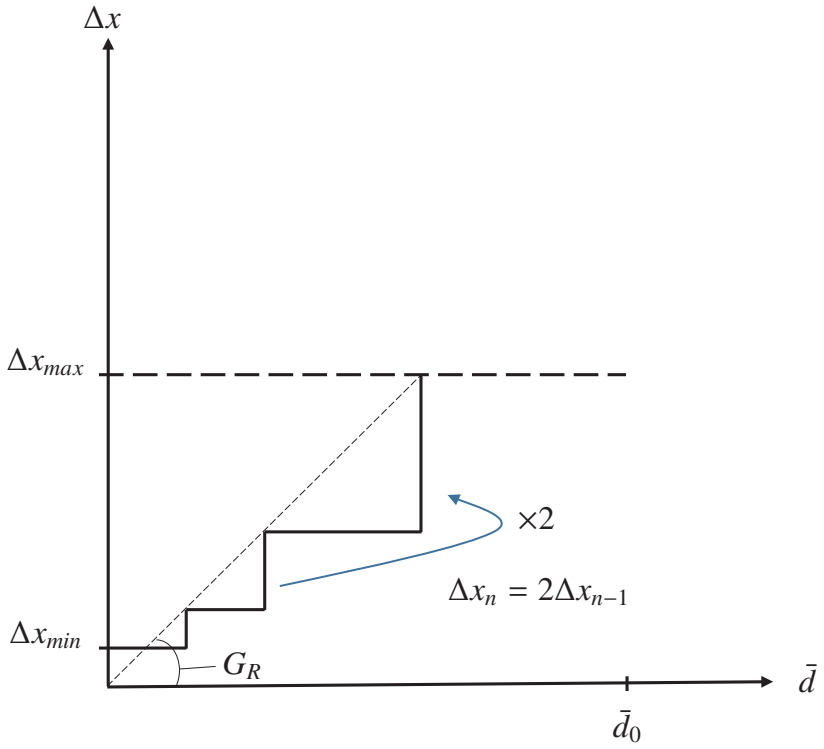

Figure 2.5: Chart of mesh generation parameters.

growth rate parameter G_R, and an overall domain size $\bar{d}_0$. From an initial (minimum) element size Δx_{min} the elements double in size as a function of their distance from the load center, $\bar{d}$, until reaching a maximum element size Δx_{max}. From this point onward, until the domain boundary $\bar{d}_0$ is approached, the size of all elements remain Δx_{max}. In this scheme the G_R parameter controls the 'rate' at which element size is doubled. All four mesh controlling parameters are illustrated graphically in Figure 2.5 which depicts element side length Δx versus distance $\bar{d}$. The maximum element size at any point in the mesh as a function of the distance $\bar{d}$ and the parameters Δx_{min}, Δx_{max} and G_R is given by

$$\Delta \mathbf{x}(\bar{d}) \leq min\left(\Delta \mathbf{x}_{max},\, max\left(\Delta \mathbf{x}_{min},\, G_R \bar{d}\right)\right) \tag{2.78}$$

Additional restrictions in the mesh generation, not presented in the figure, are applied to ensure that none of the elements cross the interface between two adjacent layers and that the load is distributed over an integer number of elements.

The specific method for building the mesh is the following:

- Build a base grid consisting of one element for each area such that no elements cross the interface between two adjacent layers and the load is distributed over an integer number of elements. The base grid is illustrated in figure 2.4 as the thick lines, dividing the mesh into nine elements in this case of a three layer structure.

- The elements of the grid are recursively divided into smaller elements until all elements satisfy the condition defined by Equation (2.78). Elements are always divided along the longest side of the element.

An algorithm for generating the mesh is given in Algorithm 2, wherein n_{el} denotes an element and N_{el} is the total number of elements in the mesh. The method is suitable for mesh generation in both 2D and 3D.

Algorithm 2 Mesh generation algorithm

```
Build base grid
n_el = 1
while n_el ≤ N_el do
    Calculate Δx = [Δx, Δy, Δz]
    Calculate Δx_lim = min(Δx_max, max(Δx_min, G_R d̄))        ▷ eq. (2.78)
    if Δx > Δx_lim then
        Select axis for division: max(Δx)
        Divide element in the middle
        Add the new element to element topology → N_el=N_el+1
    else
        n_el = n_el + 1
    end if
end while
```

2.4.1.1 Method of Lagrange multipliers

A consequence of generating a mesh with above presented method is the occurrence of a number of so-called 'free nodes'. Free nodes are not connected to neighbour nodes in all directions (disregarded the nodes on the boundary). The problem is illustrated in Figure 2.6a. Following Cook et al. [2002], the displacements of the free nodes need to be restricted by their neighbour nodes (see Figure 2.6b). Hence an extra set of constraint equations are added to the equation, which for bilinear elements is a linear interpolation between neighbouring nodes

$$\frac{1}{2}u_{n+1} + \frac{1}{2}u_{n-1} - u_n = 0 \tag{2.79}$$

where u_n is the displacement of the free node n, u_{n+1} and u_{n-1} are the displacements of the neighbouring nodes to node n. The constraint equation (2.79) can be written on the form

$$\mathbf{Au} - \mathbf{Q} = \mathbf{0} \tag{2.80}$$

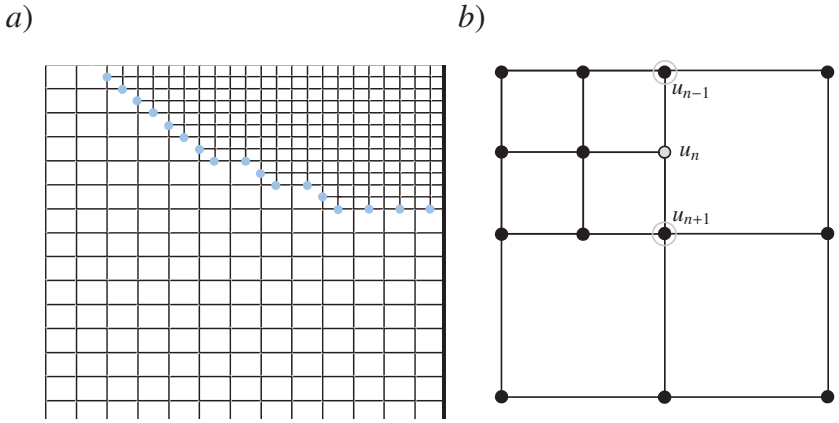

Figure 2.6: Free nodes indicated with dots in a) and free node u_n and its neighbours u_{n-1} and u_{n+1} in b).

where **A** is the Jacobian of the constraints, **Q** contain constants and **u** is the displacement vector. There are more degrees of freedom in **u** than constraint equations, so **A** has more columns than rows. Following Cook et al. [2002], Lagrange multipliers can be used to impose the constraints by multiplying the left hand side of the constraint equation (2.80) by a row vector $\boldsymbol{\lambda}^T$ that contains as many Lagrange multipliers as there are constraints. This expression is added to the expression of potential energy of the system yielding

$$\Pi_p = \frac{1}{2}\mathbf{u}^T\mathbf{S}\mathbf{u} - \mathbf{u}^T\mathbf{R} + \boldsymbol{\lambda}^T(\mathbf{A}\mathbf{u} - \mathbf{Q}) \tag{2.81}$$

in which **S** represents the left hand side of the system of equations in (2.76) and **R** is the corresponding right hand side. The expression in parentheses is zero so 'nothing' is added to the standard formulation of potential energy (Cook et al. [2002]). Now Π_p is made stationary by using the equations $\partial\Pi_p/\partial\mathbf{u} = 0$ and $\partial\Pi_p/\partial\boldsymbol{\lambda} = 0$ which are obtained on a matrix form as

$$\begin{bmatrix} \boldsymbol{S} & \boldsymbol{A}^T \\ \boldsymbol{A} & \mathbf{0} \end{bmatrix}\begin{bmatrix} \boldsymbol{u} \\ \boldsymbol{\lambda} \end{bmatrix} = \begin{bmatrix} \boldsymbol{R} \\ \boldsymbol{Q} \end{bmatrix} \tag{2.82}$$

The new system of equations is solved for both the displacements and the Lagrange multipliers. The Lagrange multipliers are not used in the further analysis but can be interpreted as the force of constraint applied through the neighboring nodes. Since the constraint equations are all given by Equation (2.79), the vector **Q** is a zero vector. If elements of higher order are used, Eq. (2.79) is modified such that the displacement of the free node is interpolated according to the given shape function.

2.5 Main findings

In this section, numerical examples are presented to demonstrate the absorbing properties of the PML formulated in a moving frame of reference. In that sense the Ricker pulse is used as an example of a moving source. The PML performance is demonstrated for a case of a load applied on a half space (Figure 2.7a) and a load applied on a viscoelastic layer overlying a half space (Figure 2.7b). The effect of load speed is presented in the case of an applied load on a half space. In the case of two layers present, the effect of different ratios between modulus of the two layers are investigated. The results are presented using an implementation of the formulation in 2D. The results are also presented in Paper [P1] along with additional results. Results regarding the implementation in 3D is presented in Section 2.6.

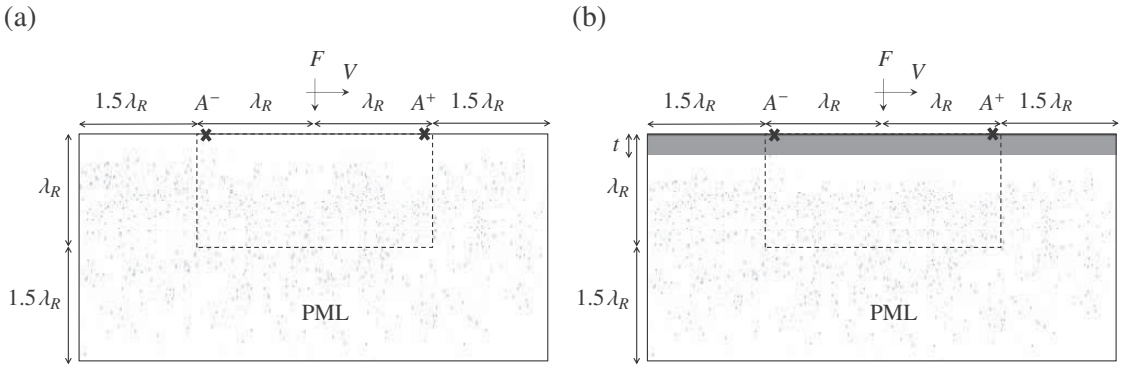

Figure 2.7: Computational domain surrounded by PML for (a) a half space and (b) a viscoelastic layer overlying a half space. Observation points A^+ and A^- are marked by '×'

The numerical examples are based on the single layer half space and the two layer half space sketched in Figure 2.7a and 2.7(b), respectively. The dashed line indicates the interface between the computational domain and the PML. F is the load acting at the center of the surface and V indicates the velocity and travel direction of the load. The load is a Ricker pulse acting in a single point given by

$$F(t) = \tau\left(1-\tau^2\right)^2, \quad -1 \leq \tau \leq 1 \tag{2.83}$$

where $\tau = 2t/T_c - 1$. The duration of the pulse is $T_c = 0.2$s, hence the dominant frequency of the pulse is $f = 1/T_c = 5Hz$. In the numerical examples, the maximum load applied is $F_{max} = 50$ kN. The time history of the Ricker pulse and its Fourier content are given in Figure 2.8.

The computational domain has a width of $2\lambda_R$ and a depth of λ_R , where λ_R is the Rayleigh wave length for the dominant load frequency. The computational domain is surrounded by PML on 3 sides with a width of $d_i = 1.5\lambda_R$. The PML is terminated by Dirichlet boundary conditions. In Paper [P1], a parametric study is carried out

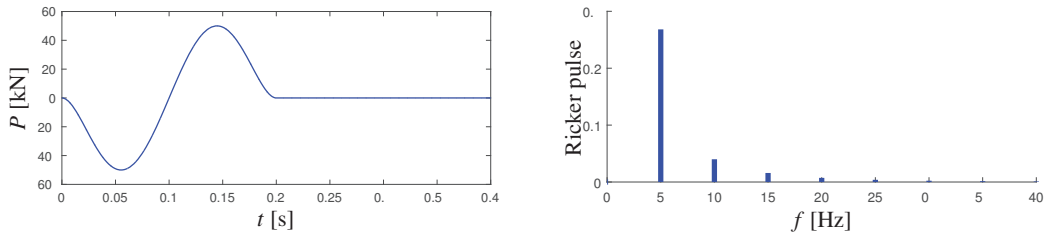

Figure 2.8: Ricker pulse and its Fourier spectrum.

to investigate the best choice of PML parameters for the attenuation function from Equation (2.19), repeated here

$$\beta_j(x_j) = \beta_{\max}\left(\frac{x_j^p}{d}\right)^2 \tag{2.84}$$

in which $\beta_{\max}$ is given by (Matzen [2011])

$$\beta_i^{max} = -\frac{3c_p \log_{10}(R_0)}{2d_i} \tag{2.85}$$

Best parameter values were found to be $R_0 = 10^{-4}$ and $d_i = 1.5\lambda_R$ [P1]. These parameters are used in the following examples.

The response of the pulse is captured in two observation points, A^+ and A^- in front of and behind the load, respectively. The two observation points are located with equal distance to the load on the surface in the computational domain, close to the PML interface. The domain and the PML are discretized with bilinear elements width edge size $\Delta x_1 = \Delta x_2 = 2.57$m. The simulated time is 1.5s and the implicit time integration scheme (2.76) is used with $\beta = 1/4$. The time step is $\Delta t = 0.0071$ s based on the CFL condition

$$\Delta t = \Delta x / c_s \tag{2.86}$$

In the first example presented in Figure 2.9, a Ricker pulse is applied to a single layer half space. The material parameters of the half space are $E = 60$MPa, $\nu = 0.35$ and $\rho = 1800$kg/m^3. The pulse is moving on the surface with different speeds in the horizontal direction. The speed is expressed in relation to the shear wave velocity of the soil as the Mach value

$$\text{Mach} = V/c_s \tag{2.87}$$

referring to subsonic motion as long as the speed is smaller than the shear wave velocity of the soil. Pavement traffic would rarely exceed a speed higher than Mach = 0.4. In the case of a very soft soil with $E = 30$ MPa, Mach=0.4 corresponds to a load speed in the order of $V \simeq 110$km/t. Thus, the example is carried out for Mach = 0, 0.2 and 0.4. The responses obtained in point A^- and A^+ are shown in Figures 2.9a and 2.9b, respectively.

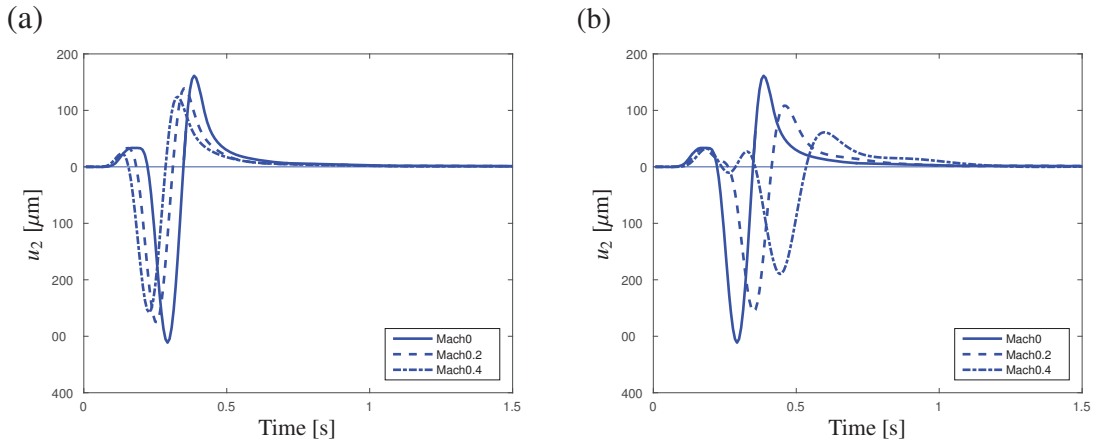

Figure 2.9: Deflection response in points A^- (a) and A^+ (b) for single layer system.

The pulse arrives with the speed $c + V$ behind the load, point A^-, and it arrives with the speed $c - V$ in front of the load, at point A^+. I.e. for a fixed point in front of the moving load the frequency increases while it decreases for a fixed point behind the moving load. The response is seen to decrease with velocity. This is especially clear in front of the load where the maximum deflection decreases by approximately 30%. This is in agreement with the results found by Krenk et al. [1999]. An opposite observation has been made by Metrikine and Dieterman [1999], Hung and Yang [2001] in case of a constant moving load. In this case, the response increases by increasing velocity.

Figure 2.10 depicts the vertical displacement field with snapshots at four instants in time with PML and with fixed boundaries, respectively. The velocity of the moving pulse is $V \simeq 44$m/s. After $10T_c$ corresponding to 2 seconds the wave has been fully absorbed in the PML (top row) while reflections of the wave are present at the same instants in time in the case of fixed boundaries (bottom row).

The effect of different modulus ratios between two layers is investigated in the case of a viscoelastic layer, such as asphalt, being present on top of the half space (Figure 2.7b). The Ricker load is applied with a velocity corresponding to Mach = 0.4 while the elastic modulus of the toplayer varies between E, $10E$ and $100E$ with E being the modulus of the bottom layer. The density of the top layer is $\rho = 2300\text{kg/m}^3$ and Poisson's ratio is $\nu = 0.35$. The effect of impedance ratio between top and bottom layer on the response obtained in A^+ and A^- is shown in Figure 2.11.

A high impedance ratio is seen to have a significant influence on the response obtained in front of the load (Figure 2.11b. The negative displacement peak increases around 13% when the impedance ratio equals 100. This peak also occurs approximately 0.05 s earlier compared to the response obtained in the single layer half space. On the other hand, the response obtained behind the load does not change substantially. The effects observed for the response in front of the load are only seen to a minor degree behind

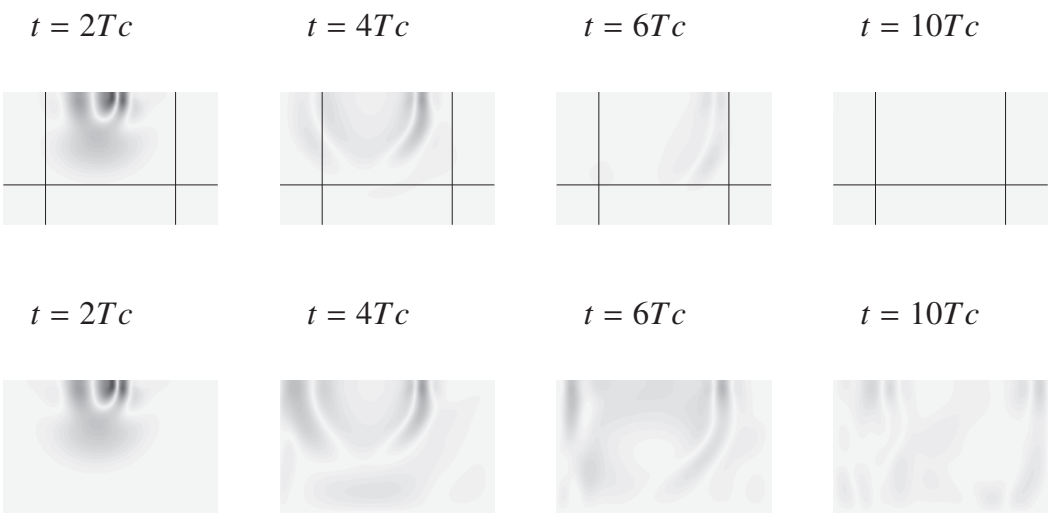

Figure 2.10: Snapshots of the vertical displacement field at four instances of time with Mach=0.4. Top row is with PML boundaries and bottom row is with fixed boundaries

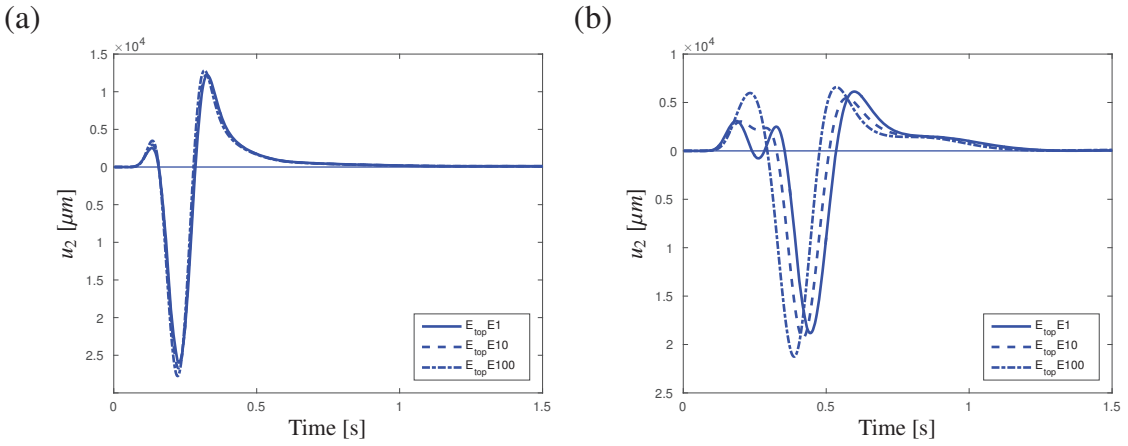

Figure 2.11: Deflection response in points A^- (a) and A^+ (b) for a two layer system with top layer stiffness E, $10E$ and$100E$ at Mach=0.4.

the load.

2.6 Wave propagation in 3D

This section presents results of propagating waves from a load source moving with different velocities in 3D. All examples are obtained from an implementation in Matlab of

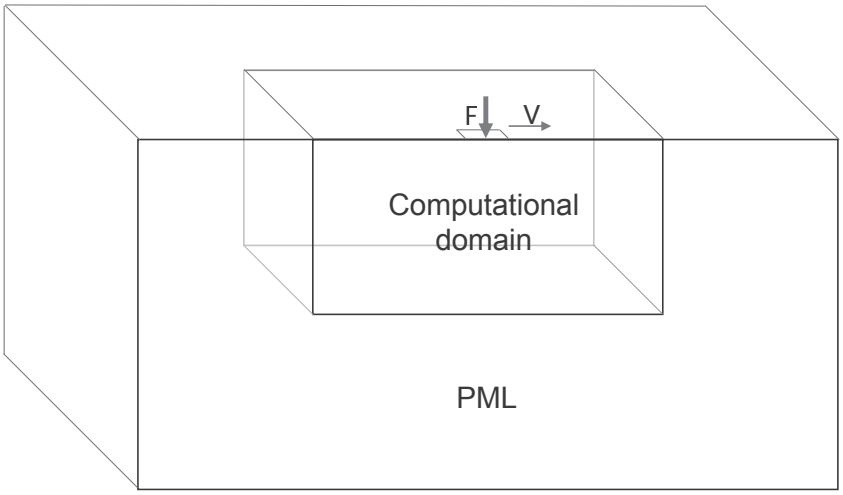

Figure 2.12: 3D sketch; Computational domain surrounded by PML. The load is equally distributed over the indicated area corresponding to two elements.

the equations derived in Section 2.1.3 and 2.3. This implementation considers the main part of the PML ensuring waves to be gradually absorbed in the PML layer. The convolution integrals are disregarded in this version of the implementation; i.e. Equation (2.59) is solved with the convolution vector **g** being equal to zero. In order to take advantage of the full potential of PML, the convolution integrals should be implemented as well, following the procedure given in Section 2.1.3.

In Section 2.6.1, the 3D implementation is verified by simulating waves propagating in two directions for comparison with simulations conducted in 2D. The simulation in a moving frame of reference is verified against a manually moved load in a static frame of reference. The performance of the implemented version of PML is investigated. In Section 2.6.2, propagation of waves in 3D by means of a Ricker load applied on the surface of a halfspace moving with different velocities is illustrated. Wave propagation in 3D is compared with propagating waves in 2D.

All 3D examples are obtained in a mesh as the one illustrated in Figure 2.12 The computational domain and the PML layer are separated in the figure by dashed lines. All examples consider a Ricker load, given by Equation (2.83), applied to the surface of a half space. The load is equally distributed over 2 elements moving in the direction as indicated on the figure.

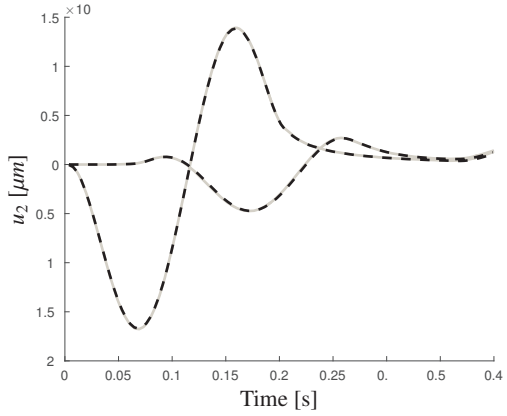

(a) Response from stationary Ricker pulse in 2D (solid) and 3D (dashed).

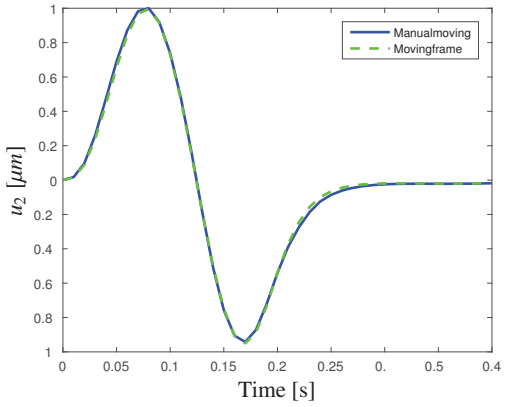

(b) Response from Ricker pulse in moving frame and static frame.

Figure 2.13: a: The response in 2D and 3D is observed in the point of loading and in a point close to the PML interface. b: A Ricker pulse is moving with Mach = 0.2 in a moving and a static frame of reference.

2.6.1 Model verification

The 3D implementation is verified with a line load of 1 m. This corresponds to the 2D example in Figure 2.7a and should thus yield similar result. The Ricker load is not moving and the response is obtained in the point of loading and in a point located 21 m in front of the load (Figure 2.13a). The simulations conducted in 3D and 2D are seen to yield similar results.

The response from a Ricker pulse simulated in a moving frame of reference is superposed the response simulated in a static frame of reference by manually moving the load in Figure 2.13b. The Ricker load is moving with Mach = 0.2 and the response is observed in the front point of the loading area. Responses obtained in a moving frame of reference and by manually moving the load are seen to follow each other closely.

The performance of PML is investigated in Figure 2.14. Figure 2.14 shows the response from a Ricker pulse with PML and with Dirichlet boundaries, respectively. In the case of no PML present, the PML parameters are set equal to zero in the PML layer in Figure 2.12 such that $\beta_1 = \beta_2 = \beta_3 = 0$ and the domain is truncated by Dirichlet conditions only. Figure 2.14b zooms in to the part of Figure 2.14a from $2T_c - 12T_c$. The reflections from the propagated wave with and without PML becomes clear. The PML is seen to absorb well although only the central part of the PML formulation is active. The maximum error is 1% and by $12T_c$ the reflections are almost fully absorbed. Without PML the error reaches 5% and by $12T_c$ reflections are still present with an amplitude of 3%. The absorption abilities of the PML is further demonstrated in Figure

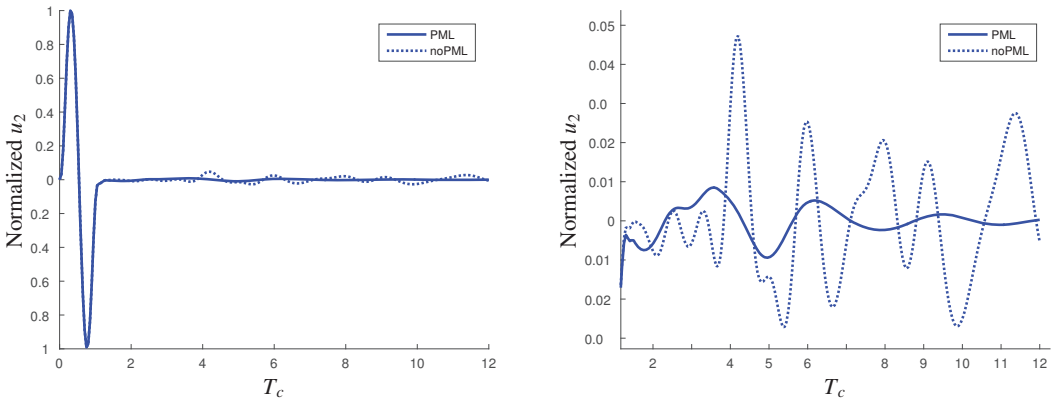

Figure 2.14: Response from Ricker pulse at a point of loading with and without PML.

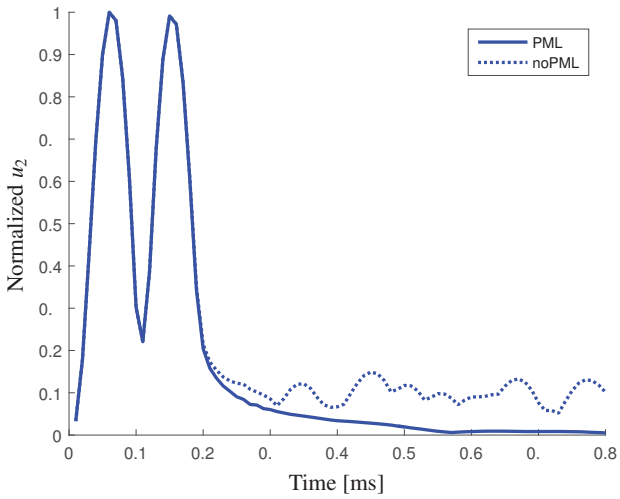

Figure 2.15: Maximum domain response from a Ricker pulse as function of time with and without PML.

2.15 in which the maximum response in the entire domain is presented as a function of time. The response is normalized and presented in the case of PML present and in case of no PML present. In case of PML present, the response is continuously absorbed by the PML and stays close to zero afterwards. In the case of no PML present, fluctuations are present in a more or less steady level after the wave has reached the boundaries. Without PML, for long time simulations of continuous transient loading a large reflection of waves will with increasing effect amplify the response with time which may lead to divergence.

In Figure 2.16 the effect of PML and Dirichlet boundaries, respectively, is illustrated by snapshots of wave propagation. Wave propagation is shown for the three instants of time T_c, $2T_c$ and $4T_c$. The Wave propagates similarly at $t = T_c$ and $t = 2T_c$. At $t = 4T_c$

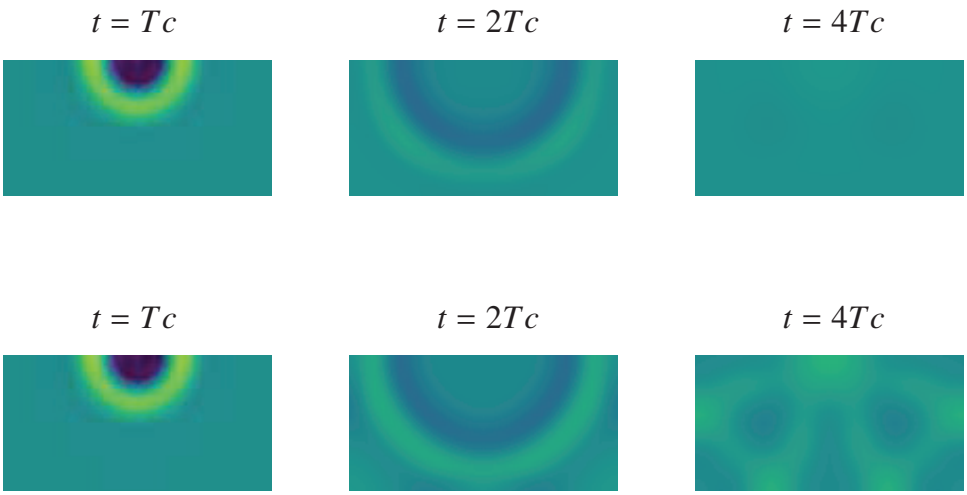

Figure 2.16: Snapshots of the vertical displacement field at three instances of time with Mach=0. Top row is with PML boundaries and bottom row is with Dirichlet boundaries.

it is seen that the wave is well absorbed by PML while reflections are present in the entire domain in the case of Dirichlet boundary conditions.

2.6.2 Wave propagation in 3D compared with 2D

The present section illustrates how waves propagate in 3D when a Ricker load source moving with different speeds is applied. The differences between wave propagation in 2D and 3D are investigated.

Figure 2.17 illustrates the surface of a half space at which a wave propagates from a Ricker load moving with Mach = 0.4. The wave propagation is shown at four instants of time; $1/2T_c$, T_c, $3/2T_c$ and $2T_c$. At $t = 2T_c$ the wave behind the load has almost left the domain, while the wave in front of the load is still fully present inside the domain. Thus, a wave behind the point of loading travels faster backward from the load source compared to the wave in front of the source. This is consistent with Figure 2.9 in Section 2.5 for an equivalent example conducted in 2D. The same effect is visualized in Figure 2.18 where wave propagation is shown for a Ricker load moving with Mach 0, 0.2 and 0.4.

Waves propagate differently in 3D compared to 2D. In 3D waves attenuate with the inverse square law, $1/r^2$ and in 2D waves attenuate by $1/r$. Thus, 3D waves attenuate faster than waves represented in 2D. This is clearly seen in Figure 2.19a which shows

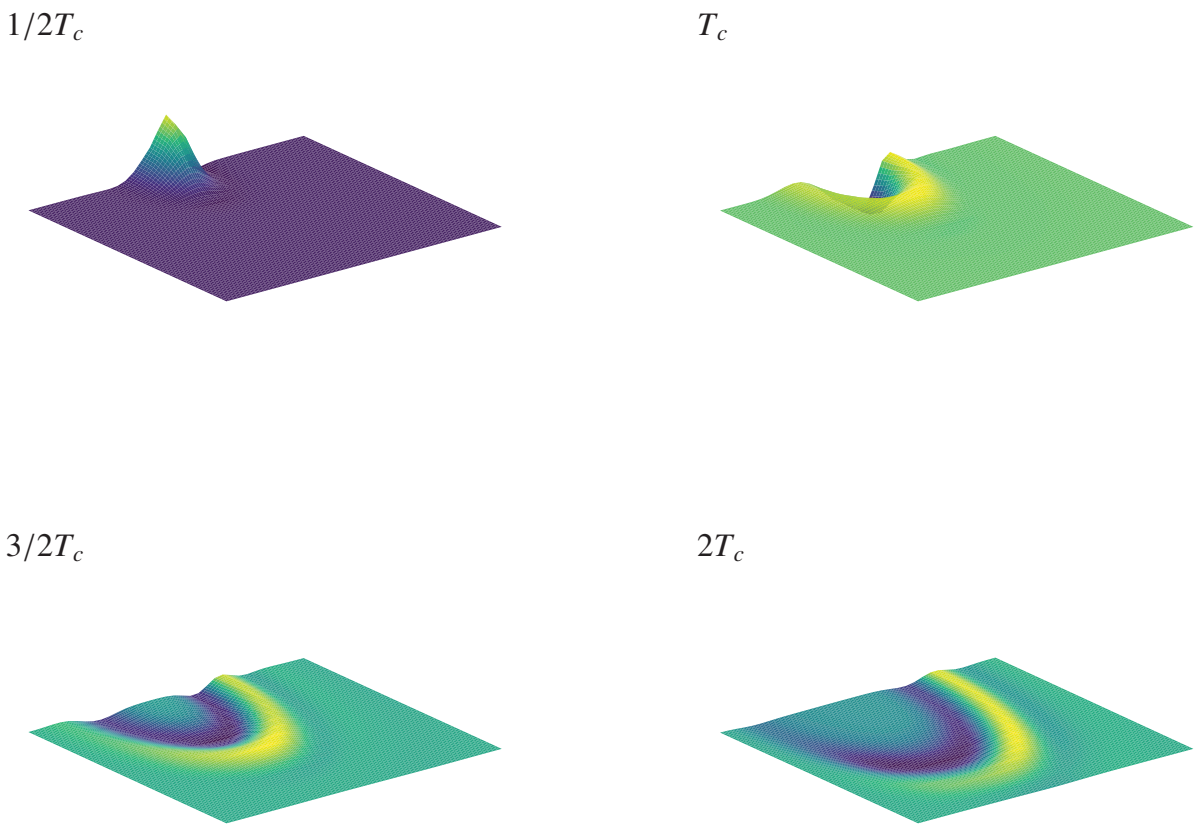

Figure 2.17: Surface wave propagation of a half space subjected to a Ricker load moving with Mach = 0.4

the normalized response from a Ricker pulse with time. The response is observed in the point of loading. Besides experiencing a slower attenuation, the magnitude of the 2D response deviates from the 3D response. While the positive and negative amplitude of the 3D wave are identical, the negative amplitude of the 2D wave is only 80% of the positive amplitude. Moreover, there is a peak delay of the 2D wave compared to the wave in 3D.

Figure 2.19b shows the response in 2D and 3D at the point of the load and 6 m in front of the load. It is here clear that there are significant differences between 2D and 3D waves in terms of both magnitude and attenuation rate at different observation points relative to the source of loading. This is also illustrated in Figure 2.20 showing wave propagation in 2D and 3D at 3 instants of time; $1/2T_c$, $3/2T_c$ and $2T_c$. The color

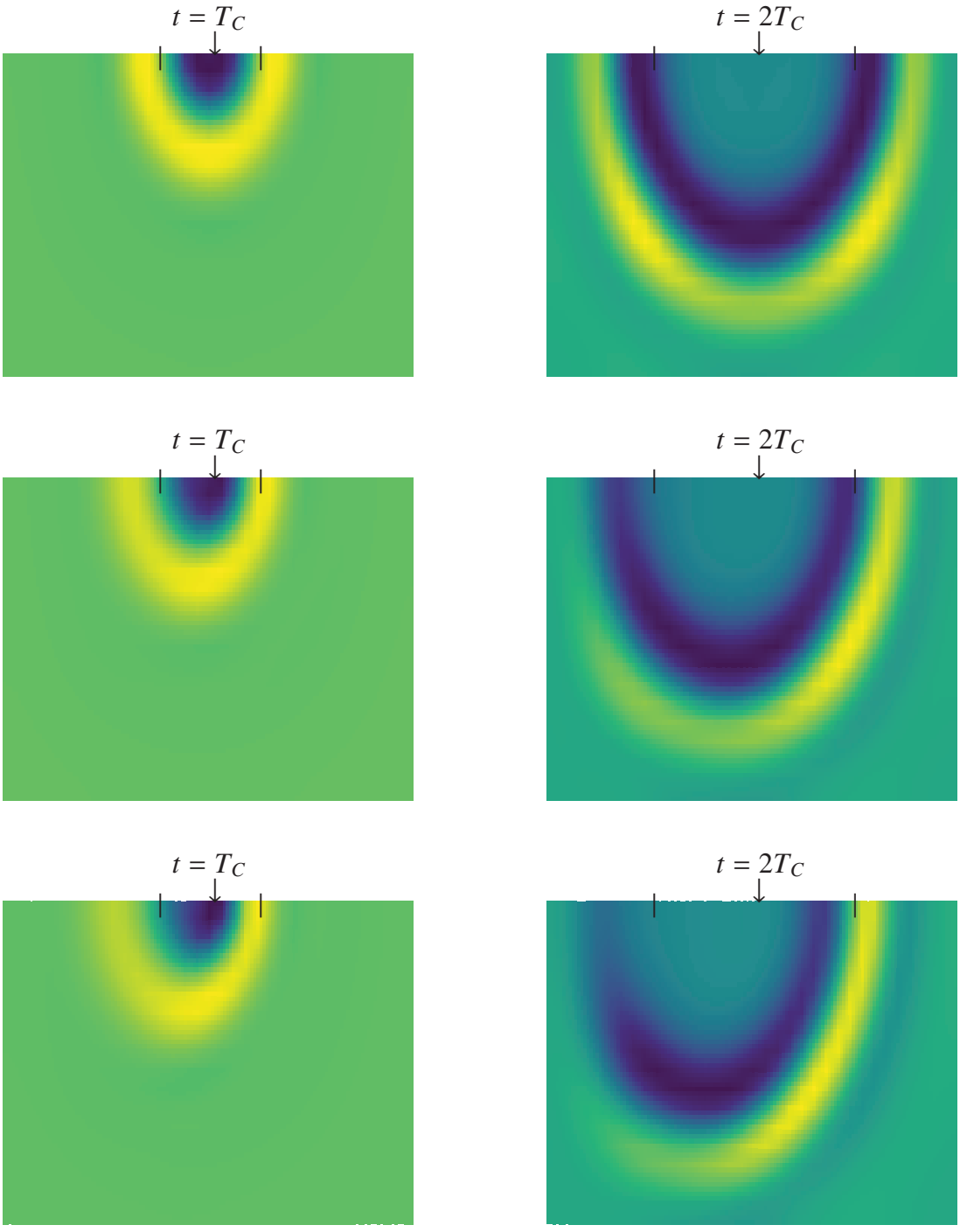

Figure 2.18: Surface wave propagation of half space subjected to a Ricker pulse with velocity Mach0 (top), Mach0.2 (middle) and Mach0.4 (bottom) illustrated at time $t = T_c$ and $t = 2T_c$, respectively. The load is indicated by an arrow.

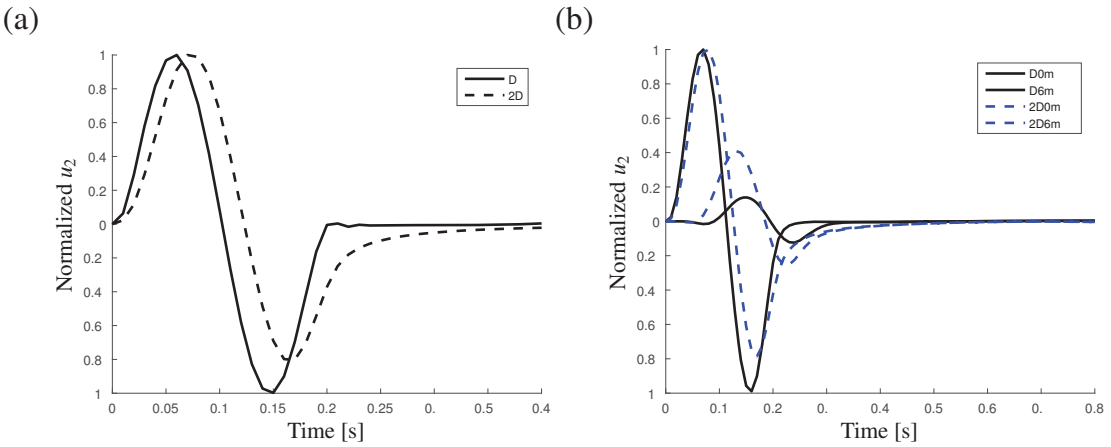

Figure 2.19: Normalized response obtained from a Ricker pulse for 3D (solid) and 2D (dashed); (a) at the point of loading and (b) at the point of loading and 6 m in front of the load.

scale bounds are $\pm 0.1 u_{max}$ where u_{max} refers to the maximum amplitude observed in the simulation in 2D and 3D, respectively.

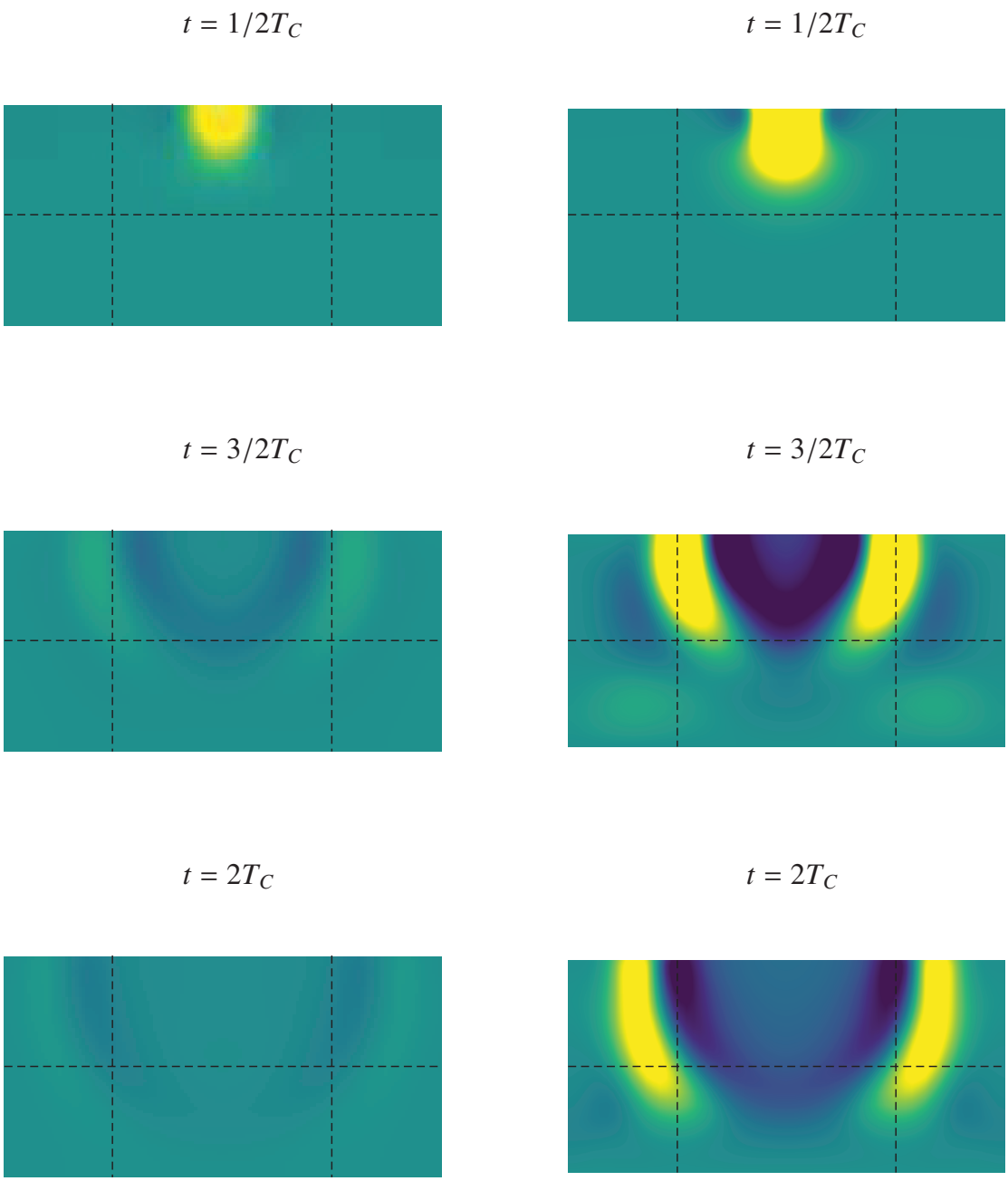

Figure 2.20: Surface wave propagation of half space subjected to a Ricker pulse with velocity Mach0 obtained in 3D (left column) and 2D (right column) illustrated at time instants $t = 1/2T_c$, $t = 3/2T_c$ and $t = 2T_c$, respectively.

Chapter 3

Application to deflection measurements

This chapter deals with modeling and analysis of impact loading generated by a Falling Weight Deflectometer (FWD). An introduction to the FWD device is given in Section 3.1. In section 3.2 the equation of motion is presented in axisymmetric coordinates which is suitable for modeling impact loads. A method for backcalculation of pavement layer properties is developed and used for backcalculation of pavement layer properties based on measurements obtained from FWD experiments. In Section 3.3 the method and algorithm for backcalculation are presented and Section 3.4 presents the results obtained from backcalculation; that is measured deflections fitted with modeled deflections and estimated layer properties of a pavement on which the FWD was applied.

3.1 Falling Weight Deflectometer (FWD)

The Falling Weight Deflectometer is a standard non-destructive testing device for the pavement industry ASTM [2015]. In general terms, an FWD is designed to generate a short load pulse at the pavement surface, in the order of 30–60 milliseconds in duration, and record the associated surface deflections. This type of loading is achieved by dropping a weight from a predetermined height, and the deflections are measured

(a) Falling Weight Deflectometer (FWD).

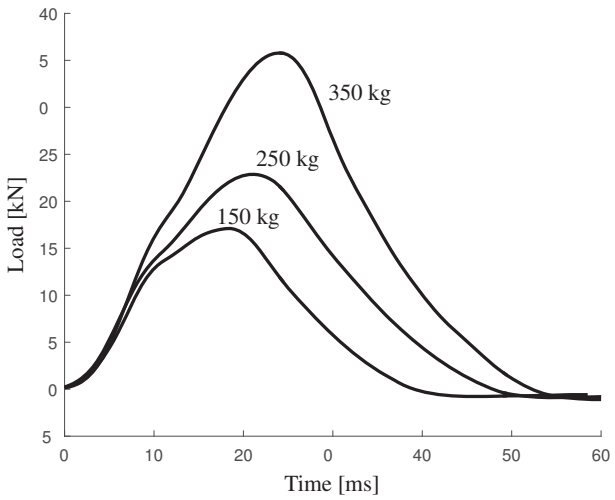

(b) FWD generated load histories.

Figure 3.1: (a) Illustration of an FWD and (b) Three examples of load histories applied to a pavement by an FWD by dropping a weight of 150 kg, 250 kg and 350 kg, respectively, from a 50 mm drop height with 2 buffers.

by an array of sensors called geophones. The mass is dropped on a stiff circular load plate with a diameter of 300 mm in order to equally distribute the load to a known area on the pavement. When a mass is dropped, it slides along two guide rods, having a set of buffers attached underneath it. In any standard FWD device the operator can choose whether to use 2, 4 or 6 buffers for an experiment (see Figure 3.1a). The effect of the buffers is deceleration of the mass to control the shape of the pulse. The shape and magnitude of a load pulse generated by an FWD is thus controlled by three operational parameters; weight of the dropped mass, drop height and number of buffers attached to the mass. Figure 3.1b shows three load pulses generated by an FWD by dropping a mass of 150 kg, 250 kg and 350 kg, respectively, from a 50 mm drop height with 2 buffers. The load pulse is seen to change in terms of both load magnitude and duration of the pulse.

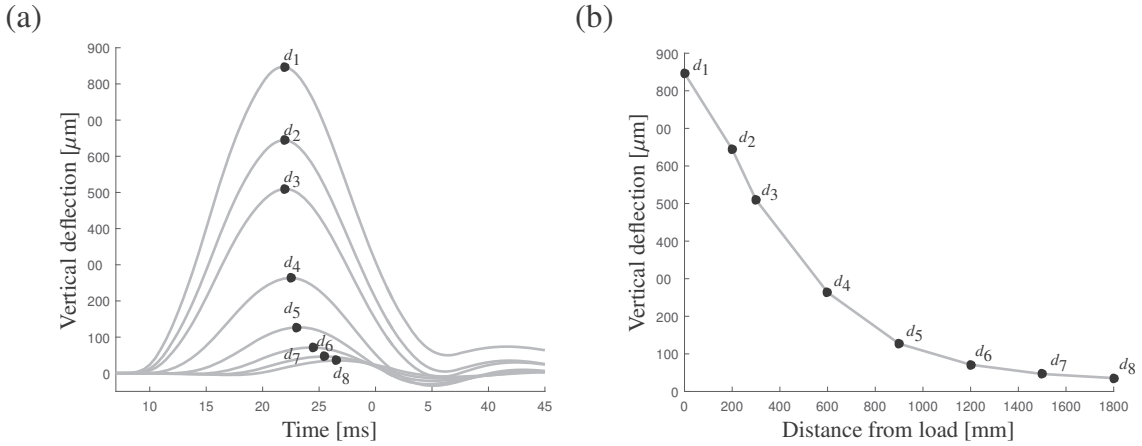

Figure 3.2: (a) Deflection time histories recorded by each of the geophones. (b) Deflection basin generated using the peak values from the deflection time histories in a)

The deflections are typically recorded by 7-10 geophones placed at distances between 0 – 2100 mm from the center of the load plate. An example of deflection time histories recorded by an FWD is shown in Figure 3.2a. In this example, the geophones are placed at the distances; 0, 200, 300, 600, 900, 1200, 1500, 1800 mm. Number $d_1, .., d_8$ in the figure indicate from which geophone the measurements are recorded; d_1 corresponds to the geophone located at the center of the load plate, d_2 is located at a distance of 200 mm from the load plate center and so on. The peak deflection of each curve as function of the recording distance from the load plate is known as the deflection basin (see Figure 3.2b). The deflection basin is thought of as the basin that would be generated by a heavy truck passing by.

In most cases FWD measurements are interpreted with the aim of identifying the in situ mechanical properties of the individual system layers. This is commonly performed by means of backcalculation, wherein model-generated deflections are best matched against field-measured deflections. The mechanical properties can be used to estimate

stresses and strains in the pavement. Based on this, the remaining life of the pavement can be estimated.

3.1.1 FWD Experiments

A total of 24 FWD drops were executed, spanning the full operational range of the device in terms of: drop height, drop mass and number of buffers. The experiments were conducted on a pavement test field build inside a hangar in the end of 2015. All tests were executed within a period of 0.5 hours, during which the AC temperature was 22°C. Figure 3.3 graphically presents the pavement test field; Figure 3.3a presents an overhead view of the testing area and Figure 3.3b presents a cross-sectional view. As may be seen, a portion of the concrete floor in the hangar has been replaced with a 5 m×3 m asphalt pavement consisting of 400 mm granular base layer and 120 mm Asphalt Concrete (AC). The load plate was positioned as seen in Figure 3.3a along with eight geophones placed at the following offset distances (from the center): 0, 200, 300, 600, 900, 1200, 1500 and 1800 mm. Additional information about the construction of the pavement may be found in Paper [P2]. Later, the asphalt pavement section was further investigated to collect more geotechnical characteristics of the subgrade. The investigation included vane testing which displayed a trend of increasing shear resistance with depth, from 125 kN/m^2 close to the subgrade surface to 330 kN/m^2 at a depth of 4 m.

Eight separate FWD tests out of the 24 were selected for further analysis in this study. The associated operational settings and load-time history features are listed in Table 3.1 (numbered sequentially for convenience). The load-time histories are characterised by peak loads varying between 17 kN and 86 kN and load pulse duration spanning in the interval 29.5 – 52.0 ms.

3.2 Pavement modeling

This section is concerned with modeling of an FWD experiment for subsequent analysis. The aforementioned pavement is represented as a fully bonded three layer system as shown in Figure 3.4. In general terms, each layer is assumed to be a linear viscoelastic solid governed by a Kelvin-Voigt type of constitutive relation

$$\boldsymbol{\sigma} = \boldsymbol{C}\boldsymbol{\varepsilon} + \eta \boldsymbol{C}\dot{\boldsymbol{\varepsilon}} \tag{3.1}$$

where $\dot{\boldsymbol{\varepsilon}}$ is the strain-rate tensor and η denotes material damping. In Figure 3.4, the material properties are identified for each layer by subscripts 1, 2 and 3 referring to AC layer, base layer, and subgrade, respectively.

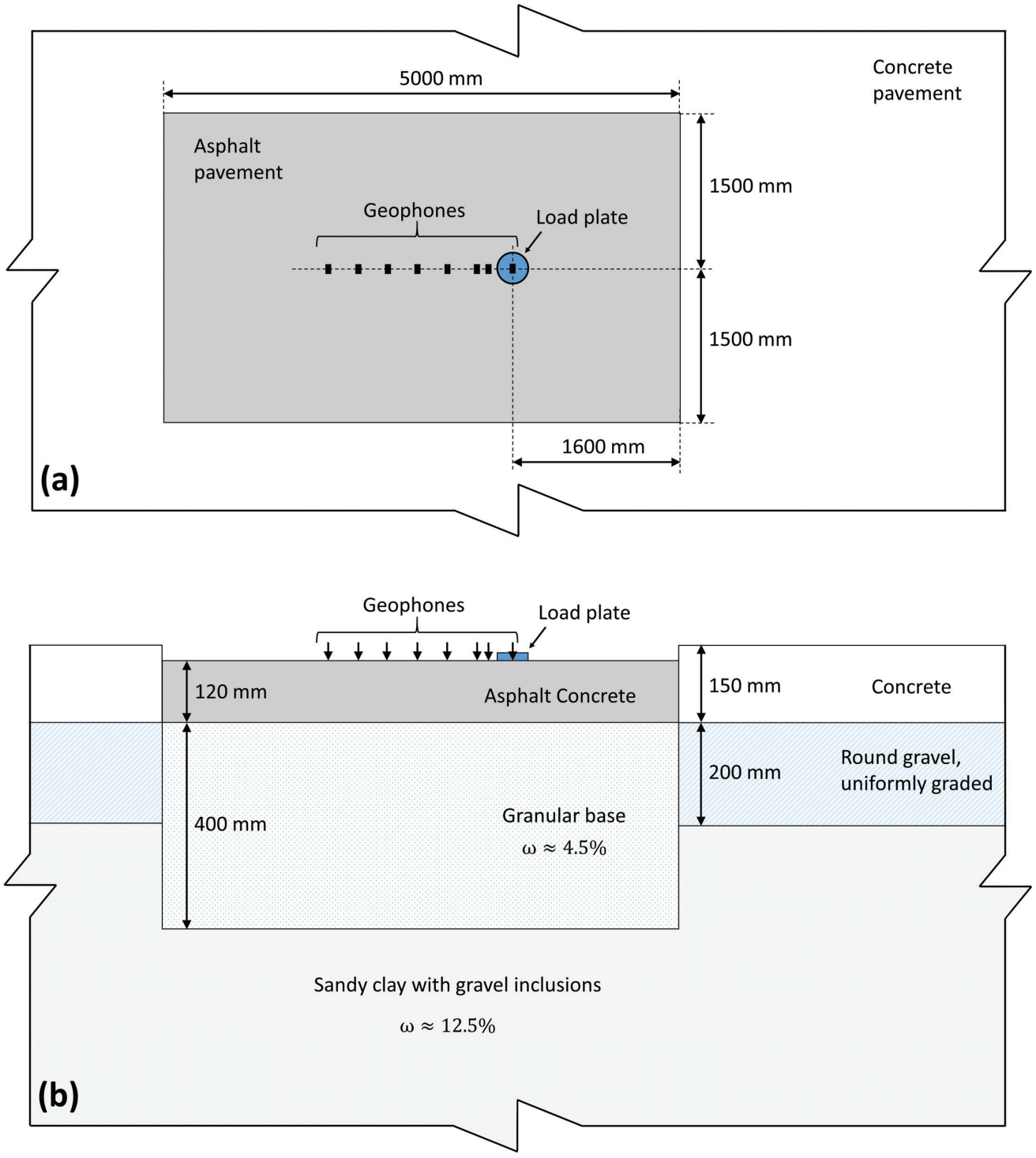

Figure 3.3: FWD testing area: (a) overhead view, and (b) cross-sectional view.

Based on the fact that the vane test conducted on the site showed an increase in shear resistance of the boulder clay with depth, the modulus of the subgrade layer is assumed

Test	Buffers	Weight [kg]	Drop height [mm]	Pulse duration [ms]	Peak load [kN]
1	4	250	400	29.5	86
2	4	250	200	33.0	52
3	4	250	50	37.0	23
4	2	150	100	39.0	17
5	2	250	100	47.5	26
6	2	350	100	52.0	35
7	2	250	175	44.0	35
8	6	350	50	35.5	35

Table 3.1: Selected FWD drop experiments: Pulse features and device operational settings.

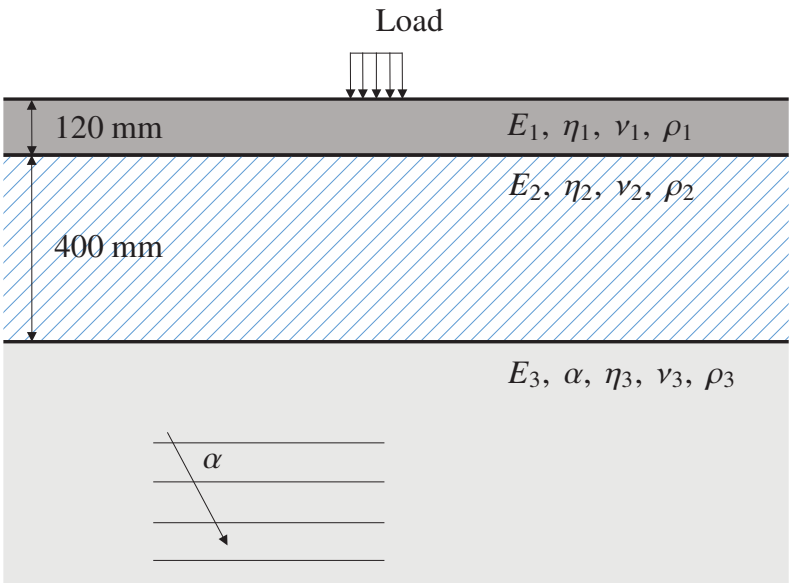

Figure 3.4: Three layered pavement structure.

to increase as a function of depth. An expression suggested by Ullidtz [1998] was employed in this connection

$$E_3(z) = E_3^0 \left(\frac{z}{z_0} \right)^{\alpha} \tag{3.2}$$

where E_3^0 is Young's modulus at the top of the subgrade, z_0 is a reference depth, and $\alpha \geq 0$ is a unitless exponent governing the rate of modulus increase. For the pavement considered in this paper the reference depth is $z_0 = 520\,\text{mm}$ (see Figure 3.4).

The system is assumed stress free until the surface of the top layer is exposed to an FWD stress history $\boldsymbol{\sigma}(t)$ uniformly distributed over a circle with radius 150 mm. To solve for the resulting dynamic response, the formulation presented in Chapter 2 is employed. An FWD drop test is a relatively short-lasting event, in the order of 30 ms in duration. The domain size can thus be chosen such that fixed boundaries will not influence the displacement field within the area of interest during the simulation time. Hence, absorbing boundaries are not applied for this purpose. The FWD is a stationary loading condition for which reason the load speed is zero and the formulation becomes equivalent to the general equation of motion, here given in the weak FE form

$$\int_S \tilde{\mathbf{u}}^T \boldsymbol{\sigma} \mathbf{n} dS - \int_V \left[\tilde{\boldsymbol{\varepsilon}}^T \boldsymbol{\sigma} + \rho \tilde{\mathbf{u}}^T \ddot{\mathbf{u}} \right] dV = 0 \tag{3.3}$$

Since the force is circular and uniformly distributed, the problem is treated as axisymmetric with radial coordinate r, axis of revolution z and circumferential coordinate θ. When loads, boundaries, geometry and elastic properties are axisymmetric, the displacement field becomes a function of the radial displacement u_r and the axial displacement u_z only, i.e. $\mathbf{u} = [u_r, u_z]^T$. The strain-displacement relationships are

$$\varepsilon_r = \frac{\partial u_r}{\partial r} \quad \varepsilon_\theta = \frac{u}{r} \quad \varepsilon_z = \frac{\partial u_z}{\partial z} \quad \gamma_{rz} = \frac{\partial u_r}{\partial z} + \frac{\partial u_z}{\partial r} \tag{3.4}$$

In array format the strain and corresponding stress is written as

$$\boldsymbol{\sigma} = [\sigma_{rr}, \sigma_{\theta\theta}, \sigma_{zz}, \sigma_{rz}]^T \tag{3.5}$$

$$\varepsilon = \boldsymbol{\partial} \mathbf{u} = [\varepsilon_{rr}, \varepsilon_{\theta\theta}, \varepsilon_{zz}, \gamma_{rz}]^T \tag{3.6}$$

The strain-displacement operator is expressed by

$$\boldsymbol{\partial} = \begin{bmatrix} \partial/\partial r & 0 \\ 1/r & 0 \\ 0 & \partial/\partial z \\ \partial/\partial z & \partial/\partial r \end{bmatrix} \tag{3.7}$$

Since no variation occurs in the circumferential direction, the volume dV of an element can be expressed as

$$dV = 2\pi r dA \tag{3.8}$$

where dA is the cross-sectional area of an element. Similarly, the element of surface dS can be expressed as

$$dS = 2\pi r ds \tag{3.9}$$

where ds denotes an element length. Insertion of (3.8) and (3.9) into (3.3) leads to the equation of motion on matrix format

$$\mathbf{M}\ddot{\mathbf{u}} + \mathbf{Z}\dot{\mathbf{u}} + \mathbf{K}\mathbf{u} = \mathbf{F}(t) \tag{3.10}$$

in which the matrices are defined as

$$\mathbf{M} = 2\pi \int_A \rho \tilde{\mathbf{N}}^T \mathbf{N}\, r\, dr\, dz \tag{3.11}$$

$$\mathbf{Z} = \eta\, 2\pi \int_A \tilde{\mathbf{B}}^T \mathbf{C}\mathbf{B}\, r\, dr\, dz \tag{3.12}$$

$$\mathbf{K} = 2\pi \int_A \tilde{\mathbf{B}}^T \mathbf{C}\mathbf{B}\, r\, dr\, dz \tag{3.13}$$

where $\mathbf{B} = \partial\mathbf{N}$ denotes the strain displacement matrix and the constitutive matrix $\mathbf{C}$ for layer i is given by

$$\mathbf{C} = \frac{E_i}{(1+\nu_i)(1-2\nu_i)} \begin{bmatrix} 1-\nu_i & \nu_i & \nu_i & 0 \\ \nu_i & 1-\nu_i & \nu_i & 0 \\ \nu_i & \nu_i & 1-\nu_i & 0 \\ 0 & 0 & 0 & (1-2\nu_i)/2 \end{bmatrix} \tag{3.14}$$

Finally, the load vector in Equation (3.10) is given by

$$\mathbf{F}(t) = 2\pi \int_A \boldsymbol{\sigma}(t)\mathbf{n} r ds \tag{3.15}$$

The method of mesh generation presented in Section 2.4.1 is applied. The mesh parameters were selected such that computed deflections are accurate to within $\pm 1\,\mu$m which is equivalent to the level of deflection accuracy measured by a typical FWD device. Accordingly, the final mesh generation values are: $\bar{d}_0 = 9500$ mm, $\Delta x_{min} = 19$ mm, $\Delta x_{max} = 625$ mm, and $G_R = 0.06$.

3.3 Backcalculation

Traditional backcalculation procedures, which are still widely employed by engineers, ignore inertia effects, disregard time-dependent layer properties, and focus on matching peak deflections only. However, these effects are necessary to include in order to capture the dynamic behavior of a pavement subjected to an impact load. Deflection basins generated by static and dynamic models can deviate significantly dependent on the properties of the pavement layers. This is illustrated by two examples in Figure 3.5. Figure 3.5a shows three deflection basins generated using dynamic analysis (solid). The deflection basins are generated using peak values of the deflection time-histories. Base modulus is $E_2 = 500$ MPa and subgrade modulus is $E_3 = 30$ MPa for all basins while AC modulus differs from each basin with the values 1000 MPa, 4000 MPa and 8000 MPa, as indicated in the legend. The same properties are used to

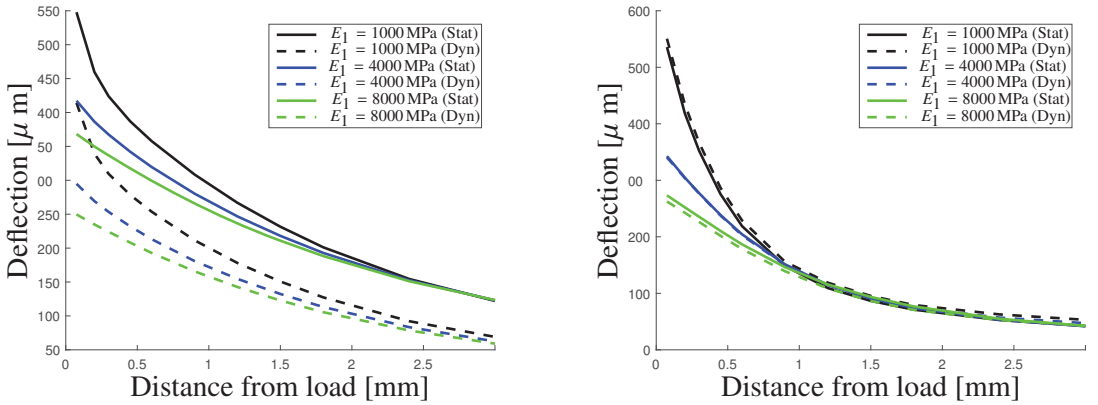

(a) $E_2 = 500$ MPa, $E_3^0 = 30$ MPa and $\alpha = 0$ **(b)** $E_2 = 100$ MPa, $E_3^0 = 80$ MPa and $\alpha = 0$

Figure 3.5: Deflection basin generated by means of static and dynamic analysis. Base and subgrade layer moduli are given in each figure label and AC moduli are given in each figure legend. The subgrade modulus is constant with depth, i.e. $\alpha = 0$ and damping is zero in all layers; $\eta_1 = \eta_2 = \eta_3 = 0$.

generate three deflection basins with static analysis (dashed). In static analysis, a deflection basin is obtained directly as the deformation of the surface under static load application. To make the comparison between dynamic and static analysis as simple as possible, layer damping and rate of modulus increase in the subgrade are all set equal to zero; $\eta_1 = \eta_2 = \eta_3 = 0$ and $\alpha = 0$. The deflection basins become significantly different when static or dynamic analysis is employed. The biggest differences are found when the subgrade is soft and the stiffness ratio between layers is large. In Figure 3.5b the subgrade stiffness is increased to $E_3 = 80$ MPa and base modulus is decreased to $E_2 = 100$ MPa, i.e. small stiffness ratio between base and subgrade moduli. In this simple case where damping is neglected, the basins obtained with static and dynamic analysis are close.

For further analysis of the FWD experiments presented in section 3.1.1, backcalculation is employed to best estimate the constitutive parameters of the pavement layers in Figure 3.4 under the different loading conditions in Table 3.1. For this purpose the measured load histories are used as an input to the numerical formulation for generating model deflections. The applied load is discretized with a constant interval of 0.5 ms into 60-120 time steps depending on the load pulse duration. The level of mismatch between the modelled and measured deflections is subsequently minimized by adjusting the unknown parameters. As shown in Figure 3.4 there are a total of 13 constitutive parameters that govern the model response. As is commonly accepted (see e.g. Huang [2004]), $\nu_1 - \nu_3$ and $\rho_1 - \rho_3$, are prefixed before performing the backcalculation; their chosen values are included in Table 3.2. The seven remaining parameters: E_1, E_2, E_3^0, $\eta_1 - \eta_3$ and α are kept adjustable for the backcalculation algorithm. As means of

Layer	ν [−]	ρ kg/m^3	E [MPa]	η [s]	α
1	0.35	2400	[1000 – 7000]	$[5 \cdot 10^{-5} - 5 \cdot 10^{-3}]$	-
2	0.35	2000	[150 – 750]	$[5 \cdot 10^{-5} - 5 \cdot 10^{-3}]$	-
3	0.35	1800	[25 – 180]	$[5 \cdot 10^{-5} - 5 \cdot 10^{-3}]$	[0 – 3.0]

Table 3.2: Material properties of the tested pavement. ρ and ν are estimated and kept constant during backcalculation. E, η and α are represented by intervals from which seed values are chosen for backcalculation.

confining the solution search space, this latter set of sought parameters is bound to be within the ranges defined in Table 3.2.

3.3.1 Minimization approach

An objective function, ψ_{ab}, is defined to express the difference between modelled and measured deflections as follows

$$\psi_{ab} = \sqrt{\frac{1}{b-a+1}\frac{1}{M}\sum_{k=a}^{b}\sum_{j=1}^{M}(D_k(t_j) - d_k(t_j))^2} \tag{3.16}$$

where $D_k(t_j)$ is the deflection measured by the k^{th} geophone at discrete times $t_j = t_1, t_2, ..., t_M$ and $d_k(t_j)$ is the corresponding deflection produced by the numerical model. The geophones included in the objective function are $k \in [a; b]$ where a and b are geophone numbers; $a = 1, 2, ..., 8$ and $b = 1, 2, ..., 8$ with $b \geq a$. As can be seen, ψ_{ab} represents the discrepancy between model and measurement across the entire simulated time for a group of sensors $a, a + 1, ..., b$ out of the entire available set. The value ψ_{ab} corresponds to the mean discrepancy in μm across the entire simulated time. The overall goal of the backcalculation process is to minimize ψ_{18} within a total analysis duration t_M. Deflection recordings are known to be less reliable as time progresses (due to integration of geophone data), producing unrealistic deflection tails (e.g., Uzan [1994]). As means of ensuring convergence into physically realistic results t_M is therefore chosen to include the first part of the recorded deflections - about 60%. This analysis period covers the deflection rise-time, the peak, and a small portion of the decrease.

Another effort for ensuring convergence into meaningful results involved performing the minimization in stages. Initially, parameter seed values are randomly chosen within the bounds given in Table 3.2. Then ψ_{48} is minimized with respect to E_3^0, α and η_3 (Stage I), ψ_{23} is minimized with respect to E_2 and η_2 (Stage *II*), and finally ψ_1 is minimized with respect to E_1 and η_1 (Stage *III*). This bottom-up approach is based on an engineering intuition that associates more distant geophone readings with deeper layer

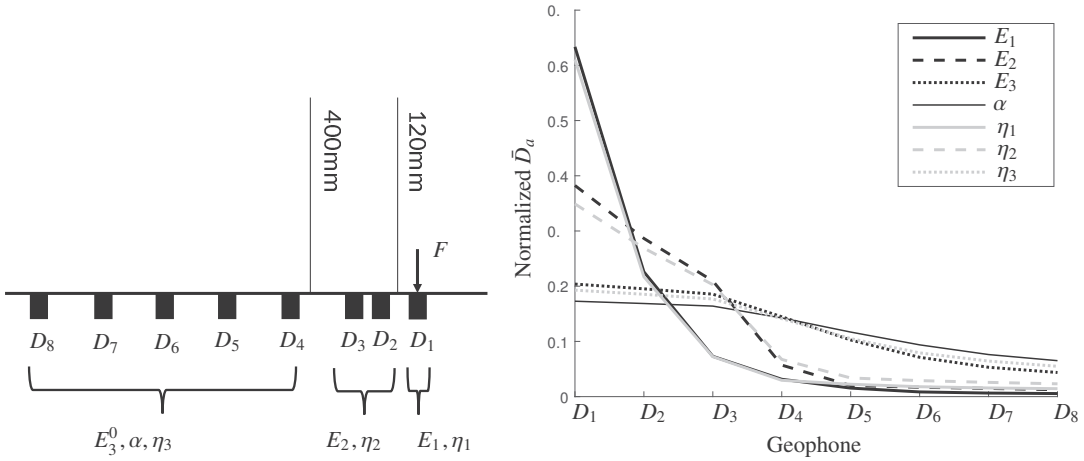

(a) Illustration of primary influence on geophones.

(b) One-at-a-time sensitivity analyis.

Figure 3.6: Pavement layering is superposed over the geophone array configuration, supported by a one-at-a-time sensitivity analyis: Relative mean value difference between the response of each geophone calculated with reference parameter values and perturbed parameter values.

properties. The rational for specific choices in the above stages is illustrated in Figure 3.6a in which the pavement layering is superposed over the geophone array configuration. Accordingly, $d_4 - d_8$ are deemed more sensitive to the subgrade parameters, $d_2 - d_3$ are deemed more sensitive to the base parameters and d_1 most closely associated with the AC parameters. This specific choice is further supported by a one-at-a-time sensitivity analysis conducted on the seven parameters. Each parameter is given an initial value and a reference deflection time history d_a is calculated for each of the geophone positions $d_1 - d_8$. Then one parameter at a time is perturbed with $+10\%$ and the deflection histories are calculated once again, $d_a^{10\%}$. The mean value of the relative difference in deflection histories is calculated for each of the geophone positions

$$\bar{D}_a = \frac{1}{M} \sum_{j=1}^{M} \frac{\left| d_a(t_j) - d_a^{10\%}(t_j) \right|}{d_a(t_j)} \tag{3.17}$$

where a refers to the geophone position number and the superscript $^{10\%}$ indicates perturbed deflections. The values $\bar{D}_a$ are presented in Figure 3.6b in a normalized form for each of the seven parameters. It is here seen that AC layer properties have highest influence on deflections d_1, base parameters have the highest influence on deflections $d_2 - d_3$ and deflections $d_4 - d_8$ are mostly governed by subgrade parameters.

A gradient based method is used for the separate stages with gradients calculated using a backward finite difference. In each of the three stages minimization is restarted several times with new seed values to broaden the search space for a solution. The optimal

(minimal) objective functions in stages I, II and III are denoted ψ_{48}^{min}, ψ_{23}^{min} and ψ_{1}^{min}. These entities are employed in the Min-Max sense (Osyczka [1978]) to perform an overall minimization for ψ_{18} with respect to all adjustable parameters simultaneously (Stage *IV*)

$$\psi_{18} = \frac{1}{3}\left(\frac{\psi_{48}}{\psi_{48}^{min}} + \frac{\psi_{23}}{\psi_{23}^{min}} + \frac{\psi_{1}}{\psi_{1}^{min}}\right)\left(\psi_{48}^{min} + \psi_{23}^{min} + \psi_{1}^{min}\right) \tag{3.18}$$

in which ψ_{48}, ψ_{23} and ψ_{1} are calculated by Equation (3.16). The last bracket in (3.18) serves as a scaling factor. A general purpose unconstrained derivative-free nonlinear optimization algorithm is employed for this final minimization step. A pseudo code for the entire procedure is presented in Algorithm 3.

Algorithm 3 Backcalculation approach

1: Random initial guess of $X_0 = [E_1, E_2, E_3^0, \alpha, \eta_1, \eta_2, \eta_3]$
2: **Stage I:**
3: $\underset{x_I=[E_3^0,\alpha,\eta_3]}{\text{minimize}}$ $\psi_{48}(x_I)$ subject to $LB \leq x_I \leq UB$
4: Continue minimization until $\Delta\psi_{48}(x_I) \leq 10^{-6}$
5: **Stage II:**
6: Given result of stage I:
7: $\underset{x_{II}=[E_2,\eta_2]}{\text{minimize}}$ $\psi_{23}(x_{II})$ subject to $LB \leq x_{II} \leq UB$
8: Continue minimization until $\Delta\psi_{23}(x_{II}) \leq 10^{-6}$
9: **Stage III:**
10: Given result of stage I and II:
11: $\underset{x_{III}=[E_1,\eta_1]}{\text{minimize}}$ $\psi_{1}(x_{III})$ subject to $LB \leq x_{III} \leq UB$
12: Continue minimization until $\Delta\psi_{1}(x_{III}) \leq 10^{-6}$
13: Calculate weights for overall optimization
14: **Stage IV:**
15: Given result of stage I, II and III as initial guess:
16: $\underset{x_{IV}=[E_1,\eta_1,E_2,\eta_2,E_3^0,\eta_3,\alpha]}{\text{minimize}}$ $\psi_{18}(x_{IV})$ using Matlab's fminsearch function
17: Continue minimization until $\Delta\psi_{18}(x_{IV}) \leq 10^{-6}$

3.4 Backcalculation results

Included and discussed in this section are backcalculation results. First presented is the fitting obtained between modelled and measured deflection histories for Test 6 and for Test 8. Both drops are similar in terms of peak force but different with respect to pulse duration (see Table 3.1). Geophone measurements and calculated deflections are superposed in Figures 3.7 and 3.8. The dashed vertical line indicate the analysis

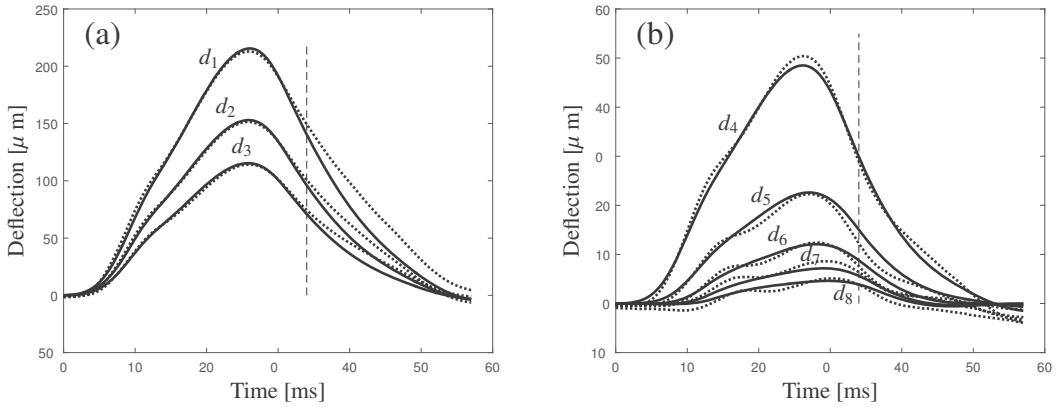

Figure 3.7: Measured (dotted) and modelled (solid) deflection histories for Test 6 (see Table 3.1).

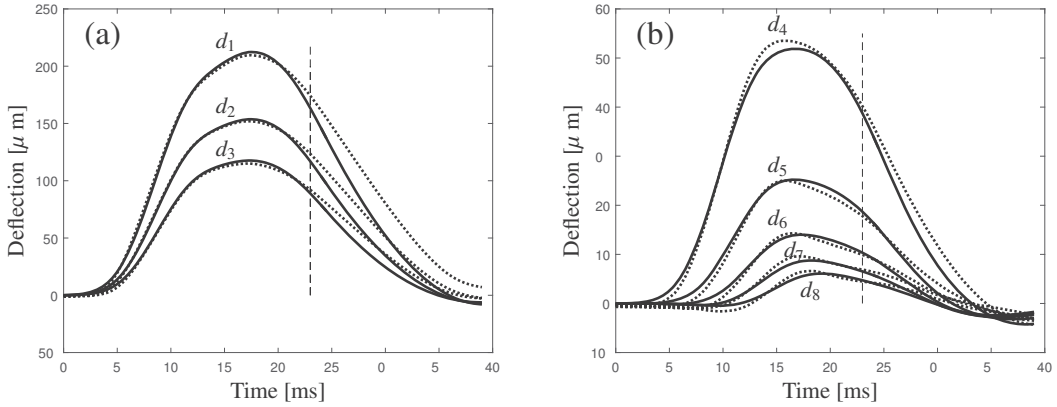

Figure 3.8: Measured (dotted) and modelled (solid) deflection histories for Test 8 (see Table 3.1).

duration in each case (i.e., t_M). As can be graphically seen in both figures, the FE model is able to capture and reproduce both the magnitude and the overall shape of the deflections. However, discrepancy between measured and modeled deflections is seen to increase for times exceeding the fitting window, particularly for $d_1 - d_3$. This might be due to a lack of model complexicy or due to increasing measurement error with time as mentioned earlier; or it might be a combination of both. Essentially similar charts are obtained for the other tests.

A summary of the backcalculation results for the eight FWD drops is presented in Table 3.3. For the AC layer, E_1 was found in the range 3065-4561 MPa and η_1 was found in the range of 2.1-4.1 ms. For the base layer, E_2 was found in the range 246-307 MPa and η_2 in the range of 0.6-1.1 ms. Finally, for the subgrade, E_3^0 was found in the range 99-153 MPa, η_3 in the range of 0.9-2.0 ms, and α in the range of 1.0-1.4. The latter corresponds well to the vane test results which indicated increasing stiffness profile for

	AC properties		Base properties		Subgrade properties			
Test	E_1	η_1	E_2	η_2	E_3^0	α	η_3	ψ_{18}^{min}
1	4211	2.5	247	0.6	99	1.2	2.0	3.6
2	4250	2.2	238	1.1	126	1.2	1.1	2.2
3	3786	2.8	272	0.9	151	1.1	0.9	1.0
4	3065	3.3	307	0.8	129	1.4	1.3	0.8
5	3492	4.1	285	0.8	143	1.1	1.9	1.0
6	3953	4.5	262	0.7	150	1.0	2.0	1.4
7	4085	3.1	246	1.1	153	1.0	1.5	1.5
8	4561	2.1	254	0.9	138	1.2	1.0	1.5
Mean	3925	3.1	264	0.9	136	1.2	1.5	1.6
CV [%]	12.0	29.0	8.7	22.2	13.2	8.3	33.3	56.3

Table 3.3: Layer properties obtained from FWD Backcalculation (Moduli given in [MPa] and damping parameters in [ms]).

the subgrade. Across the different analysed cases, the coefficient of variation for the moduli values was relatively small, about 10%, while the coefficient of variation for the damping parameters was nearly three times larger. Overall, the backcalculated values are well within the bounds defined in Table 3.2 and are therefore reasonable from an engineering standpoint.

For comparison, the same backcalculation procedure was used to match the entire deflection histories. Measured and calculated deflections are superposed in Figure 3.9 for Test 8. Compared to Figure 3.8, a better fitting of the deflection history tail is obtained. This is obvious since the tail was disregarded in Figure 3.8. On the other hand, a larger discrepancy occurs in the first part where deflections increase to peak. Moreover, the shape of the deflections, which was captured very well particularly in Figure 3.8b, is not captured as well in Figure 3.9b.

Presented in Table 3.4 is a summary of the backcalculation results for the eight FWD drops for which the entire deflection-time histories are fitted. The mean value of layer moduli, α and η_3 are similar to the mean values obtained in Table 3.3 while the mean values of η_1 and η_2 are about two times larger. The coefficient of variance is however significantly larger for all the seven backcalculated parameters; about 30% for moduli values and $70-120\%$ for damping parameters. For the AC layer, E_1 was found in the range 1430-5583 MPa and η_1 was found in the range of 0.0-18.7 ms. For the base layer, E_2 was found in the range 161-371 MPa and η_2 in the range of 0.0-5.6 ms. Finally, for the subgrade, E_3^0 was found in the range 50-157 MPa, η_3 in the range of 0.0-2.5 ms, and

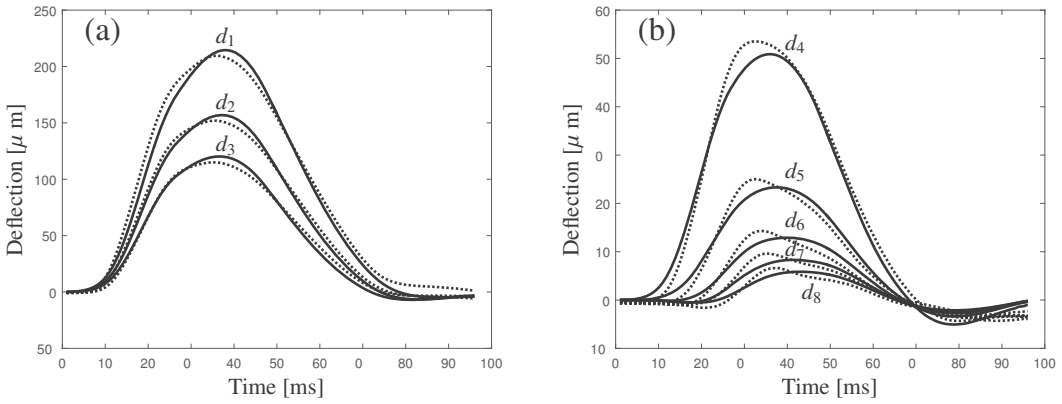

Figure 3.9: Measured (dotted) and modelled (solid) deflection histories for Test 8 (see Table 3.1). As opposed to Figure 3.8, the entire deflection time-history is matched.

α in the range of 1.0-2.3. AC and Base damping, η_1 and η_2, exceed the limits defined in Table 3.2 in some of the analysed cases. The calculations obtained by using the entire deflection histories are therefore not reasonable.

As means of investigating the influence of different FWD load-time histories on back-calculated outcomes, the backcalculation results obtained using part of the deflection histories (Table 3.3) are used. Figure 3.10 presents some of the results from Table 3.3 combined with data from Table 3.1. Figure 3.10a cross-plots moduli values and pulse duration across all peak loads, Figure 3.10b depicts moduli values versus peak loads across all pulse durations, and Figure 3.10c cross-plots damping values and pulse duration. As can be graphically noticed in the charts, all backcalculated parameters are influenced by the FWD load-time history. Specifically, the AC modulus (E_1) displays slight decrease with increasing pulse duration and slight increase with increasing peak load levels. Similar sensitivity, but with opposite trends, is exhibited by the base and top of subgrade moduli (E_2 and E_3^0). As for layer damping, it appears that the AC is most sensitive, showing an increase in value with increase in pulse duration. Subgrade damping is slightly increasing with increase in pulse duration while base damping seem to be uncorrelated with FWD pulse duration.

The results of the investigation indicate that different FWD load-time histories produce different backcalculation parameters for the tested pavement. The trends appearing in Figure 3.10 are not random in nature. In other words, the optimized values of the model parameters has to be readjusted to best match the measured deflections depending on the pulse attributes. This finding suggests that modelling complexity is too simplified. The rational here is that if a more intricate pavement model is employed then inferred properties based on any deflection test should remain identical when back-calculated. Possible enhancements in this connection can include: better viscoelastic representation of the AC layer, allowance for nonlinear stress-dependent behaviour of

	AC properties		Base properties		Subgrade properties			
Test	E_1	η_1	E_2	η_2	E_3^0	α	η_3	ψ_{18}^{min}
1	5583	0.0	161	5.6	99	1.6	0.3	12.2
2	1430	18.7	371	0.0	50	2.3	2.0	4.2
3	3172	8.2	268	0.0	153	1.1	1.7	1.6
4	2640	6.2	302	2.2	91	2.0	0.2	1.9
5	3324	4.7	269	3.4	116	1.5	0.0	2.6
6	3399	10.7	258	0.0	143	1.1	2.5	2.3
7	2893	2.7	299	3.0	127	1.2	1.6	4.4
8	4038	7.1	233	0.0	157	1.0	1.7	2.7
Mean	3310	7.3	270	1.8	117	1.5	1.25	4.0
CV [%]	35.9	77.8	22.2	119.6	30.9	32.0	75.4	87.7

Table 3.4: Layer properties obtained from FWD Backcalculation by fitting the entire deflection-time histories (Moduli given in [MPa] and damping parameters in [ms]).

the base and subgrade, and incorporation of anisotropic response. The downside here is that more unknown constitutive parameters will need to be evaluated. However, the observed parameter sensitivity to FWD pulse attributes essentially means that new constitutive information is exposed under the different loading situations. Consequently, opportunity arises for increasing the modelling complexity as suggested above because a wider calibration set becomes available to reliably infer the new/additional constitutive parameters. To achieve this, the testing should first include diverse load-time histories, and the analysis should require simultaneous matching of all deflection histories.

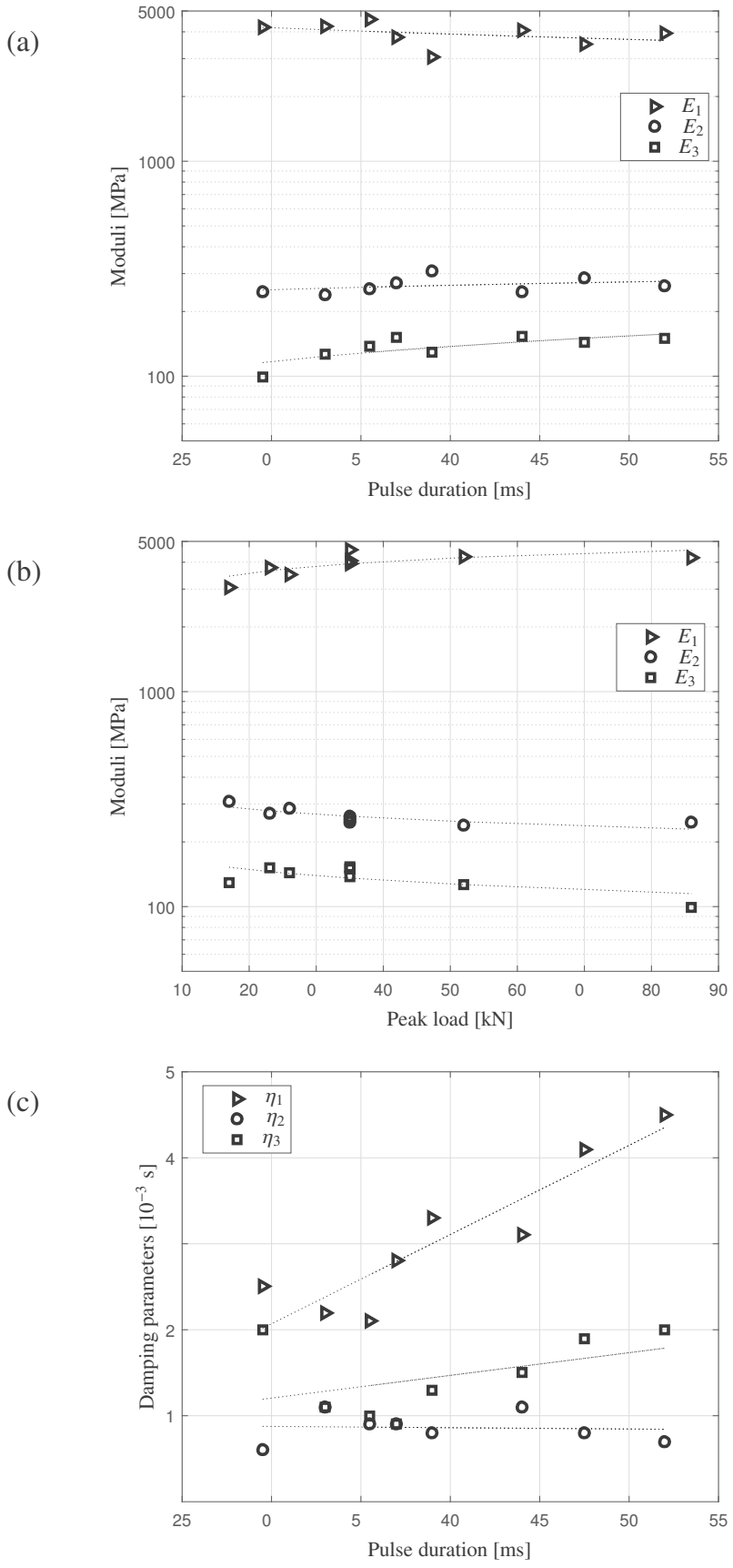

Figure 3.10: Backcalculated parameters: (a) Moduli as function of pulse duration, (b) Moduli as function of peak load and (c) damping parameters as function of pulse duration

Chapter 4

Concluding remarks

For many years the FWD has been a standard device for pavement deflection measurements to estimate the bearing capacity of pavements. However, increasing attention has been given to the Rolling Wheel Deflectometer (RWD) type of device due to its ability to measure deflections continuously while driving at traffic speed. Hence it becomes important to gain more knowledge about a pavement's behavior as it is subjected to transient dynamic loads moving with various speeds. In this thesis, a new Finite Element formulation for transient dynamic analysis has been developed. The model includes absorbing boundary conditions in the form of the efficient Perfectly Matched Layer (PML) to ensure capability of long simulation time without reflections from the boundaries. The formulation is in a moving frame of reference to increase computational efficiency by being able to limit the domain size. Another advantage of a formulation in a moving frame of reference is that the surface deflections are continuously following the vehicle's point of view.

The formulation has been derived for both 2D and 3D. From 2D investigations it was found that the PML performed very well for loads moving with various speed both in the case of a half space and in the case of a viscoelastic layer overlying a half space. A pulse applied to the surface arrives with the speed $c + V$ at a fixed point behind the moving load, where V denotes the speed of the load and c is the wave velocity of the soil. The pulse arrives with the speed $c - V$ at a fixed point in front of the load. The response amplitude decreases with increasing speed. A high modulus ratio between top layer and underlying soil reveals a significant effect in terms of an amplified response

and earlier arrival of the pulse in a fixed point in front of the load. The response obtained at a point behind the load is almost not affected by the modulus ratio. Moreover, the differences in response magnitude and attenuation rate of 2D and 3D waves are illustrated.

The model has been applied for backcalculation of a number of FWD experiments conducted on a three layer pavement with various load-time histories. The load-time histories differ from each other in terms of load pulse duration and load magnitude. The model is able to capture both magnitude and overall shape of the measured deflections in all the test cases. The backcalculated parameters include Young's modulus and damping of each layer and an exponent for increasing stiffness with depth of the subgrade. The coefficient of variance of the backcalculated parameters across all tests were around 10% for the moduli and 30% for the damping parameters. The backcalculated parameters were found sensitive to the load pulse duration. This suggests that the model can be improved in terms of complexity in order to obtain similar optimized values in all the test cases. This finding also suggests, that performing FWD experiments with various load-time histories is a good way of calibrating a model by performing backcalculation of various FWD experiments simultaneously.

4.1 Future work

Future work should be directed towards:

- Improving the viscoelastic model and allow for stress-dependent behavior of base and subgrade.
- Validation of the model in terms of backcalculation of pavement layer properties using data measured by an RWD.
- Uncertainty quantification and sensitivity analysis of the model.

Appendix A

Finite element matrices with PML

The strain-displacement matrix in three-dimensional PML formulation is given by

$$\mathbf{B} = \begin{bmatrix} N_{I,1} & 0 & 0 \\ 0 & N_{I,2} & 0 \\ 0 & 0 & N_{I,3} \\ N_{I,2} & N_{I,1} & 0 \\ N_{I,3} & 0 & N_{I,1} \\ 0 & N_{I,3} & N_{I,2} \\ N_{I,2} & -N_{I,1} & 0 \\ N_{I,3} & 0 & -N_{I,1} \\ 0 & N_{I,3} & -N_{I,2} \end{bmatrix} \tag{A.1}$$

Based on Equation (2.39) The three-dimensional constitutive matrix with PML reads

$$\tilde{\mathbf{C}} = \begin{bmatrix} D_{11} & D_{12} & D_{13} & & & & & & \\ D_{21} & D_{22} & D_{23} & & & & & & \\ D_{31} & D_{32} & D_{33} & & & & & & \\ & & & D_{44} & & D_{47} & & & \\ & & & & D_{55} & & D_{58} & & \\ & & & & & D_{66} & & D_{69} & \\ & & & D_{74} & & D_{77} & & & \\ & & & & D_{85} & & D_{88} & & \\ & & & & & D_{96} & & D_{99} & \end{bmatrix} \tag{A.2}$$

The empty slots inside $\tilde{\mathbf{C}}$ are zero and the non-zero ones are

$$
\begin{aligned}
\tilde{D}_{11} &= (2\mu+\lambda)\frac{s_2 s_3}{s_1}, \quad \tilde{D}_{12}=\tilde{D}_{21}=\lambda s_3, \quad \tilde{D}_{13}=\tilde{D}_{31}=\lambda s_2, \\
\tilde{D}_{22} &= (2\mu+\lambda)\frac{s_1 s_3}{s_2}, \quad \tilde{D}_{23}=\tilde{D}_{32}=\lambda s_1, \quad \tilde{D}_{33}=(2\mu+\lambda)\frac{s_1 s_2}{s_3}, \\
\tilde{D}_{44} &= \mu\left(\frac{s_3}{2}+\frac{s_2 s_3}{4s_1}+\frac{s_1 s_3}{4s_2}\right), \quad \tilde{D}_{47}=\tilde{D}_{74}=\frac{\mu}{4}\left(\frac{s_2 s_3}{s_1}-\frac{s_1 s_3}{s_2}\right) \\
\tilde{D}_{55} &= \mu\left(\frac{s_2}{2}+\frac{s_2 s_3}{4s_1}+\frac{s_1 s_2}{4s_3}\right), \quad \tilde{D}_{58}=\tilde{D}_{85}=\frac{\mu}{4}\left(\frac{s_2 s_3}{s_1}-\frac{s_1 s_2}{s_3}\right) \\
\tilde{D}_{66} &= \mu\left(\frac{s_1}{2}+\frac{s_1 s_3}{4s_2}+\frac{s_1 s_2}{4s_3}\right), \quad \tilde{D}_{69}=\tilde{D}_{96}=\frac{\mu}{4}\left(\frac{s_1 s_3}{s_2}-\frac{s_1 s_2}{s_3}\right) \\
\tilde{D}_{77} &= \mu\left(-\frac{s_3}{2}+\frac{s_2 s_3}{4s_1}+\frac{s_1 s_3}{4s_2}\right), \quad \tilde{D}_{88}=\mu\left(-\frac{s_2}{2}+\frac{s_2 s_3}{4s_1}+\frac{s_1 s_2}{4s_3}\right) \\
\tilde{D}_{99} &= \mu\left(-\frac{s_1}{2}+\frac{s_1 s_3}{4s_2}+\frac{s_1 s_2}{4s_3}\right)
\end{aligned}
\tag{A.3}
$$

The constitutive matrix is divided into a non-stretched and six stretched parts. The non-stretched part is found by letting $s_1 = s_2 = s_3 = 1$ in A.2. The six stretched parts are given by

$$
C_{12/3} = \begin{bmatrix}
0 & & & & & & & & \\
& 0 & & & & & & & \\
& & 2\mu+\lambda & & & & & & \\
& & & 0 & & & & & \\
& & & & \mu/4 & & & -\mu/4 & \\
& & & & & \mu/4 & & & -\mu/4 \\
& & & & & & 0 & & \\
& & & & -\mu/4 & & & \mu/4 & \\
& & & & & -\mu/4 & & & \mu/4
\end{bmatrix}
\tag{A.4}
$$

$$
C_{23/1} = \begin{bmatrix}
2\mu+\lambda & & & & & & & & \\
& 0 & & & & & & & \\
& & 0 & & & & & & \\
& & & \mu/4 & & & \mu/4 & & \\
& & & & \mu/4 & & & \mu/4 & \\
& & & & & 0 & & & \\
& & & \mu/4 & & & \mu/4 & & \\
& & & & \mu/4 & & & \mu/4 & \\
& & & & & & & & 0
\end{bmatrix}
\tag{A.5}
$$

$$C_{13/2} = \begin{bmatrix} 0 & & & & & & & & & & & \\ & 2\mu+\lambda & & & & & & & & & & \\ & & 0 & & & & & & & & & \\ & & & \mu/4 & & & & \mu/4 & & & & \\ & & & & 0 & & & & & & & \\ & & & & & \mu/4 & & & & \mu/4 & & \\ & & & \mu/4 & & & & \mu/4 & & & & \\ & & & & & & & & 0 & & & \\ & & & & & & \mu/4 & & & & \mu/4 & \end{bmatrix} \tag{A.6}$$

$$C_1 = \begin{bmatrix} 0 & & & & & & & & & & & \\ & 0 & \lambda & & & & & & & & & \\ & \lambda & 0 & & & & & & & & & \\ & & & 0 & & & & & & & & \\ & & & & 0 & & & & & & & \\ & & & & & \mu/2 & & & & & & \\ & & & & & & 0 & & & & & \\ & & & & & & & 0 & & & & \\ & & & & & & & & -\mu/2 & & & \end{bmatrix} \tag{A.7}$$

$$C_2 = \begin{bmatrix} 0 & & \lambda & & & & & & & & & \\ & 0 & & & & & & & & & & \\ \lambda & & 0 & & & & & & & & & \\ & & & 0 & & & & & & & & \\ & & & & \mu/2 & & & & & & & \\ & & & & & 0 & & & & & & \\ & & & & & & 0 & & & & & \\ & & & & & & & -\mu/2 & & & & \\ & & & & & & & & 0 & & & \end{bmatrix} \tag{A.8}$$

$$C_3 = \begin{bmatrix} 0 & \lambda & & & & & & & & & & \\ \lambda & 0 & & & & & & & & & & \\ & & 0 & & & & & & & & & \\ & & & \mu/2 & & & & & & & & \\ & & & & 0 & & & & & & & \\ & & & & & 0 & & & & & & \\ & & & & & & -\mu/2 & & & & & \\ & & & & & & & 0 & & & & \\ & & & & & & & & 0 & & & \end{bmatrix} \tag{A.9}$$

Bibliography

R. Al-Khoury, A. Scarpas, C. Kasbergen, and J. Blaauwendraad. Spectral element technique for efficient parameter identification of layered media. i. forward calculation. *International Journal of Solids and Structures*, 38(9):1605–1623, 2001.

L. Andersen, S. R. K. Nielsen, and S. Krenk. Numerical methods for analysis of structure and ground vibration from moving loads. *Computers & Structures*, 85:43–58, 2007.

ASTM. Astm d4694 - 09, standard test method for deflections with a falling-weight-type impulse load device. Technical report, 2015.

Niki D. Beskou, Stephanos V. Tsinopoulos, and Dimitrios D. Theodorakopoulos. Dynamic elastic analysis of 3-d flexible pavements under moving vehicles: A unified {FEM} treatment. *Soil Dynamics and Earthquake Engineering*, 82:63 – 72, 2016.

D. M. Burmister, L. A. Palmer, E. S. Barber, and T. A. Middlebrooks. THE THEORY OF STRESS AND DISPLACEMENTS IN LAYERED SYSTEMS AND APPLICATIONS TO THE DESIGN OF AIRPORT RUNWAYS. *Highway Research Board Proceedings*, 23, 1944.

Karim Chatti, Yigong Ji, and Ronald Harichandran. Dynamic time domain backcalculation of layer moduli, damping, and thicknesses in flexible pavements. *Transportation Research Record: Journal of the Transportation Research Board*, (1869): 106–116, 2004.

Y.-H. Chen, Y.-H. Huang, and C.-T. Shih. RESPONSE OF AN INFINITE TIMOSHENKO BEAM ON A VISCOELASTIC FOUNDATION TO A HARMONIC MOVING LOAD. *Journal of Sound and Vibration*, 241(5):809–824, April 2001.

W C Chew and Q H Liu. Perfectly matched layers for elastodynamics: A new absorbing boundary condition. *Journal of Computational Acoustics*, 4:341–359, 1996.

W C Chew and W H Weedon. A 3D perfectly matched medium from modified Maxwell's equations with stretched coordinates. *Microwave and Optical Technology Letters*, 7:599–604, 1994.

R.D. Cook, D.S. Malkus, and M.E. Plesha. *Concepts and applications of finite element analysis*. Wiley, 2002.

H. A. Dieterman and V. Metrikine. Steady-state displacements of a beam on an elastic half-space due to a uniformly moving constant load. *European Journal of Mechanics - Series A/Solids*, 16:295–306, 1997.

Hu Ding, Kang-Li Shi, Li-Qun Chen, and Shao-Pu Yang. Dynamic response of an infinite Timoshenko beam on a nonlinear viscoelastic foundation to a moving load. *Nonlinear Dynamics*, 73(1-2):285–298, July 2013.

Gary E. Elkins, Travis M. Thompson, Jonathan L. Groeger, Beth Visintine, and Gonzalo R. Rada. Reformulated Pavement Remaining Service Life Framework. Technical report, 2013.

M.A. Elseifi, A.M. Abdel-Khalek, K. Gaspard, Z. Zhang, and S. Ismail. Evaluation of continuous deflection testing using the rolling wheel deflectometer in louisiana. *Journal of Transportation Engineering*, 138(4):414–422, 2012.

S. FranÇois, M. Schevenels, P. Galvín, G. Lombaert, and G. Degrande. A 2.5d coupled fe-be methodology for the dynamic interaction between longitudinally invariant structures and a layered halfspace. *Computer Methods in Applied Mechanics and Engineering*, 199(23-24):1536–1548, 2010.

P. Galvín, S. FranÇois, M. Schevenels, E. Bongini, G. Degrande, and G. Lombaert. A 2.5d coupled fe-be model for the prediction of railway induced vibrations. *Soil Dynamics and Earthquake Engineering*, 30(12):1500–1512, 2010.

Daba S. Gedafa, Mustaque Hossain, Richard Miller, and Douglas A. Steele. Surface Deflections of Perpetual Pavement Sections. In *Pavement Performance: Current Trends, Advances, and Challenges*, pages 1–13. ASTM International, November 2012.

Isaac Harari and Uri Albocher. Studies of FE/PML for exterior problems of time-harmonic elastic waves. *Computer Methods in Applied Mechanics and Engineering*, 195:3854–3879, 2006.

M.-H. Huang and David P. Thambiratnam. Dynamic response of plates on elastic foundation to moving loads. *Journal of Engineering Mechanics*, 128(9):1016–1022, 2002.

Y. H. Huang. *Pavement Analysis and Design*. Pearson Prentice Hall, 2004.

H. H. Hung and Y. B. Yang. Elastic waves in visco-elastic half-space generated by various vehicle loads. *Soil Dynamics and Earthquake Engineering*, 21:1–17, 2001.

Dirk Jansen. Tsd evaluation in germany. In *Proceedings of the Internation Symposium Non-Destructive Testing in Civil Engineering*, pages 700–708. Berlin, Germany, 2015.

S Krenk, L Kellezi, S R K Nielsen, and PH Kirkegaard. Finite element and transmitting boundary conditions for moving loads. In *Proceedings of the 4th European Conference on Structural Dynamics, Eurodyn'99*, pages 447–452. Balkema, The Netherlands, 1999.

Chen-Ming Kuo and Ting-Yi Tsai. Significance of subgrade damping on structural evaluation of pavements. *Road Materials and Pavement Design*, 15(2):455–464, 2014.

Hakan Lane, Per Kettil, and Nils-Erik Wiberg. Moving finite elements and dynamic vehicle interaction. *European Journal of Mechanics - A/Solids*, 27(4):515–531, 2008.

J. Lysmer and R. L. Kuhlemeyer. Finite dynamic model for infinite media. *Journal of the Engineering Mechanics Division, American Society of Civil Engineers*, 95: 859–877, 1969.

Michael S. Mamlouk and Trevor G. Davies. Elasto-dynamic analysis of pavement deflections. *Journal of transportation engineering*, 110(6):536–550, 1984.

Rene Matzen. An efficient finite element time-domain formulation for the elastic second-order wave equation: A non-split complex frequency shifted convolutional PML. *International Journal for Numerical Methods in Engineering*, 88:951–973, 2011.

A. V. Metrikine and H. A. Dieterman. Lateral vibrations of an axially compressed beam on an elastic half-space due to a moving lateral load. *European Journal of Mechanics - A/Solids*, 18:147–158, 1999.

Wayne B. MULLER. A comparison of TSD, FWD and GPR field measurements. In *Proceedings of the Internation Symposium Non-Destructive Testing in Civil Engineering*, pages 713–722. Berlin, Germany, 2015.

Soheil Nazarian, Kenneth H. II Stokoe, and Robert C. Briggs. Nondestructively delineating changes in modulus profiles of secondary roads. *Transportation Research Record*, (1136):96–107, 1987.

N. M. Newmark. A method of computation for structural dynamics. *Journal of the Engineering Mechanics Division, ASCE*, 85:67–94, 1959.

A Osyczka. Approach to multicriterion optimization problems for engineering design. *Computer Methods in Applied Mechanics and Engineering*, 15(3):309–333, 1978.

I. Singer and E. Turkel. A perfectly matched layer for the helmholtz equation in a semi-infinite strip. *Journal of Computational Physics*, 201(2):439–465, 2004.

Per Ullidtz. *Modelling Flexible Pavement Response and Performance*. Polyteknisk Forlag, 1998.

J Uzan. Dynamic linear back-calculation of pavement material parameters. *Journal of Transportation Engineering-asce*, 120(1):109–126, 1994.

A.F.H.M. Visser and D.P. Koesrindartono. Towards a mechanistic analysis of benkelman beam deflection measurements. *Heron*, 45(3):177–195, 2000.

Z. Xie, D. Komatitsch, R. Martin, and R. Matzen. Improved forward wave propagation and adjoint-based sensitivity kernel calculations using a numerically stable finite-element PML. *Geophysical Journal International*, 198(3):1714–1747, July 2014.

Y. B. Yang, H. H. Hung, and D. W. Chang. Train-induced wave propagation in layered soils using finite/infinite element simulation. *Soil Dynamics and Earthquake Engineering*, 23(4):263–278, 6/1 2003.

Pyeong Yoo and Imad Al-Qadi. Effect of transient dynamic loading on flexible pavements. *Transportation Research Record: Journal of the Transportation Research Board*, 1990:129–140, 2007.

Sameh Zaghloul and Thomas White. Use of a three-dimensional, dynamic finite element program for analysis of flexible pavement. *Transportation Research Record*, (1388):60–69, 1993.

Wei Zhai and Erxiang Song. Three dimensional FEM of moving coordinates for the analysis of transient vibrations due to moving loads. *Computers and Geotechnics*, 37:164–174, 2010.

Yibing Zheng and Xiaojun Huang. Anisotropic perfectly matched layers for elastic waves in Cartesian and curvilinear coordinates. Technical report, Massachusetts Institute of Technology, Earth Resources Laboratory, 2002.

Appended papers

[P1]

"Perfectly Matched Layer (PML) for transient wave propagation in a moving frame of reference"

Stine S. Madsen and Steen Krenk

Submitted: *Computers and Geotechnics, 2016*

Perfectly Matched Layer (PML) for transient wave propagation in a moving frame of reference

Stine Skov Madsen[1,2], Steen Krenk[2]

[1] *Geotechnics and Geology, Department of Civil Engineering, Technical University of Denmark*

[2] *Solid Mechanics, Department of Mechanical Engineering, Technical University of Denmark*

Abstract

The paper presents the Perfectly Matched Layer (PML) formulated in a moving frame of reference for transient dynamic response of a multi-layer 2D half-space. A displacement based finite element formulation of the convected domain problem is presented together with a PML formulation in which the original convolution integrals are represented via two auxiliary displacement-like state-space variables. A parametric study of the PML parameters is conducted for optimizing the PML. The performance is demonstrated on a single- and a two-layered half-space for various velocities of an impulse Ricker load. Excellent absorbing properties are demonstrated in both half spaces.

Keywords: Convected coordinates, Finite element method, Absorbing boundary, PML, Moving load, Transient wave propagation

1. Introduction

Dynamic analysis of moving loads is of great interest in the fields of road and railway traffic. Determination of the dynamic response of road and airport pavements to moving dynamic loads is very important in pavement design in particular to predict road damage. With the increasing interest of high-speed train lines it

has as well become important to understand the dynamic behavior of a multi-layer half-space subjected to moving loads.

Modeling of elastic wave propagation in a half space requires accurate boundary conditions to allow only outgoing waves. In many cases a numerical solution is developed by applying the finite element method over the computational domain. In the case of a half space, the unbounded region must be truncated to a computational domain of interest, including suitable boundary conditions that are transparent to incident waves, thereby representing the unbounded region.

A technique that has demonstrated very high efficiency as absorbing boundary is the Perfectly Matched Layer (PML). The PML was first suggested by Berenger [1] for the absorption of electromagnetic waves. Shortly after new interpretations to this method was suggested by Chew [2] in terms of introducing the stretch coordinate. Chew and Liu [3] proved that a perfectly matched layer is also applicable for elastic waves using the method of complex coordinate stretching. Later the PML technique was formulated for the elastic wave equation using several modifications by e.g. [4, 5, 6]. However, in these approaches the solution for the displacements is dependent on computation of the strains in each time step. This problem was circumvented in a combined stress-displacement formulation presented by Kucukcoban and Kallivokas [7]. A simpler procedure, depending only on the displacements, using an artificially anisotropic material description of the PML layer, was recently proposed by Matzen [8]. This method proved to be highly efficient, when solving transient vibration problems in a stationary frame of reference.

Potential stability problems of the PML layer formulation for stationary anisotropic problems and wave guides have been discussed in [9, 10, 11]. The problems are related to the basic assumption of the PML layer, that waves propagate into the

layer via impedance matching and are damped while they propagate. An extensive survey of the various PML formulations has been given in [7].

In some studies the dynamic response of a layered half space subjected to a moving load is obtained by manually moving the load from element to element. This approach is used by e.g. Yoo and Al-Qadi [12] in their study of transient dynamic loading of a pavement using a 3D finite element model and Wang et al. [13] analyzing the pavement response of an instrumented runway under moving aircraft tire loading.

Lane et al. [14] presented a mesh movement algorithm where the elements are moved with the same velocity as the load in their study of dynamic vehicle interaction and wave propagation in a 3D finite element model. This requires a change of the grid in each time step. On the other hand, Dieterman and Metrikine [15] studied the analytical solution of the steady-state displacement of an Euler-Bernoulli beam resting on an elastic half space due to a uniformly constant moving load by introducing a coordinate transformation into a moving frame of reference. Krenk et al. [16] presented 2D formulation in a convected coordinate system moving with the load and using a transmitting boundary condition in the form of a spring-dashpot model for absorption of waves, modified to account for the translation velocity and the difference between compression and shear waves, see also [17]. The advantage of a transformation into moving coordinates is that a high mesh resolution can be concentrated around the load without any need of remeshing. This is especially important in 3D finite element modeling where computation time increases rapidly with increasing amount of elements.

In this paper, a formulation of the PML is developed in a moving frame of reference based on the PML formulation in [8]. In [18] an improved PML formulation

was presented for the acoustic problem, based on a coordinate transformation in the PML layer incorporating the direction dependence of the wave slowness diagram, but this techniques can not account for the different shear and compression wave speeds. The present formulation is given in 2D but it can be expanded to 3D as well. The procedure uses displacement based finite elements and represents the PML memory effect via two displacement-like auxiliary state-space variables. A parametric study of the PML parameters is conducted for optimizing the performance of the PML. Numerical examples show the response from a Ricker impulse load of various velocity obtained in two points placed behind and in front of the load, respectively, with equal distance to the load. The absorption abilities of the PML is evaluated in a single as well as a two layer half space. The effect of stiffness ratio between the top layer and the underlying layer in a 2-layer system is studied as well.

2. Perfectly Matched Layer (PML)

The present section introduces the method of a perfectly matched layer for absorbing out-going elastic waves. The method, introduced in [8], makes use of a formal coordinate transformation by which a regular wave in the transformed spatial coordinates is recast into an equivalent problem in the original coordinates in such a way that the coordinate transformation appears as coefficients in the governing equations that are subsequently solved by finite elements. The characteristic feature of the method is that the transformation is only introduced in a layer surrounding the computational domain, in which the transformation degenerates to an identity. Thus, the special features of the absorbing boundary condition only appear in the surrounding layer, which is included in the finite element model. The boundary layer is characterized by its thickness and parameters describing its dissipation

properties.

2.1. Two-dimensional wave propagation

The goal now is to set up a set of equations for a stretched 2D elasticity problem that incorporates damping if the coordinates are stretched, and specializes to the classic undamped elasticity equations if the original coordinates are retained without stretching. The equations of two-dimensional isotropic linear elasticity consist of the constitutive equations and the equations of motion. The constitutive equations relating the stresses $\boldsymbol{\sigma}$ and the derivatives of the displacements $\mathbf{u}$ are

$$\boldsymbol{\sigma} \,=\, \lambda\,(\boldsymbol{\nabla}^T\mathbf{u})\,\mathbf{I} \,+\, \mu\,\big[(\boldsymbol{\nabla}\mathbf{u}^T) + (\boldsymbol{\nabla}\mathbf{u}^T)^T\big] \tag{1}$$

where the gradient operator is defined by

$$\boldsymbol{\nabla} \,=\, \Big[\frac{\partial}{\partial x_1}, \frac{\partial}{\partial x_2}\Big]^T \tag{2}$$

and λ and μ are the Lamé parameters. When considering harmonic time variation represented via the factor $\exp(i\omega t)$, the equation of motion takes the form

$$(\boldsymbol{\nabla}^T\boldsymbol{\sigma})^T \,=\, -\omega^2\rho\,\mathbf{u} \tag{3}$$

where ρ is the mass density.

The original elasticity problem is now reformulated by using the notion of stretched coordinates. The idea is to introduce a set of stretched coordinates $\tilde{x}_j = \tilde{x}_j(x_j)$, defined in terms of the original coordinates x_j by the relation

$$\frac{\partial\tilde{x}_j}{\partial x_j} = s_j\,, \quad j = 1,2 \tag{4}$$

for the derivatives. It is noted that by this assumption each coordinate is stretched independently. In the present paper the stretching functions s_1 and s_2 are chosen

in the form

$$s_j(x_j) = 1 + \frac{\beta_j(x_j)}{i\,\omega}\,, \quad j = 1, 2. \tag{5}$$

The stretching functions deviate from unity by an additive term consisting of an attenuation function $\beta_j(x_j)$ depending on the coordinate x_j and assumed increasing through the bounding layer. The attenuation function is divided by the imaginary frequency factor $i\omega$. When converting the frequency representation to the time domain, the frequency factor $(i\omega)^{-1}$ corresponds to time integration in the same way the factor $i\omega$ corresponds to time differentiation. The role of the attenuation functions is to introduce an imaginary part that increases gradually from the interface between the elastic domain and the surrounding boundary layer. In the present paper this is accomplished by selecting the attenuation functions in the form, [19, 20],

$$\beta_j(x_j) \;=\; \beta_{\max} \left(\frac{x_j^p}{d} \right)^2 \tag{6}$$

where the superscript p denotes the corresponding coordinate with origin at the interface between the elastic domain and the boundary layer. The boundary layer surrounds the elastic region as illustrated in Figure 1 showing three side regions and two corner regions. In the side regions only the coordinate orthogonal to the interface is transformed, while both coordinates are transformed in the corner regions.

The idea now is to formulate a formal elasticity problem by using derivatives in terms of the stretched coordinates, and by introducing a suitable formal stress definition. Once the equations are formulated, the stretching parameters are absorbed into the constitutive parameters and the mass density corresponding to time differentiation and integration operators on the physical parameters λ, μ and ρ. The first step is to introduce the transformed gradient operator

$$\tilde{\boldsymbol{\nabla}} \;=\; \Big[\frac{\partial}{\partial \tilde{x}_1}, \frac{\partial}{\partial \tilde{x}_2} \Big]^T \;=\; \Big[\frac{1}{s_1} \frac{\partial}{\partial x_1}, \frac{1}{s_2} \frac{\partial}{\partial x_2} \Big]^T \tag{7}$$

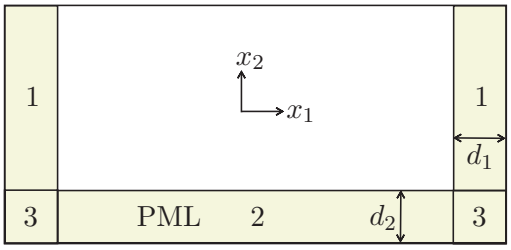

Figure 1: Region 1: $s_1 = 1 + \beta_1/i\omega$ and $s_2 = 1$, region 2: $s_1 = 1$ and $s_2 = 1 + \beta_2/i\omega$, region 3: $s_1 = 1 + \beta_1/i\omega$ and $s_2 = 1 + \beta_2/i\omega$. In the computational domain $s_1 = s_2 = 1$.

in terms of the stretched coordinates. In the boundary layer the use of this gradient operator would define a formal stress

$$\boldsymbol{\sigma} \;=\; \lambda\,(\tilde{\boldsymbol{\nabla}}^T\mathbf{u})\,\mathbf{I} \;+\; \mu\,\big[(\tilde{\boldsymbol{\nabla}}\mathbf{u}^T) + (\tilde{\boldsymbol{\nabla}}\mathbf{u}^T)^T\big]. \tag{8}$$

It follows from the format of this formal stress definition that the stress component matrix is symmetric, $\sigma_{12} = \sigma_{21}$. However, the formal strain matrix, given by the square brackets in (8), is now no longer symmetric, and the off-diagonal elements are defined in terms of the classic shear strain as well as the rotation. Thus, there are essentially four deformation components, but only three components in the formal stress matrix $\boldsymbol{\sigma}$. A resolution to the problem is suggested by the formal equation of motion,

$$(\tilde{\boldsymbol{\nabla}}^T\boldsymbol{\sigma})^T \;=\; -\omega^2\rho\,\mathbf{u} \tag{9}$$

The transformation of the gradient operator introduces factors s_j^{-1} on the derivatives corresponding to the first index of σ_{jk}. This suggests the use of a formal stress with components defined by, [3],

$$\tilde{\boldsymbol{\sigma}} \;=\; s_1 s_2 \begin{bmatrix} 1/s_1 & \\ & 1/s_2 \end{bmatrix} \boldsymbol{\sigma}\,. \tag{10}$$

The factor $s_1 s_2$ in this relation is suggested by the consideration that the final form of the formal stress-strain relation should not contain powers of s_j less than of degree -1 in order to enable a direct interpretation of the frequency problem in the time domain as discussed later.

When introducing the definition (10), the formal stress $\tilde{\boldsymbol{\sigma}}$ is related to a set of formal strains including the rotation component by a relation of the form

$$\tilde{\boldsymbol{\sigma}} \;=\; \tilde{\mathbf{C}}\,\boldsymbol{\varepsilon}\,. \tag{11}$$

In this relation it is convenient to introduce the formal stress in the array format

$$\bar{\boldsymbol{\sigma}} \;=\; \begin{bmatrix} \tilde{\sigma}_{11} \\ \tilde{\sigma}_{22} \\ \frac{1}{2}(\tilde{\sigma}_{21} + \tilde{\sigma}_{12}) \\ \frac{1}{2}(\tilde{\sigma}_{21} - \tilde{\sigma}_{12}) \end{bmatrix} \tag{12}$$

and the formal strains in the corresponding array format

$$\boldsymbol{\varepsilon} \;=\; \boldsymbol{\partial}\mathbf{u} \;=\; \begin{bmatrix} \partial_{x_1} & 0 \\ 0 & \partial_{x_2} \\ \partial_{x_2} & \partial_{x_1} \\ \partial_{x_2} & -\partial_{x_1} \end{bmatrix} \begin{bmatrix} u_1 \\ u_2 \end{bmatrix} \tag{13}$$

Straightforward substitution of (10) into the constitutive equations (8) then gives the constitutive matrix $\tilde{\mathbf{C}}$ in the form

$$\tilde{\mathbf{C}} \;=\; \mathbf{C}_0 \;+\; \frac{s_1}{s_2}\mathbf{C}_1 \;+\; \frac{s_2}{s_1}\mathbf{C}_2 \tag{14}$$

The non-stretched part $\mathbf{C}_0$ and the two stretched parts $\mathbf{C}_1$ and $\mathbf{C}_2$ are given by

$$\mathbf{C}_0 = \begin{bmatrix} 0 & \lambda & 0 & 0 \\ \lambda & 0 & 0 & 0 \\ 0 & 0 & \mu/2 & 0 \\ 0 & 0 & 0 & -\mu/2 \end{bmatrix}, \quad \mathbf{C}_1 = \begin{bmatrix} 0 & 0 & 0 & 0 \\ 0 & \lambda+2\mu & 0 & 0 \\ 0 & 0 & \mu/4 & \mu/4 \\ 0 & 0 & \mu/4 & \mu/4 \end{bmatrix},$$
$$\mathbf{C}_2 = \begin{bmatrix} \lambda+2\mu & 0 & 0 & 0 \\ 0 & 0 & 0 & 0 \\ 0 & 0 & \mu/4 & -\mu/4 \\ 0 & 0 & -\mu/4 & \mu/4 \end{bmatrix} \tag{15}$$

In the special case $s_1 = s_2 = 1$, used in the computational domain, the matrix takes the form

$$\mathbf{C} \;=\; \mathbf{C}_0 \;+\; \mathbf{C}_1 \;+\; \mathbf{C}_2 \tag{16}$$

corresponding to plane strain with symmetric stress components.

The equation of motion is obtained from (10), when disregarding the spatial derivatives of the factors s_1 and s_2. Hereby the equations of motion in terms of the formal stress $\bar{\boldsymbol{\sigma}}$ in the array format (12) take the form

$$\boldsymbol{\partial}^T \bar{\boldsymbol{\sigma}} \;=\; -\rho\, s_1 s_2 \omega^2\, \mathbf{u}\,, \tag{17}$$

where $\boldsymbol{\partial}$ is the spatial differential operator introduced in the strain definition (13).

2.2. Time domain equations

The frequency-dependent system of equations consisting of the constitutive equation (11) is transformed into time domain using the inverse Fourier transform. The constitutive equation takes the form

$$\bar{\boldsymbol{\sigma}} \;=\; \mathcal{C} * \boldsymbol{\varepsilon}\,, \tag{18}$$

where the symbol $*$ implies convolution with the time-dependent constitutive matrix defined by

$$\mathcal{C} \;=\; \mathbf{C} + \mathcal{F}_1(t)\mathbf{C}_1 + \mathcal{F}_2(t)\mathbf{C}_2 \tag{19}$$

It is noted that the matrix $\mathbf{C}$ corresponds to the standard time-independent form defined in (16). Thus, the functions $\mathcal{F}_1(t)$ and $\mathcal{F}_2(t)$ are the inverse Fourier transforms of $s_1/s_2 - 1$ and $s_2/s_1 - 1$, respectively,

$$\mathcal{F}_1(t) \;=\; (\beta_1 - \beta_2)e^{-\beta_2 t}, \quad t \geq 0 \tag{20a}$$

$$\mathcal{F}_2(t) \;=\; (\beta_2 - \beta_1)e^{-\beta_1 t}, \quad t \geq 0 \tag{20b}$$

The implementation of this formulation makes use of a time-step form in which the convolution integrals involving $\mathcal{F}_1(t)$ and $\mathcal{F}_2(t)$ are replaced by increments, thereby limiting the computations to the current time increment.

In the time domain the equation of motion (17) takes the form

$$\boldsymbol{\partial}^T \bar{\boldsymbol{\sigma}} \;=\; \mathcal{D}_0(t)\,\rho\,\mathbf{u}\,. \tag{21}$$

The operator $\mathcal{D}_0(t)$ is the inverse Fourier transform of $-\omega^2 s_1 s_2$ given by

$$\mathcal{D}_0(t) \;=\; \frac{d^2}{dt^2} + (\beta_1 + \beta_2)\frac{d}{dt} + \beta_1\beta_2 \tag{22}$$

The first term represents the inertia term, while the second term represents a velocity proportional viscous damping and the last term a mass-proportional stiffness, all acting on the absolute motion.

3. Convected Mesh Model

Following Krenk et al. [16] a convected coordinate system moving with the load is introduced via the relation

$$x = X - Vt \tag{23}$$

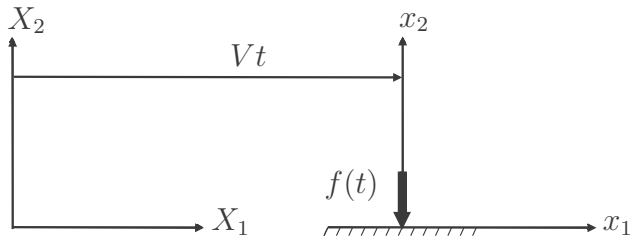

Figure 2: Moving surface load in fixed X_i-coordinate system

where X is the coordinate of the moving load in the fixed reference coordinate system, while x is the coordinate in the coordinate system following the load that is moving with velocity V. The relation (23) implies the following differentiation relations

$$\left.\frac{\partial}{\partial X}\right|_t = \left.\frac{\partial}{\partial x}\right|_t, \qquad \left.\frac{\partial}{\partial t}\right|_X = \left.\frac{\partial}{\partial t}\right|_x - V\frac{\partial}{\partial x} \tag{24}$$

Note that for convenience x is used instead of x_1 in the derivative with respect to x_1.

Substitution of these operators into the equation of motion (21) leads to the following modified form of the equilibrium equation in the moving coordinate system

$$\boldsymbol{\partial}^T \bar{\boldsymbol{\sigma}} = \tilde{\mathcal{D}}_0(t)\rho\mathbf{u} \tag{25}$$

with the convected time differentiation operator

$$\bar{\mathcal{D}}_0(t) = \left(\frac{\partial}{\partial t} - V\frac{\partial}{\partial x}\right)^2 + (\beta_1+\beta_2)\left(\frac{d}{dt} - V\frac{d}{dx}\right) + \beta_1\beta_2 \tag{26}$$

When using this operator in the dynamic equation (25) the following form of the equation is obtained

$$\begin{aligned}\boldsymbol{\partial}^T \bar{\boldsymbol{\sigma}} = \rho &\left(\frac{\partial^2\mathbf{u}}{\partial t^2} + (\beta_1+\beta_2)\frac{\partial\mathbf{u}}{\partial t} + \beta_1\beta_2\mathbf{u}\right) \\ &+ V^2\frac{\partial^2(\rho\mathbf{u})}{\partial x^2} - (\beta_1+\beta_2)V\frac{\partial(\rho\mathbf{u})}{\partial x} - 2V\frac{\partial^2(\rho\mathbf{u})}{\partial x\partial t}\end{aligned} \tag{27}$$

The first three terms on the right correspond to the representation in a fixed coordinate system, while the three last represent the effect of translation.

The convolution integrals in the constitutive relation (18) are related to the artificial properties of the boundary layer, and when assuming these properties convected with the load the form of the constitutive equation remains unchanged by the translation. Hereby the transformation from fixed to moving coordinates only modifies the dynamic equation, permitting a fairly straight forward implementation of the PML formulation in the translating formulation.

4. Finite element implementation

The principle of virtual work is used to obtain the weak formulation of the equation of motion (25), yielding

$$\int_V \tilde{\mathbf{u}}^T(\boldsymbol{\partial}^T\,\bar{\boldsymbol{\sigma}})dV - \int_V \tilde{\mathbf{u}}^T\tilde{\mathcal{D}}_0(t)\rho\,\mathbf{u}dV = 0 \tag{28}$$

The spatial variation of the actual and the virtual displacement fields are represented by shape functions as

$$\mathbf{u}(\mathbf{x},t) \;=\; \mathbf{N}(\mathbf{x})\,\mathbf{d}(t) \tag{29}$$

$$\tilde{\mathbf{u}}(\mathbf{x},t) \;=\; \tilde{\mathbf{N}}(\mathbf{x})\,\tilde{\mathbf{d}}(t) \tag{30}$$

with the shape function matrix $\mathbf{N}(\mathbf{x})$ in the form

$$\mathbf{N} = \begin{bmatrix} N_1 & 0 & N_2 & 0 & \cdots & N_n & 0 \\ 0 & N_1 & 0 & N_2 & \cdots & 0 & N_n \end{bmatrix} \tag{31}$$

and $\tilde{\mathbf{N}}$ on a similar form.

The shape functions are inserted in (28) which is reformulated using integration by parts in order to obtain a symmetric formulation

$$\begin{aligned}\int_V \Bigg\{ & \tilde{\boldsymbol{\varepsilon}}^T \bar{\boldsymbol{\sigma}} + \rho \tilde{\mathbf{u}}^T \ddot{\mathbf{u}} - \rho V \left(\tilde{\mathbf{u}}^T \frac{\partial \dot{\mathbf{u}}}{\partial x} - \dot{\mathbf{u}}^T \frac{\partial \tilde{\mathbf{u}}}{\partial x} \right) + \rho V^2 \frac{\partial \tilde{\mathbf{u}}^T}{\partial x} \frac{\partial \mathbf{u}}{\partial x} + \rho(\beta_1 + \beta_2) \tilde{\mathbf{u}}^T \dot{\mathbf{u}} \\ & + \tfrac{1}{2} \rho V (\beta_1 + \beta_2) \left(\mathbf{u}^T \frac{\partial \tilde{\mathbf{u}}}{\partial x} - \tilde{\mathbf{u}}^T \frac{\partial \mathbf{u}}{\partial x} \right) + \rho \beta_1 \beta_2 \tilde{\mathbf{u}}^T \mathbf{u} \Bigg\} dV \\ = \int_S \Bigg\{ & \tilde{\mathbf{u}}^T \boldsymbol{\sigma} \boldsymbol{n} + \rho V \tilde{\mathbf{u}}^T \left(\dot{\mathbf{u}} - V \frac{\partial \mathbf{u}}{\partial x} \right) \mathbf{n}_x + \tfrac{1}{2} \rho V (\beta_1 + \beta_2) \tilde{\mathbf{u}}^T \mathbf{u} \mathbf{n}_x \Bigg\} dS \end{aligned} \tag{32}$$

The load is traveling in the x_1-direction, and when assuming full attenuation within the PML-layer the surface is the only free boundary. Thus, the two last terms in the surface integral vanish.

Separating the convolution terms in the operators $\mathcal{F}_1(t)$ and $\mathcal{F}_2(t)$ in the constitutive matrix $\mathcal{C}$, the following set of ordinary differential equations is obtained

$$\mathbf{M}\ddot{\mathbf{u}} + \mathbf{Z}\dot{\mathbf{u}} + \mathbf{K}\mathbf{u} + \mathbf{g} = \mathbf{f} \tag{33}$$

where $\mathbf{u}$ is the global displacement vector and $\mathbf{f}$ is the global force vector, assumed to represent surface loads, whereby

$$\mathbf{f} = \int_S \tilde{\mathbf{N}}^T \boldsymbol{\sigma} \mathbf{n} \, dS \tag{34}$$

The element mass, damping and stiffness matrices are given by

$$\begin{aligned} \mathbf{M} &= \int_V \rho \tilde{\mathbf{N}}^T \mathbf{N} dV \\ \mathbf{Z} &= \int_V -\rho V (\tilde{\mathbf{N}}_x^T \mathbf{N} - \hat{\mathbf{N}}^T \mathbf{N}_x) + \rho(\beta_1 + \beta_2) \tilde{\mathbf{N}}^T \mathbf{N} dV \\ \mathbf{K} &= \int_V \Bigg\{ \tilde{\mathbf{B}}^T \mathbf{C} \mathbf{B} - \rho V^2 \tilde{\mathbf{N}}_x^T \mathbf{N}_x \\ &\quad + \tfrac{1}{2} \rho V \left(\beta_1 + \beta_2 \right) \left(\tilde{\mathbf{N}}_x^T \mathbf{N} - \tilde{\mathbf{N}}^T \mathbf{N}_x \right) + \rho \beta_1 \beta_2 \tilde{\mathbf{N}}^T \mathbf{N} \Bigg\} dV \end{aligned} \tag{35}$$

where $\mathbf{B}$ denotes the strain-displacement matrix and $\mathbf{N}$ the shape functions with x-derivative $\mathbf{N}_x = \partial\mathbf{N}/\partial x$.

Following [8] the convolution integrals from the constitutive relation, representing artificial damping in the PML, are now associated with the nodal displacements, whereby the corresponding vector $\mathbf{g}$ takes the form

$$\mathbf{g}^e = \mathbf{K}_1^e \, \mathcal{F}_1 * \mathbf{u}(t) + \mathbf{K}_2^e \, \mathcal{F}_2 * \mathbf{u}(t) \tag{36}$$

with element matrices $\mathbf{K}_1$ and $\mathbf{K}_2$ given by

$$\mathbf{K}_p^e = -\int_\Omega \mathbf{B}^T \mathbf{C}_p \mathbf{B} \, dV \,, \quad p = 1, 2 \tag{37}$$

By this, approximate, procedure the convolution terms $\mathcal{F}_p * \mathbf{u}(t)$ are defined using the value of the PML parameters at the nodes. The general appearance of the convolution term is

$$\mathcal{F}_p * \mathbf{u}(t) = \int_0^t \mathcal{F}_p(\tau)\mathbf{u}(t-\tau)\, d\tau = \int_0^t (\beta_{\bar{p}} - \beta_p) e^{-\beta_p \tau} \mathbf{u}(t-\tau)\, d\tau \tag{38}$$

with index $\bar{p}$ being the complement of p. In the integral the arguments τ and $t-\tau$ can be interchanged, and differentiation with respect to t then leads to the first-order 'filter type' equation

$$\frac{d}{dt}\Big(\mathcal{F}_p * \mathbf{u}(t)\Big) + \beta_p \Big(\mathcal{F}_p * \mathbf{u}(t)\Big) = (\beta_{\bar{p}} - \beta_p)\mathbf{u}(t) \tag{39}$$

When using this form, the functions $\mathbf{v}_p(t) = \mathcal{F}_p * \mathbf{u}(t)$, with dimension of displacement, can be considered as state-space variables and can be updated explicitly via a finite difference approximation as indicated in the description of the numerical algorithm in section 4.2. This constitutes a simple alternative to the procedure in [7] using a combined displacement stress-field representation. It may be argued

that the time derivative in the filter equation (39) should be modified to account for the moving frame. However, the fading memory is fictitious and need not be implemented in a stationary frame, and furthermore the representation of the spatial variation of the PML parameters has already been replaced by their nodal histories by (36).

4.1. Correction for moving frame

The translation of the coordinate system leads to terms proportional to V and V^2 in (27). These terms make the equations loose the original self-adjointness. In principle this can be compensated for by a modification of the shape functions. However, in the present problem it is simpler to use a technique developed by Krenk et al. [16] in which the terms $2\rho V\dot{\mathbf{u}}_x$ and $\rho V(\beta_1+\beta_2)\mathbf{u}_x$ are modified to account for the convection effect. A Taylor series expansion demonstrates that a straightforward Galerkin representation of these terms implies an error illustrated by the two-term Taylor expansion

$$\dot{\mathbf{u}}_x \simeq \frac{-\Delta\dot{\mathbf{u}}}{h} + \frac{1}{2}h\dot{\mathbf{u}}_{xx} \tag{40}$$

where h denotes the length of the increment Δx in the opposite direction of the load velocity. The first term on the right hand side of (40) is already properly represented by linear interpolation, hence the second term should be inserted in (27) for an improved formulation. The same procedure is used for the term $\rho V(\beta_1+\beta_2)\mathbf{u}_x$ and insertion of the terms of improvement in Eq. (27) yields

$$\begin{aligned}\boldsymbol{\partial}^T\bar{\boldsymbol{\sigma}} - \rho\Bigg(&\frac{\partial^2\mathbf{u}}{\partial t^2} + V^2\frac{\partial^2\left(\mathbf{u} - (h/V)\dot{\mathbf{u}} - \frac{1}{2}(h/V)(\beta_1+\beta_2)\mathbf{u}\right)}{\partial x^2}\\ &-2V\frac{\partial\dot{\mathbf{u}}}{\partial x} + (\beta_1+\beta_2)\frac{\partial\mathbf{u}}{\partial t} - (\beta_1+\beta_2)V\frac{\partial\mathbf{u}}{\partial x} + \beta_1\beta_2\mathbf{u}\Bigg)\end{aligned} \tag{41}$$

The introduction of the correction terms yields an extra contribution to the volume terms of the damping and stiffness matrix. The additional volume damping and stiffness matrices are

$$\begin{aligned} \mathbf{Z}_V &= h \int_V \rho V \tilde{\mathbf{N}}_x^T \mathbf{N}_x \, dV \\ \mathbf{K}_V &= h \int_V \tfrac{1}{2} \rho V (\beta_1 + \beta_2) \tilde{\mathbf{N}}_x^T \mathbf{N}_x \, dV \end{aligned} \tag{42}$$

The effect of the improved formulation is an additional convection term proportional to the second order derivative in space added to the full system in terms of damping and to the boundary layer in terms of stiffness. A suitable value for the convection correction parameter h was found by Krenk et al. [16] to be around $0.3 - 0.4$ times the length of the elements in the x-direction.

4.2. Time integration

The FE discretized system of equations are integrated in time using the Newmark-Beta time integration method [21]. The result is the following time marching of the elastic displacement field

$$\begin{aligned} &\left(\frac{1}{\Delta t^2} \mathbf{M} + \frac{1}{2\Delta t} \mathbf{Z} + \beta \mathbf{K} \right) \mathbf{u}^{n+1} \\ &= \left(\frac{2}{\Delta t^2} \mathbf{M} - (1 - 2\beta) \mathbf{K} \right) \mathbf{u}^n - \left(\frac{1}{\Delta t^2} \mathbf{M} - \frac{1}{2\Delta t} \mathbf{Z} + \beta \mathbf{K} \right) \mathbf{u}^{n-1} \\ &\quad - \beta \mathbf{g}^{n+1} - (1 - 2\beta) \mathbf{g}^n - \beta \mathbf{g}^{n-1} + \beta \mathbf{f}^{n+1} + (1 - 2\beta) \mathbf{f}^n + \beta \mathbf{f}^{n-1} \end{aligned} \tag{43}$$

The parameter, β, controls the interpolation between explicit and implicit time integration schemes. It has been shown that the integration scheme becomes unconditionally stable when $\beta \geq 1/4$. As opposed to explicit methods in which the time step Δt is bounded by the CFL condition, the implicit method has no limiting time

Algorithm 1 PML formulation in moving coordinates

1: Initialize $\mathbf{u}, \Delta t, V$
2: Build matrices $\mathbf{K}, \mathbf{M}, \mathbf{Z}$ ▷ eq. (35)
3: $t = 0$
4: **for** $i = 1 : i_{max}$ **do**
5: update $\mathbf{u}_n\, \mathbf{u}_{n-1}\, \mathbf{g}_n\, \mathbf{f}_n$ from previous time
6: Calculate $\mathbf{f}_{n+1}$ ▷ eq. (34)
7: Calculate $\mathbf{g}_{n+1}$ ▷ eq. (45), (44)
8: Solve for $\mathbf{u}_{n+1}$ ▷ eq. (43)
9: **end for**
10: Post processing

step. However, the time step should be chosen such that a minimum resolution of wave propagation is present. Zhai and Song [22] suggest a minimum time step of $\Delta t = 1/(8 f_{max})$ where f_{max} is the largest frequency present.

The value of $\mathbf{g}^{n+1}$ follows from (36), when expressed in the form

$$\mathbf{g}^{n+1} = \mathbf{K}_1\, \mathbf{v}_1^{n+1} + \mathbf{K}_2\, \mathbf{v}_2^{n+1} \tag{44}$$

with the auxiliary state-space vectors $\mathbf{v}_p^{n+1}$ determined from a finite difference form of the filter equations (39). A particularly simple form is a central difference around t_n and weight parameter β in the form

$$\frac{1}{2\Delta t}\big(\mathbf{v}_p^{n+1} - \mathbf{v}_p^{n-1}\big) + \beta_p\big(\beta \mathbf{v}_p^{n+1} + (1-2\beta)\mathbf{v}_p^{n} + \beta \mathbf{v}_p^{n-1}\big) = (\beta_{\bar{p}} - \beta_p)\mathbf{u}^n \tag{45}$$

This equation determines $\mathbf{v}_1^{n+1}$ and $\mathbf{v}_2^{n+1}$ leading to $\mathbf{g}^{n+1}$ by (44). For the discretization of the PML and the computational domain quadrilateral bilinear elements are employed. The procedure is presented in Algorithm 1.

5. Numerical Examples

In this section, numerical examples are conducted to demonstrate the absorbing properties of the PML formulated in a moving frame of reference. In that sense the Ricker pulse is used as an example of a moving source. In section 5.1, the PML boundary condition is verified against a large domain and the results are compared to a solution obtained by substituting the PML layer with fixed boundaries. The wave propagation is visualized with snapshots at four instances of time with PML boundaries and fixed boundaries, respectively. The simulation in a moving frame of reference is verified against a manually moved load in a static frame of reference. In section 5.2 a parametric study on the PML parameters is conducted. In section 5.3 and 5.4 the PML is used to study the response of a Ricker pulse traveling across the surface of a single- and a two-layer half space, respectively, with different velocities. Section 5.3 treats a single layer half space and demonstrates the change in response with velocity in front of and behind the load. Section 5.4 investigates the effect of putting a stiff layer on top of the soft subgrade for varying impedances.

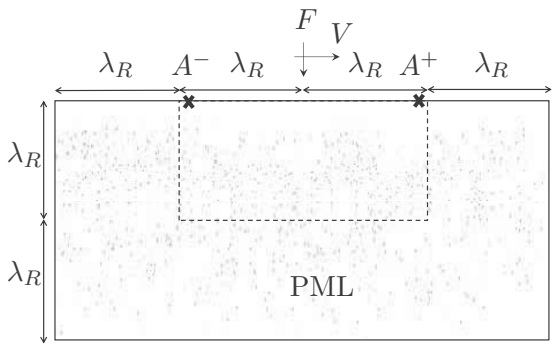

Figure 3: Domain of interest truncated by PML.

The numerical examples are based on the half space sketched in Figure 3. The

dashed line indicates the interface between the computational domain and the PML. F is the load acting at the center of the surface and V indicates the velocity and traveling direction of the load. In all numerical examples, the computational domain has a width of $2\lambda_R$ and a depth of λ_R , where λ_R is the Rayleigh wave length for the dominant load frequency.

The computational domain is surrounded by PML on 3 sides with a width of $d_i = \lambda_R$, unless specified otherwise. The PML is terminated by Dirichlet boundary conditions. The material parameters are $E = 60\text{MPa}$, $\nu = 0.35$ and $\rho = 1800\text{kg/m}^3$. The response of the pulse is captured in two observation points, A^+ and A^-. The two observation points are located with equal distance to the load on the surface in the computational domain, very close to the PML interface.

The load is a Ricker pulse acting in a single point defined as

$$P(t) = \tau(1-\tau^2)^2, \quad -1 < \tau < 1 \tag{46}$$

where $\tau = 2t/T - 1$. The duration of the pulse is 0.2s, hence the dominant frequency of the pulse is $f = 1/T = 5\,\text{Hz}$. In the numerical examples, the maximum load is $P_{max} = 50\,\text{kN}$. The time history of the Ricker pulse and its Fourier content is given in Figure 4.

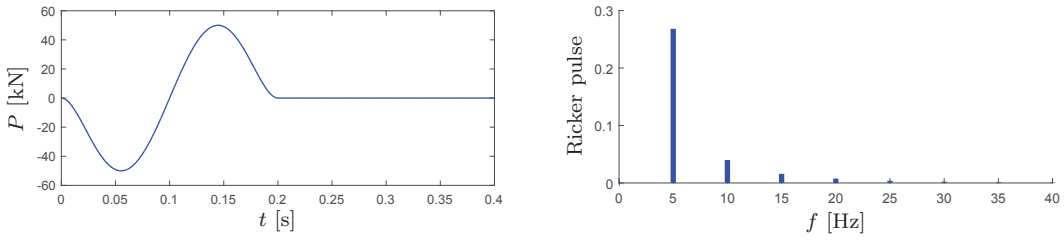

Figure 4: Ricker pulse and its Fourier spectrum.

In the time integration, the implicit version of the Newmark method is used, i.e. $\gamma = 1/2$ and $\beta = 1/4$ for unconditionally stable time marching. Although the time step is free of choice considering stability, it is essential to choose a time step that matches the temporal variation of the source. The choice of time step is therefore based on the CFL condition

$$\Delta t = \min\left(\frac{1}{c_p}, \frac{1}{c_s}\right)\left(\frac{1}{\Delta x_1^2} + \frac{1}{\Delta x_2^2}\right)^{-1/2} \tag{47}$$

as well as the previously mentioned condition $\Delta t \leq 1/(8 f_{max})$, where f_{max} is the largest frequency to be represented in the time history.

The 2D FE-model is implemented in Matlab. However, the recursive update of the convolution terms is done by a Mex function, due to the faster computation of a for-loop running over each element in the PML region. The element length is found sufficient to be 2.57m corresponding to 8 element s per Rayleigh wave length which is also suggested by [22, 23]. In the two-layer half space where the top layer is thinner than the element width of 2.57m, this layer consist of thin, wide elements with thickness equal to the layer thickness. In all numerical examples a Rayleigh type damping is imposed with a structural damping ratio of $\zeta = 0.01$ centered around the load frequency [24].

5.1. Verification of PML

Three numerical examples are used to verify the PML in moving coordinates. The wave propagation in a half space subjected to the Ricker pulse moving along the surface (Figure 3) is calculated in the first example. The response is studied in observation points A^+ and A^- for a half space truncated by PML, a half space with fixed boundaries and a reference value calculated in a large domain in which the waves do not reach the fixed boundaries within the simulation time. The traveling

velocity of the pulse is $V \simeq 22$m/s. The calculated time period is 1s and the time step is 0.0071s.

The time histories at the two observation points A^+ and A^- are displayed in Figure 5. The responses computed using PML agree well with the responses computed in a large domain. The responses computed with fixed boundaries are seen to be off from the reference responses quite early. This proves the applicability of the PML even very close to the interface to PML.

The vertical displacement field is visualized with snapshots at four instants in time with PML and with fixed boundaries, respectively, in Figure 6. The traveling velocity of the pulse is $V \simeq 44$m/s. After $10T_c$ corresponding to 2 seconds the wave has been fully absorbed in the PML (top row) while reflections of the wave are present at the same instants in time in case of fixed boundaries (bottom row).

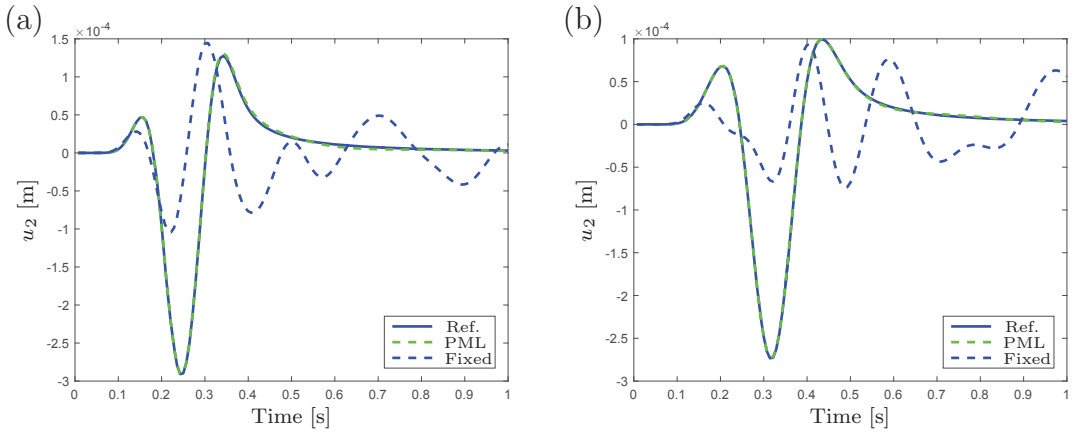

Figure 5: Vertical displacement at observation points, A^- and A^+.

The third example illustrates the response from a Ricker pulse traveling with velocity $V = 22\,\mathrm{m/s}$ in a moving frame of reference compared to the response from manually moving the Ricker pulse in a static frame of reference (Figure 7). In this

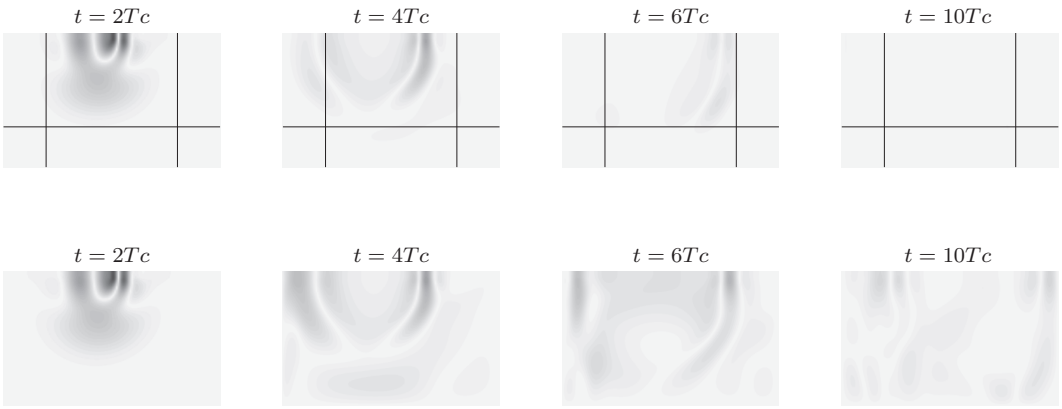

Figure 6: Snapshots of the vertical displacement field at four instances of time with Mach=0.4. Top row is with PML boundaries and bottom row is with fixed boundaries

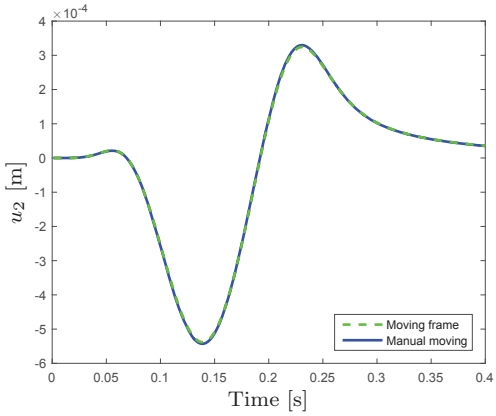

Figure 7: Response from Ricker pulse traveling with $V = 22\,\mathrm{m/s}$ in moving frame compared to static frame.

case the convection correction parameter is chosen to $h = 0.4l_x$ with l_x being the side length of the element in the x-direction. The response is recorded at the distance 4m ahead of the load source. The response obtained in the moving frame of reference

compares well with the response obtained in a static frame of reference.

5.2. Parametric study of the PML parameters

The absorbing properties of the PML are determined by a number of parameters. The choice of these parameters is essential for optimizing its performance. The spatial dependence of the PML attenuation function β_i in the x_i direction is chosen as a 2^{nd} order polynomial function as in [8, 20]

$$\beta_i = \beta_i^{max} \left(\frac{x_i^p}{d_i} \right)^2, \quad i = 1, 2 \tag{48}$$

in which x_i^p is measured from the interface to PML and d_i is the thickness of the PML layer. The coefficient β_i^{max} is given by [8]

$$\beta_i^{max} = -\frac{3c_p \log_{10}(R_0)}{2d_i} \tag{49}$$

where R_0 is the theoretical reflection coefficient at normal incidence and c_p is the pressure wave velocity. Good performance of PML depends on proper selection of β_{max}. Choosing it too small would result in pollution of the computational domain due to insufficient absorption. Choosing it too large will on the other hand result in spurious reflections from the interface due to inadequate representation of the PML by the discrete layer [20].

In this section, a parametric study of the free parameters in the attenuation function (49) is conducted to determine the optimal parameters for obtaining good accuracy and efficient computations.

The attenuation function has 3 parameters; c_p, R_0 and d_i where for simplicity $d_1 = d_2$. The pressure wave velocity c_p is given by the material properties of the medium, leaving 2 parameters to be determined. A parameter study on these 2 parameters has been conducted, and the results are shown in Figure 8-9. The

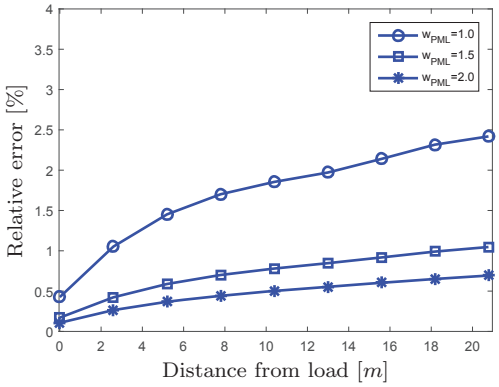

Figure 8: Maximum relative error at a number of observation points computed using the PML widths $\mathrm{w_{PML}} = d_i/\lambda_{c_r} = 1.0, 1.5, 2.0$.

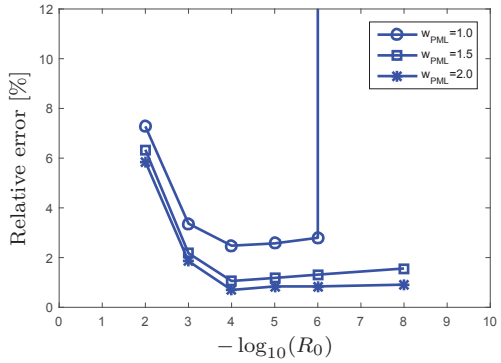

Figure 9: Maximum relative error as function of R_0 for each PML width. $n = 2$.

results are expressed as the maximum relative error between the transient response from the Ricker pulse using PML and the reference value introduced in the previous section, calculated as

$$\text{relative error} = \frac{\max\left|U^{PML} - U^{ref}\right|}{\max(U^{ref})} \tag{50}$$

where U is the transient response obtained at a certain observation point, and the exponents denotes whether the response is obtained using PML or it is the reference value. The simulations have been running for 1.5 s ensuring enough time for the

waves to reflect back to the origin of the load source for the thickest PML layer of interest. All tests are done for the PML thicknesses $d_i = 0.5\lambda_{c_r}$, λ_{c_r}, $1.5\lambda_{c_r}$ and $2\lambda_{c_r}$. However, a PML width of $0.5\lambda_{c_r}$ turns out to be too thin and the response diverges. The errors obtained from using this thin layer are therefore not presented in Figures 8 and 9.

Figure 8 illustrates the performance of the PML with the different PML layer thicknesses. The response is obtained at a number of observation points on the surface from under the load source to the interface of PML. The spacing between the observation points is one element length. The reflection coefficient is $R_0 = 10^{-4}$. For a PML width of $d_i = \lambda_{c_r}$, the relative error under the load source is $< 0.5\%$ increasing to 2.5% at the interface to PML. The relative errors for $d_i = 1.5\lambda_{c_r}$ and $d_i = 2\lambda_{c_r}$ varies closely between 0–1% from under the load source to the PML interface. This corresponds to an absolute error of 4–5 μm for $d_i = \lambda_{c_r}$ and 1–2 μm for $d_i = 1.5\lambda_{c_r}$. Whether to choose $d_i = \lambda_{c_r}$ or $d_i = 1.5\lambda_{c_r}$ comes down to a balance between accuracy and computational efficiency. In the further examples of this paper, $d_i = 1.5\lambda_{c_r}$ is used.

In Figure 9, the relative error from the variation of the reflection coefficient between $R_0 = 10^{-2} - 10^{-8}$ is illustrated for the different widths. This figure shows for all thicknesses that the best choice of reflection coefficient lies in the area of $R_0 = 10^{-4}$. Choosing it any smaller will not improve the result and will at some point lead to a divergence of the response (as seen for $d_i = \lambda_{c_r}$ with $R_0 < 10^{-6}$. Choosing a larger R_0 results in a significant increase of the maximum relative error. In the further numerical examples, $R_0 = 10^{-4}$ is used.

The following examples in this paper are based on the reflection coefficient $R_0 = 10^{-4}$ and the PML width $d_i = 1.5\lambda_{c_r}$ corresponding to 8 elements.

5.3. Single layer half space

The simplest case for testing the performance of the PML is to apply a Ricker pulse load to a single layer half space (Figure 3). The pulse is traveling on the surface with different velocities in the horizontal direction. The velocity is expressed in relation to the shear wave velocity of the soil as the Mach value

$$\text{Mach} = V/c_s \tag{51}$$

The response is obtained in Figure 10 at Mach 0, 0.2 and 0.4. The pulse arrives

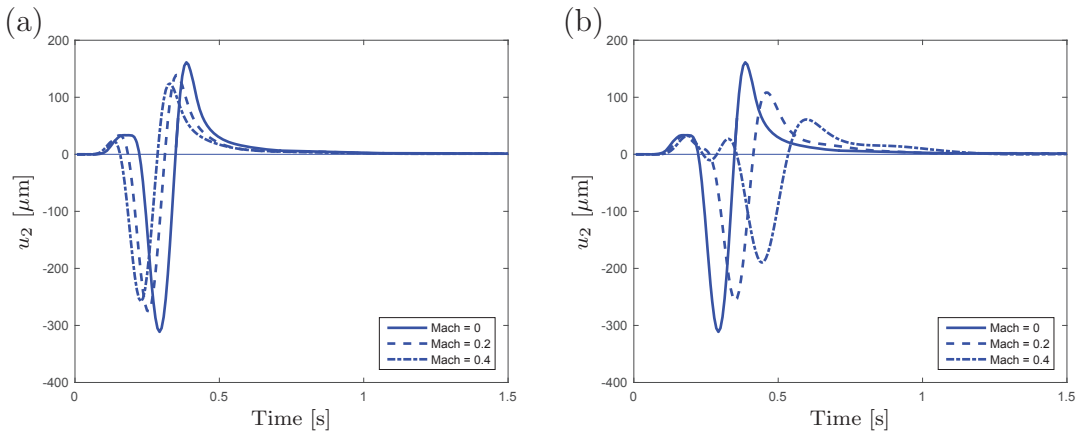

Figure 10: Deflection response in points A^- (a) and A^+ (b) for single layer system.

with the speed $c+V$ behind the load, point A^-, and it arrives with the speed $c-V$ in front of the load, at point A^+. I.e. for a fixed point in front of the moving load the frequency increases while it decreases for a fixed point behind the moving load.

Hence, the wave length defined by c/f is changing according to the change in speed, given by

$$f = \left(\frac{c}{c+V}\right) f_0 \tag{52}$$

where c is the wave velocity of the medium, V is velocity of the pulse and f_0 is the frequency of the load. It follows from this equation that by increasing the speed of the source, the resulting frequency is spread over a wider range of frequencies. Hence, the PML width needs to be chosen such that the shortest wavelength is ensured a resolution of 8 elements.

The dynamic response is seen to decrease with velocity (Fig. 10). This is especially clear in front of the load where the maximum deflection decreases by approximately 30%. This is in agreement with the results found by [16]. An opposite observation can be made in case of a constant moving load. In this case, the response increases by increasing velocity [25, 26].

The Ricker pulse traveling with velocities Mach 0, 0.2 and 0.4 is fully absorbed by the PML layer in the single layer half space.

5.4. Two layer half space

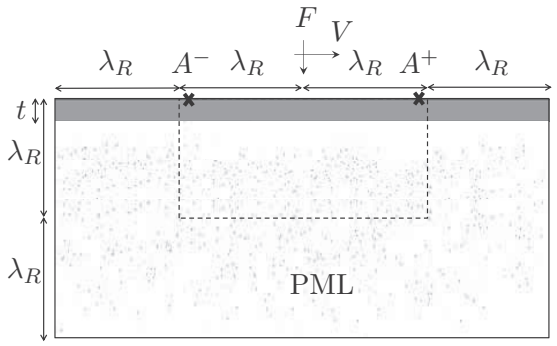

Figure 11: Domain of interest with stiff top layer truncated by PML.

In this example the effect of two layers on the response of a Ricker pulse is studied. The pulse is the one illustrated in Figure 4 used in the previous example. A 100 mm stiff layer is added on top of the single layer treated in section 5.3 as

sketched in Figure 11. The density of the top layer is $\rho = 2300\,\mathrm{kg/m^3}$ and Poisson's ratio is $\nu = 0.35$. The effect of impedance ratio is analysed in the following examples where Young's modulus of the top layer is chosen to E, $10E$ and $100E$, respectively, where $E = 60\,\mathrm{MPa}$ is the modulus of the bottom layer. The response in point A^+ and A^- obtained from the Ricker load of zero velocity acting on the two layer system with varying top layer stiffness is seen in Figure 12. The first two peaks of

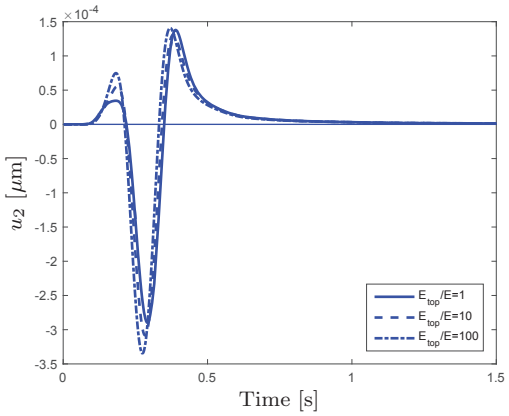

Figure 12: Response from Ricker wavelet acting on a two layer system with top layer stiffness E, $10E$ and $100E$ at Mach=0.

the response are seen to increase with increasing impedance ratio. Also, the wave period becomes shorter as the impedance ratio increases. This is explained from the fact that the wave period is given by $T = \lambda/c$. The wave velocity of the two-layer system is a combination of the wave velocities of the top and the bottom layer. Since the wave velocity in the top layer is larger than that of the bottom layer, the wave velocity of the system will increase with increasing impedance ratio. Hence, the wave period will decrease. The response in point A^+ equals the response in point A^- due to symmetric wave propagation.

Increasing the velocity of the load to Mach = 0.4 yields the responses in point

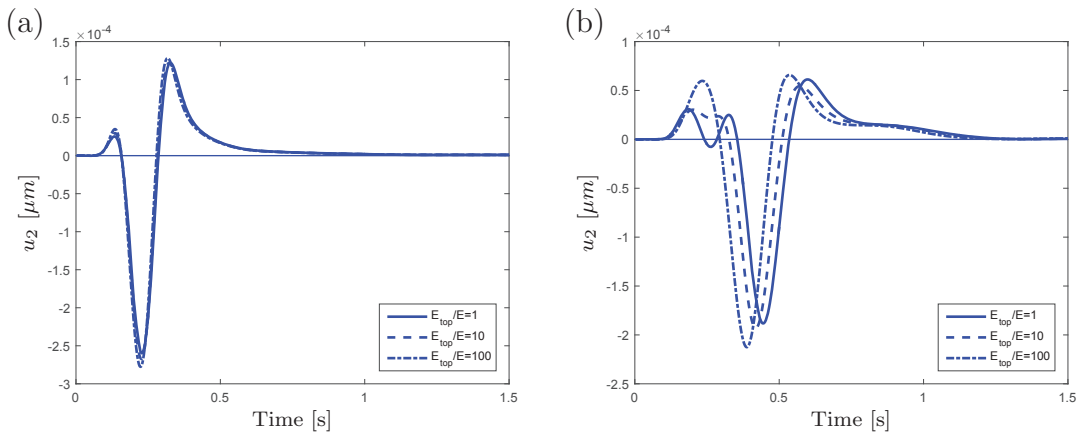

Figure 13: Deflection response in points A^- (a) and A^+ (b) for a two layer system with top layer stiffness E, $10E$ and $100E$ at Mach=0.4.

A^+ and A^- given in Figure 13. A high impedance ratio is seen to have a significant influence on the response obtained in front of the load (Figure 13b). The negative displacement peak increases around 13% when the impedance ratio equals 100. This peak also occurs approximately 0.05 s earlier compared to the response obtained in the single layer example. On the other hand, the response obtained behind the load does not change substantially. The effects observed for the response in front of the load are only seen to minor degree behind the load.

In a two-layer system c_p in the subgrade is still dominating the wave velocity, hence this value is valid for use in the attenuation function in the PML layer.

6. Conclusions

The Perfectly Matched Layer (PML) has been formulated in a moving frame of reference. With this formulation, the FE-model can be limited to the domain of interest yielding computational efficiency.

The PML demonstrates great absorbing abilities and numerical examples verifies that an accurate response can be obtained very close to the PML interface. The parametric study of the PML parameters showed that a PML width of 1.5 Rayleigh wave length with respect to the dominating load frequency is sufficient to achieve good accuracy in the response, i.e. a maximum relative error of less than 1% close to the interface to the PML layer. The optimal reflection coefficient to solve the treated problem was found to be around $R_0 = 10^{-4}$.

Numerical examples have been conducted for a single- and a two-layer half space. These examples clarifies that the wave propagation is dominated by the properties of the subgrade in the pavement. Hence the PML parameters can in a multi layered pavement system be set according to the properties of the subgrade.

The stiffness ratio between top layer and the underlying layer has a significant effect on the response obtained in front of the load. The response is seen to increase with increasing stiffness of the top layer and the arrival time of the response decreases.

7. Acknowledgements

This work is supported by the Innovation Fund Denmark through the grant 'High-Speed Pavement Assessment Tool for Better and Safer Roads'.

References

[1] J.-P. Berenger, A perfectly matched layer for the absorption of electromagnetic waves, Journal of Computational Physics 114 (1994) 185–200.

[2] W. C. Chew, W. H. Weedon, A 3D perfectly matched medium from modi-

fied Maxwell's equations with stretched coordinates, Microwave and Optical Technology Letters 7 (1994) 599–604.

[3] W. C. Chew, Q. H. Liu, Perfectly matched layers for elastodynamics: A new absorbing boundary condition, Journal of Computational Acoustics 4 (1996) 341–359.

[4] U. Basu, A. K. Chopra, Perfectly matched layers for time-harmonic elastodynamics of unbounded domains: Theory and finite-element implementation, Computer Methods in Applied Mechanics and Engineering 192 (2003) 1337–1375.

[5] U. Basu, A. K. Chopra, Perfectly matched layers for transient elastodynamics of unbounded domains, International Journal for Numerical Methods in Engineering 59 (2004) 1039–1074.

[6] U. Basu, Explicit finite element perfectly matched layer for transient three-dimensional elastic waves, International Journal for Numerical Methods in Engineering 77 (2) (2009) 151–176.

[7] S. Kucukcoban, L. F. Kallivokas, Mixed perfectly-matched-layers for direct transient analysis in 2D elastic heterogeneous media, Computer Methods in Applied Mechanics and Engineering 200 (2011) 57–76.

[8] R. Matzen, An efficient finite element time-domain formulation for the elastic second-order wave equation: A non-split complex frequency shifted convolutional PML, International Journal for Numerical Methods in Engineering 88 (2011) 951–973.

[9] E. Bécache, S. Fauqueux, J. P, Stability of perfectly matched layers, group velocities and anisotropic waves, Journal of Computational Physics 188 (2003) 399–433.

[10] K. Duru, G. Kreiss, Numerical interaction of boundary waves with perfectly matched layers in two space dimensional elastic wave guides, Wave Motion 51 (2014) 445–465.

[11] K. Duru, G. Kreiss, Boundary waves and stability of the perfectly matched layer for the two space dimensional elastic wave equation in second order format, SIAM Journal of Numerical Analysis 52 (2014) 2883–2904.

[12] P. Yoo, I. Al-Qadi, Effect of transient dynamic loading on flexible pavements, Transportation Research Record: Journal of the Transportation Research Board 1990 (2007) 129–140.

[13] H. Wang, I. Al-Qadi, S. Portas, M. Coni, Three-dimensional finite element modeling of instrumented airport runway pavement responses, Transportation Research Record: Journal of the Transportation Research Board 2367 (2013) 76–83.

[14] H. Lane, P. Kettil, N.-E. Wiberg, Moving finite elements and dynamic vehicle interaction, European Journal of Mechanics - A/Solids 27 (4) (2008) 515–531.

[15] H. A. Dieterman, V. Metrikine, Steady-state displacements of a beam on an elastic half-space due to a uniformly moving constant load, European Journal of Mechanics - Series A/Solids 16 (1997) 295–306.

[16] S. Krenk, L. Kellezi, S. R. K. Nielsen, P. Kirkegaard, Finite element and transmitting boundary conditions for moving loads, in: Proceedings of the 4th Euro-

pean Conference on Structural Dynamics, Eurodyn'99, Balkema, The Netherlands, 1999, pp. 447–452.

[17] L. Andersen, S. R. K. Nielsen, S. Krenk, Numerical methods for analysis of structure and ground vibration from moving loads, Computers & Structures 85 (2007) 43–58.

[18] J. Diaz, J. P, A time domain analysis of PML modfels in acoustics, Computer Methods in Applied Mechanics and Engineering 195 (2006) 3820–3853.

[19] Y. Zheng, X. Huang, Anisotropic perfectly matched layers for elastic waves in Cartesian and curvilinear coordinates, Tech. rep., Massachusetts Institute of Technology, Earth Resources Laboratory (2002).

[20] I. Harari, U. Albocher, Studies of FE/PML for exterior problems of time-harmonic elastic waves, Computer Methods in Applied Mechanics and Engineering 195 (2006) 3854–3879.

[21] N. M. Newmark, A method of computation for structural dynamics., Journal of the Engineering Mechanics Division, ASCE 85.

[22] W. Zhai, E. Song, Three dimensional FEM of moving coordinates for the analysis of transient vibrations due to moving loads, Computers and Geotechnics 37 (2010) 164–174.

[23] J. Lysmer, Analytical procedures in soil dynamics, Tech. Rep. UCB/EERC-78/29, Earthquake Engineering Research Center, University of California, Berkeley.

[24] P. Vinh, R. Ogden, On formulas for the Rayleigh wave speed, Wave Motion 39 (2004) 191–197.

[25] A. V. Metrikine, H. A. Dieterman, Lateral vibrations of an axially compressed beam on an elastic half-space due to a moving lateral load, European Journal of Mechanics - A/Solids 18 (1999) 147–158.

[26] H. H. Hung, Y. B. Yang, Elastic waves in visco-elastic half-space generated by various vehicle loads, Soil Dynamics and Earthquake Engineering 21 (2001) 1–17.

[P2]

"Dynamic backcalculation with different load-time histories"

Stine S. Madsen and Eyal Levenberg

Submitted: *Road Materials and Pavement Design, 2016*

Dynamic backcalculation with different load-time histories

Stine Skov Madsen[1], Eyal Levenberg[2]

[1]*Solid Mechanics, Department of Mechanical Engineering, Technical University of Denmark*

[2]*Geotechnics and geology, Department of Civil Engineering, Technical University of Denmark*

Abstract

This paper focused attention to the Falling Weight Deflectometer (FWD) load-time history. For a commonly used device, it studied the pulse generation mechanism and the influence of different load histories on backcalculation results. In this connection, a semi-analytic impact theory was first introduced for realistically simulating FWD pulse generation. Then a newly developed finite element code was presented for FWD interpretation; the code is capable of addressing dynamics, time-dependent layer properties, and quasi-nonlinear behavior. Both new developments were demonstrated for an experimental dataset that resulted from operating an FWD with different loading configurations. It was found that backcalculated parameters were sensitive to the FWD pulse features. Consequently, it is recommended that, whenever advanced pavement characterization is sought, experimental attention should be placed on generating diverse FWD pulse histories. Collectively, the resulting deflection histories will contain pertinent constitutive information for supporting the calibration of more complex pavement models.

Keywords: Falling weight deflectometer, Finite element method, Dynamic backcalculation, load-time history

1. Introduction

The Falling Weight Deflectometer (FWD) is a standard non-destructive testing device for the pavement industry (ASTM, 2015). In general terms, an FWD is designed to generate a short load pulse at the pavement surface, of the order of 30 milliseconds in duration, and record the associated surface deflections. This impact type of loading is achieved by dropping a weight from a predetermined height, and the deflections are measured by an array of geophones. In most cases FWD measurements are interpreted with the aim of identifying the in situ mechanical properties of the individual system layers (e.g. Bush et al. (1989); Quintus et al. (1994); Tayabji et al. (2000)). This is commonly performed by means of backcalculation, wherein model-generated deflections are matched against field-measured deflections.

Based on the underlying choice for pavement modelling, backcalculation schemes may differ in complexity (e.g., Ullidtz and Stubstad (1985); Shao et al. (1986); Chatti et al. (2004); Lee (2014)). Traditional procedures, which are still widely employed by engineers, ignore inertia effects, disregard time-dependent layer properties, and focus on matching peak deflections only; most are also limited to linear behaviour and isotropic properties. The more advanced schemes allow for backcalculation of time-dependent properties, nonlinear behavior, and consider dynamic effects; these focus on matching entire deflection histories. The large body of research associated with the FWD has mainly dealt with two aspects: (i) forward pavement modelling, and (ii) performing the inverse problem. Rather limited work has addressed the device loading mechanism, i.e., the ability of controlling or regulating the FWD pulse history, and consequently the influence such manipulation has on the interpretation outcomes.

This paper focuses attention to the FWD load-time history; it studies the pulse generation mechanism and attributes, and also the influence of different load histories on backcalculated outcomes. A semi-analytic impact theory is first introduced, potentially capable of simulating FWD pulse histories. Then, the impact theory is applied to the analysis of drop experiments; these included operating an FWD with different loading configurations over a given pavement. Presented next is a new finite element (FE) code for forward-modelling the response of pavements to FWD impact. This new code is capable of addressing dynamics, time-dependent layer properties, and continuous change in properties with depth (i.e., quasi-nonlinear behaviour).

Corresponding author: Stine Skov Madsen, Email: sskk@mek.dtu.dk

Lastly, the FE code is employed to backcalculate the measured deflections from the drop experiments, and investigate the effects of the different loading histories on the inferred layer properties. The specific investigation results are presented and discussed, from which some general conclusions are offered.

2. Impact analysis

2.1. Semi-analytic model

A simplified analytic model for FWD impact was offered by Sebaaly et al. (1985). Their work considered (see Figure 1) a mass m with an underlying weightless buffer that is dropped from a certain height; the buffer was represented by a linear spring with stiffness k. In this case the governing differential equation is simply: $m\ddot{x} + kx = mg$ wherein g is the gravitational acceleration of the earth, x denotes the vertical position of the mass at time t, and $\dot{(\cdot)}$ indicates differentiation with respect to time.

The solution for this equation commences when contact is first made with the ground and the spring begins to compress. The initial conditions are therefore $x(0) = 0$ and $\dot{x}(0) = \sqrt{2gx_0}$ wherein x_0 is the drop height. If the spring remains 'glued' to the pavement surface after impact, the load-time history applied to the pavement $F(t) = kx(t)$ can be expressed analytically as follows

$$F(t) = \sqrt{2mgx_0k}\sin(t\sqrt{k/m}) - mg\cos(t\sqrt{k/m}) + mg \tag{1}$$

The shape of this load-time history is approximately a haversine, with a 'first pulse' duration ΔT_1 given by

$$\Delta T_1 = \sqrt{\frac{k}{m}}\left(\arctan\left(\frac{2\sqrt{2kx_0mg}}{2kx_0 - mg}\right) + \pi\right) \tag{2}$$

A typical FWD configuration drops masses in the range of 100 to 400 kg from heights in the range of 0.05 to 0.40 m. Considering a realistic example with $m = 100$ kg and $k = 10^6$ N/m, it can be seen from the above expression that if x_0 is increased from 0.05 to 0.40 m the first pulse duration varies only marginally, between 33.4 and 32.1 ms. On the other hand, the peak load varies considerably between 10.9 to 29.0 kN. It can therefore be concluded that for a given mass, adjusting the drop height provides some control over the peak load without influencing the pulse duration. Alternatively, by changing the mass or the buffer properties (or both) different pulse durations can be produced for different peak loads.

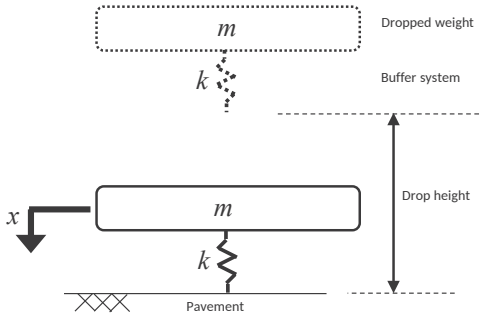

Figure 1: Simplified FWD loading model

Generation of FWD load-time history was investigated further by Lukanen (1992). His work dealt with different buffer designs, and experimentally demonstrated that load pulses do not approximate a haversine shape. In actuality, the rate of load rise was higher compared with the unloading rate, and very often some undulation or ripple appeared before the peak. Changing the buffer cross-sectional design (flat, rounded, or semi-rounded), was also demonstrated to influence the pulse shape.

As means of capturing the aforementioned effects, a refined and more realistic FWD loading model is hereafter proposed. The model is shown in Figure 2; it is based on a typical and popular FWD device configuration (specifically, Dynatest 8000). Three separate masses are included, wherein m_1 represents the dropped mass, m_2 represents the hit bracket, and m_3 represents the loading plate. In a typical FWD operation, the three masses are first placed quasi-statically on the pavement. Then, m_1 is elevated and allowed to free-fall. The buffer system underlying m_1 is considered weightless in the model, represented by a

spring and dashpot in parallel. The dashpot simulates simple Newtonian damping with viscosity c_1 while the spring is chosen as nonlinear-hardening: $k_1^{nl} = k_{11} + k_{12}x^2$. This latter choice is necessary for capturing and reproducing the effects of different cross-sectional buffer designs. The drop height (x_0) measures the initial vertical distance between the buffer system and the hit bracket (m_2).

The FWD load-cell, which records the applied load-time history, is represented by a massless linear spring with constant k_2. As can be seen in the figure, it is positioned between m_2 and m_3 to measure the load transferred between the two. While this is not the load directly applied to the pavement surface, the error involved is relatively small because k_2 is large. The load-cell mass is included in both m_2 and m_3 (split between the two). The final model component is the Viton rubber that resides between the load plate the pavement surface. It is mainly introduced to ensure full contact across the loaded area between the perfectly flat metallic load plate and the tested surface (which is never perfectly flat) and promote the generation of a uniform stress distribution (Uzan and Lytton, 1990). This Viton rubber is represented by a single Kelvin-Voigt viscoelastic element with a spring constant k_3 and dashpot viscosity c_3. In this connection, it is important to note that the bottom of the Viton is taken as perfectly rigid. This assumption is incorrect given that the pavement deforms due to the loading. Consequently, the Kelvin-Voigt element properties can be viewed to represent some combination of the Viton properties and the pavement properties.

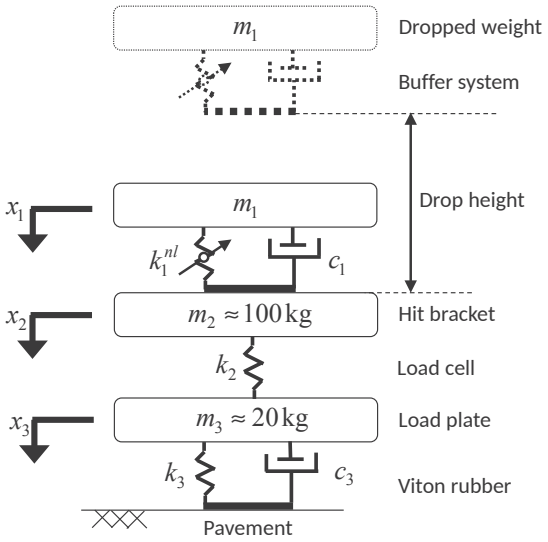

Figure 2: Realistic FWD loading model

The following nonlinear set of three differential equations (3)-(5) is associated with the FWD model shown in Figure 2. Each equation represents dynamic equilibrium over one of the masses. The formulation is based on the premise that the Viton rubber does not detach from the pavement. On the other hand, allowance is given in the formulation for m_1 to bounce off and separate from m_2. For this purpose the Macaulay brackets (defined as $\langle x \rangle = 0.5x + 0.5|x|$) are introduced to mathematically prevent tension from taking place between the two masses:

$$m_1 g = m_1 \ddot{x}_1 + \langle c_1(\dot{x}_1 - \dot{x}_2) + k_{11}(x_1 - x_2) + k_{12}(x_1 - x_2)^3 \rangle \tag{3}$$

$$\langle c_1(\dot{x}_1 - \dot{x}_2) + k_{11}(x_1 - x_2) + k_{12}(x_1 - x_2)^3 \rangle = m_2 \ddot{x}_2 + k_2(x_2 - x_3) \tag{4}$$

$$k_2(x_2 - x_3) = m_3 \ddot{x}_3 + c_3 \dot{x}_3 + k_3 x_3 \tag{5}$$

When solving these equations, analysis commences at the instant the buffer system makes first contact with the hit bracket (m_2). The associated initial conditions in this case are: $x_1(0) = x_2(0) = x_3(0) = 0$, $\dot{x}_2(0) = \dot{x}_3(0) = 0$, and $\dot{x}_1(0) = \sqrt{2x_0 g}$. In the following section this model is applied to investigate experimentally measured load-time histories.

Test	Buffers	Drop mass [kg]	Drop height [mm]	Pulse duration [ms]	Peak load [kN]
1	4	250	400	29.5	86
2	4	250	200	33.0	52
3	4	250	50	37.0	23
4	2	150	100	39.0	17
5	2	250	100	47.5	26
6	2	350	100	52.0	35
7	2	250	175	44.0	35
8	6	350	50	35.5	35

Table 1: Selected FWD drop experiments: pulse features and device operational settings.

2.2. ***Experimental***

FWD drop experiments took place inside a 50 m × 50 m hangar isolated from outside environment. The hangar floor was made of a cast-in-place concrete with an average thickness of 150 mm. Below the concrete was a layer of 200 mm of uniformly graded, round gravel overlaying a typical Danish glacial bolder clay with granite inclusions of up to 100 mm in size. Based on nearby bore logs, the bolder clay at the site extends to a depth of about 8 m and the water table level is deeper than 20 m. In the end of 2014 a portion of the concrete floor was replaced with a new asphalt pavement. A rectangular cut of 5 m × 3 m in size was performed and the underlying materials were excavated to a depth of 550 mm. The bottom was compacted with vibratory rollers to serve as formation level for a 520 mm pavement structure consisting of 400 mm of crushed granular base and 120 mm of asphalt concrete (AC). The base was compacted in several lifts using a Jumping Jack compactor and the asphalt layer was compacted in two lifts by a double-drum steel-wheeled roller and a vibratory plate. The AC mixture consisted of a combination of crushed and uncrushed materials with a maximum aggregate size of 22.4 mm, and a relatively soft bitumen graded as 70/100 (EN 12591). Figure 3 graphically presents the above description; Figure 3(a) presents an overhead view of the testing area and Figure 3(b) presents a cross-sectional view. As may be seen, the surface of the asphalt pavement was slightly lower than the surrounding concrete floor allowing for a future addition of a 30 mm AC lift.

In the end of 2015 (i.e., about a year after construction), the asphalt pavement was tested by an FWD. The specific device used was a Dynatest model 8012 which is capable of faster operation as compared to traditional systems, but is essentially identical to standard devices for all practical reasons. The load plate was positioned as seen in Figure 3(a) along with eight geophones placed at the following offset distances (from the center): 0, 200, 300, 600, 900, 1200, 1500 and 1800 mm. The load plate was 300 mm in diameter; it was segmented into four parts and included a 6 mm Viton rubber placed underneath it. The buffers used for the testing were hard cylinder buffers (Shore hardness of 80A), slightly rounded at the tip having a 110 mm diameter and a height of 84 mm.

A total of 24 FWD drops were executed, spanning the full operational range of the device in terms of: drop height, drop weight, and number of buffers. All drops were executed within a period of 0.5 hours, during which the AC temperature was 22°C. Eight separate FWD tests out of the 24 were selected for further analysis in this study (numbered sequentially for convenience). Their load-time histories are presented by the dotted lines in Figure 4 while the associated operational settings and load-time history features are listed in Table 1. Figure 4(a) shows three tests for which only the drop height differed. As can be seen, for a given buffer configuration and drop mass, increasing the drop height generates an increase in the peak load and a shortening of the pulse length (i.e. earlier peak occurrence). Figure 4(b) shows three drops for which the drop height and the buffer arrangement were kept constant, but the dropped mass differed. In this case, as the mass was increased, both the peak load and the pulse duration increased (i.e. later peak occurrence). Figure 4(c) includes three tests that exhibited nearly identical peaks but different pulse durations. These drops can not be generated by adjusting or varying only one single device option.

Also included in Figure 4 (as solid lines) are computed load-time histories. These were generated from numerically solving the set of equations (3),(4) and (5) within the time interval $t = 0$ to $t = 0.7$ s by a Runge-Kutta-Fehlberg method (fourth-fifth order). The employed model parameters are given in Table 2. These values were obtained from best fitting the measured FWD pulses across different test configurations. As expected, the parameters k_{11}, k_{12} and c_1 change based on the number of

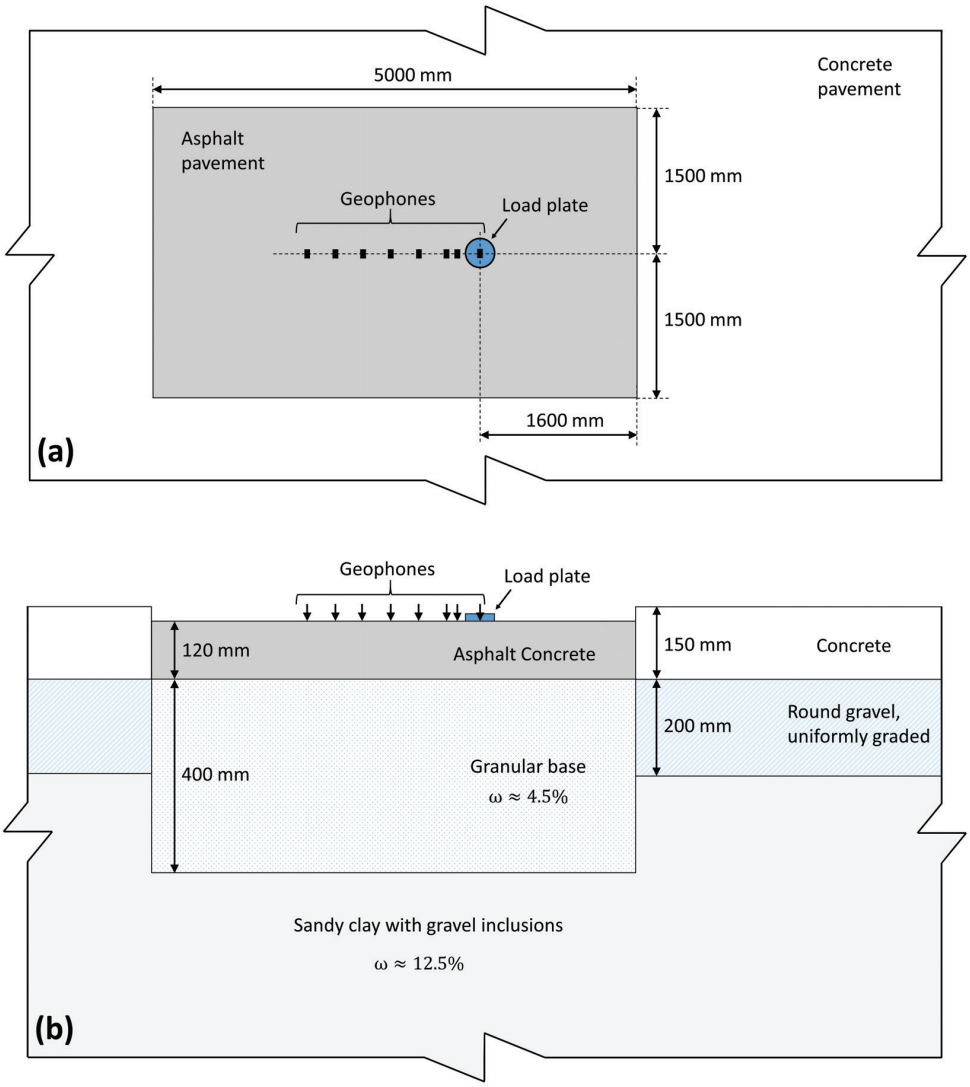

Figure 3: FWD testing area: (a) overhead view, and (b) cross-sectional view.

buffers used. The parameters k_2, k_3 and c_3 are common to all cases and therefore are not affected when the buffer system is manipulated. As can be graphically seen, the model is able to reproduce an FWDs load-time history for any number of buffers and for a range of drop heights and weights. Peak load levels are adequately replicated as well as the overall pulse shape. In some cases it was also possible to simulate the undulation of the load-time history. Such a calibrated model at hand can be utilized to guide FWD operations to generate predefined load-time histories within the device capability range.

After all FWD tests were concluded (in the beginning of 2016) the asphalt pavement section was further investigated to collect more geotechnical characteristics. The investigation reaffirmed the earlier bore log findings and the system layering. It also included vane testing which displayed a trend of increasing shear resistance with depth, from 125 $\mathrm{kN/m^2}$ close to the subgrade surface to 330 $\mathrm{kN/m^2}$ at a depth of 4 m. Moreover, an AC core was extracted from the pavement for subsequent linear viscoelastic characterization. Tests were performed in indirect tension mode under a constant temperature of 20°C. They were analysed assuming a constant Poisson's ratio of 0.35 according to the methodology proposed in Levenberg and Michaeli

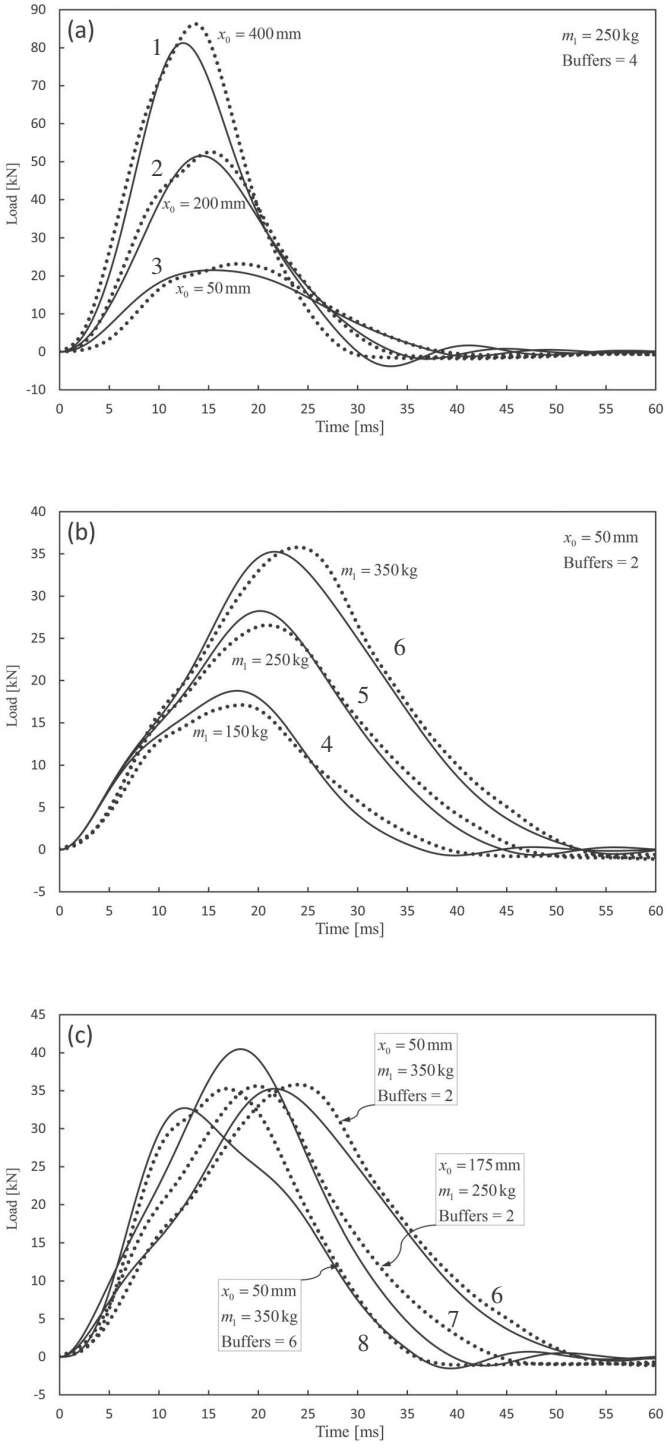

Figure 4: Measured (dotted line) and modelled (solid line) FWD load-time histories

	Number of buffers		
Model element	2	4	6
k_{11} [N/m]	$5.495 \cdot 10^5$	$1.259 \cdot 10^6$	$2.239 \cdot 10^6$
k_{12} [N/m^3]	$5.129 \cdot 10^9$	$1.072 \cdot 10^{10}$	$2.692 \cdot 10^{10}$
c_1 [Ns/m]	$3.802 \cdot 10^3$	$2.692 \cdot 10^3$	$9.333 \cdot 10^1$
k_2 [N/m]	$1.622 \cdot 10^7$		
k_3 [N/m]	$3.090 \cdot 10^3$		
c_3 [Ns/m]	$8.318 \cdot 10^4$		

Table 2: Calibrated values for the realistic FWD loading model in Figure 2.

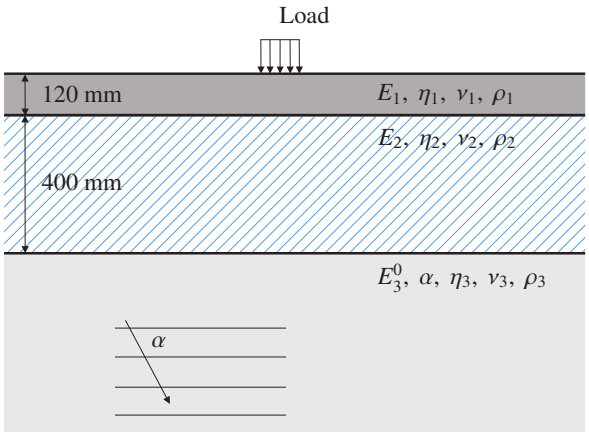

Figure 5: Three layered model of the experimental pavement in Figure 3.

(2013). The experimental information obtained from this geotechnical investigation is utilized hereafter for guiding some modelling choices, and later on for evaluating backcalculation results.

3. Pavement modelling

This section is concerned with the forward modelling of an FWD experiment for subsequent analysis. The aforementioned pavement was represented as a fully bonded three layer system as shown in Figure 5. In general terms, each layer was assumed to be a linear viscoelastic solid governed by a Kelvin-Voigt type of constitutive relation

$$\boldsymbol{\sigma} = \boldsymbol{C}\boldsymbol{\varepsilon} + \eta \boldsymbol{C}\dot{\boldsymbol{\varepsilon}} \tag{6}$$

where $\boldsymbol{\sigma}$ is the stress tensor, $\boldsymbol{\varepsilon}$ and $\dot{\boldsymbol{\varepsilon}}$ are the strain and strain-rate tensors, respectively, $\boldsymbol{C}$ is the constitutive tensor and η denotes material damping. For small strains $\boldsymbol{\varepsilon} = \boldsymbol{\nabla}\mathbf{u} + (\boldsymbol{\nabla}\mathbf{u})^T$ where $\mathbf{u}$ is the displacement vector and $\boldsymbol{\nabla}$ is the gradient operator. Assuming isotropy, the constitutive tensor is governed by two parameters: Young's modulus E and Poisson's ratio ν. In Figure 5, the material properties are identified for each layer by subscripts 1, 2 and 3 referring to AC layer, base layer, and subgrade, respectively.

Based on the vane test results, the modulus of the subgrade layer was assumed to increase as a function of depth; an

expression suggested by Ullidtz (1998) was employed in this connection

$$E_3(z) = E_3^0 \left(\frac{z}{z_0} \right)^{\alpha} \tag{7}$$

where E_3^0 is Young's modulus at the top of the subgrade, z_0 is a reference depth, and $\alpha \geq 0$ is a unitless exponent governing the rate of modulus increase. For the pavement considered in this paper the reference depth is $z_0 = 520\,\text{mm}$ (see Figure 5).

The general equation of motion governing elastic wave propagation in a continuum is given by e.g. Cook et al. (2002)

$$(\boldsymbol{\nabla}^T \boldsymbol{\sigma})^T = \rho \frac{\partial^2 \mathbf{u}}{\partial t^2} \tag{8}$$

where ρ is the mass density.

The system is assumed stress free until the surface of the top layer is exposed to an FWD stress history $\boldsymbol{\sigma}(t)$ uniformly spread over a circle with radius 150 mm. To solve for the resulting dynamic response, the FE approach was employed. For this purpose the equation of motion is multiplied by a virtual displacement field $\tilde{\mathbf{u}}$ followed by integration over the volume and reformulation using the divergence theorem yielding

$$\int_S \tilde{\mathbf{u}}^T \boldsymbol{\sigma} \mathbf{n}_\mathbf{z} dS - \int_V \left[\tilde{\boldsymbol{\varepsilon}}^T \boldsymbol{\sigma} + \rho \tilde{\mathbf{u}}^T \ddot{\mathbf{u}} \right] dV = 0 \tag{9}$$

wherein S and V denote integration over surface area and volume, respectively, and $\mathbf{n}_\mathbf{z}$ is a unit vector indicating the vertical direction of load.. The spatial variation of the actual and the virtual displacement fields are represented by shape functions via the relations

$$\mathbf{u} = \mathbf{N}\,\mathbf{d} \tag{10}$$

$$\tilde{\mathbf{u}} = \tilde{\mathbf{N}}\,\tilde{\mathbf{d}} \tag{11}$$

with $\mathbf{d}$ as the nodal displacements and the shape function matrices $\mathbf{N}$ or $\tilde{\mathbf{N}}$ in the form

$$\mathbf{N} = \begin{bmatrix} N_1 & 0 & N_2 & 0 & \cdots & N_n & 0 \\ 0 & N_1 & 0 & N_2 & \cdots & 0 & N_n \end{bmatrix} \tag{12}$$

Insertion of the shape functions into Equation (9) yields the wave equation in matrix form

$$\mathbf{M}\ddot{\mathbf{u}} + \mathbf{Z}\dot{\mathbf{u}} + \mathbf{K}\mathbf{u} = \mathbf{F}(t) \tag{13}$$

in which $\mathbf{M}$ is the mass matrix, $\mathbf{Z}$ is the damping matrix, $\mathbf{K}$ is the stiffness matrix, $\mathbf{F}(t)$ is the load vector, and $\mathbf{u}$ refers to nodal displacements.

3.1. Numerical implementation

Since the force is circular and uniformly distributed, and all other model components exhibit rotational symmetry about the load axis, the problem is treated as axisymmetric with radial coordinate r, axis of revolution z and circumferential coordinate θ. In this case the displacement field becomes a function of the radial displacement u_r and the axial displacement u_z only, i.e. $\mathbf{u} = [u_r,\, u_z]^T$. The strain-displacement relationships are

$$\varepsilon_r = \frac{\partial u_r}{\partial r} \quad \varepsilon_\theta = \frac{u}{r} \quad \varepsilon_z = \frac{\partial u_z}{\partial z} \quad \gamma_{rz} = \frac{\partial u_r}{\partial z} + \frac{\partial u_z}{\partial r} \tag{14}$$

In array format the strain and corresponding stress is written as

$$\boldsymbol{\sigma} = [\sigma_{rr},\, \sigma_{\theta\theta},\, \sigma_{zz},\, \sigma_{rz}]^T \tag{15}$$

$$\boldsymbol{\varepsilon} = \boldsymbol{\partial}\mathbf{u} = [\varepsilon_{rr},\, \varepsilon_{\theta\theta},\, \varepsilon_{zz},\, \gamma_{rz}]^T \tag{16}$$

The strain-displacement operator is expressed by

$$\boldsymbol{\partial} = \begin{bmatrix} \partial/\partial r & 0 \\ 1/r & 0 \\ 0 & \partial/\partial z \\ \partial/\partial z & \partial/\partial r \end{bmatrix} \tag{17}$$

Since no variation occurs in the circumferential direction, the volume dV of an element can be expressed as

$$dV = 2\pi r dA \tag{18}$$

where dA is the cross-sectional area of an element. Similarly, the element of surface dS can be expressed as

$$dS = 2\pi r ds \tag{19}$$

where ds denotes an element length. Insertion of (18) and (19) into (9) defines the matrices in (13) as

$$\mathbf{M} = 2\pi \int_A \rho \tilde{\mathbf{N}}^T \mathbf{N}\, r\, dr\, dz \tag{20}$$

$$\mathbf{Z} = \eta\, 2\pi \int_A \tilde{\mathbf{B}}^T \mathbf{C}\mathbf{B}\, r\, dr\, dz \tag{21}$$

$$\mathbf{K} = 2\pi \int_A \tilde{\mathbf{B}}^T \mathbf{C}\mathbf{B}\, r\, dr\, dz \tag{22}$$

where $\mathbf{B} = \boldsymbol{\partial}\mathbf{N}$ denotes the strain displacement matrix and the constitutive matrix $\mathbf{C}$ for layer i is given by

$$\mathbf{C} = \frac{E_i}{(1+\nu_i)(1-2\nu_i)} \begin{bmatrix} 1-\nu_i & \nu_i & \nu_i & 0 \\ \nu_i & 1-\nu_i & \nu_i & 0 \\ \nu_i & \nu_i & 1-\nu_i & 0 \\ 0 & 0 & 0 & (1-2\nu_i)/2 \end{bmatrix} \tag{23}$$

Finally, the load vector in Equation (13) is given by

$$\mathbf{F}(t) = 2\pi \int_A \boldsymbol{\sigma}(t) \boldsymbol{n}_z r ds \tag{24}$$

3.2. Mesh generation

This section presents a method for generating a finite element mesh that balances computational time and numerical accuracy. For the problem at hand, waves generated at the surface propagate into the medium while decaying with increasing distance from the source. Accordingly, an efficient mesh capturing this behaviour consists of placing the smallest elements near the load center and then placing larger and larger elements as distance increases. Such a domain discretization approach is presented in Figure 6(a).

More specifically, the mesh generation strategy devised herein was governed by four user-selected parameters: a minimum element size Δx_{min}, a maximum element size Δx_{max}, a growth rate parameter G_R, and an overall domain size $\bar{d}_0$. From an initial (minimum) element size Δx_{min} the elements double in size as a function of their distance from the load center, $\bar{d}$, until reaching a maximum element size Δx_{max}. From this point onward, until the domain boundary $\bar{d}_0$ is approached, the size of all elements remain Δx_{max}. In this scheme the G_R parameter controls the 'rate' at which element size is doubled. All four mesh controlling parameters are illustrated graphically in Figure 6(b) which depicts element side length Δx versus distance $\bar{d}$. Additional restrictions in the mesh generation, not presented in the figure, were applied to ensure that none of the elements cross the interface between two adjacent layers and that the load is distributed over an integer number of elements.

The overall domain size $\bar{d}_0$ was chosen to be large enough such that the waves generated at the load cannot reach the boundary during the analysis period. A domain size $\bar{d}_0 = 9500$ mm was found adequate in this respect given that an FWD drop test is a relatively short-lasting event, of the order of 80 ms in duration. The other mesh parameters were selected such that computed deflections are accurate to within $\pm 1\,\mu$m which is equivalent to the level of deflection accuracy measured by a typical FWD device. Accordingly, the final generation values were: $\Delta x_{min} = 19$ mm, $\Delta x_{max} = 625$ mm, and $G_R = 0.06$.

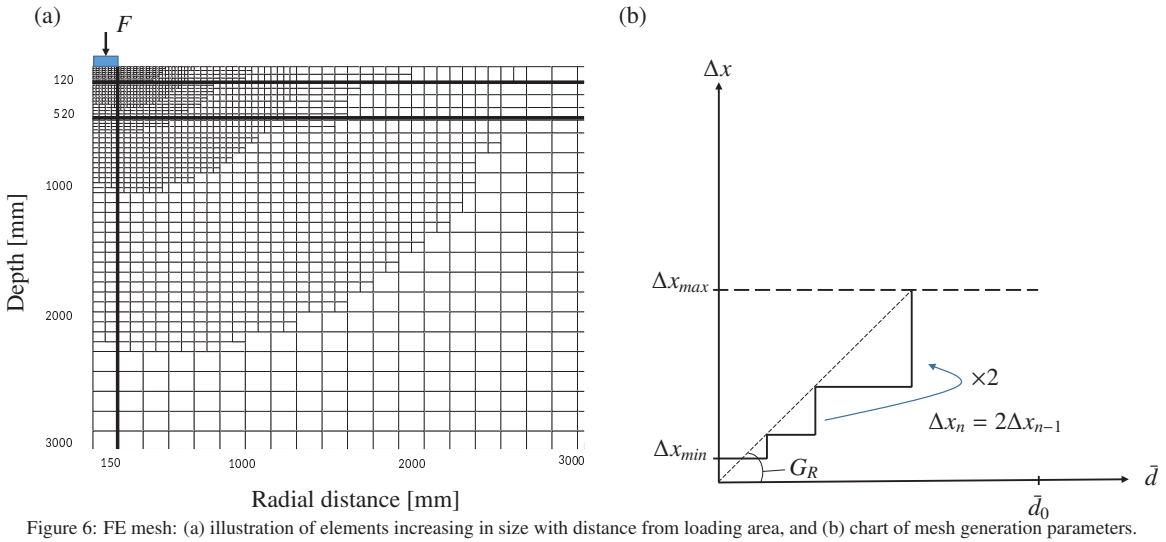

Figure 6: FE mesh: (a) illustration of elements increasing in size with distance from loading area, and (b) chart of mesh generation parameters.

Layer	ν [−]	ρ [kg/m^3]	E [MPa]	η [ms]	α [-]
1	0.35	2400	[1000 – 7000]	[0.05 – 5.00]	-
2	0.35	2000	[150 – 750]	[0.05 – 5.00]	-
3	0.35	1800	[25 – 180]	[0.05 – 5.00]	[0.0 – 3.0]

Table 3: Layer properties of the model pavement. ρ and ν are prefixed during backcalculation. E, η and α are adjustable during backcalculation within the defined ranges.

4. Backcalculation

Backcalculation was employed here to best estimate the constitutive parameters of the pavement layers in Figure 5 under the different loading conditions in Figure 4. For this purpose the measured load histories were used as an input to the numerical formulation for generating model deflections. Applied load was discretized with a constant interval of 0.5 ms into 60-120 time steps depending on the load pulse duration. The level of mismatch between the modelled and measured deflections was subsequently minimized by adjusting the unknown parameters. As shown in Figure 5 there are a total of 13 constitutive parameters that govern the model response. As is commonly accepted, $\nu_1 - \nu_3$ and $\rho_1 - \rho_3$, were prefixed before performing the backcalculation; their chosen values are included in Table 3. The seven remaining parameters: E_1, E_2, E_3^0, $\eta_1 - \eta_3$ and α were kept adjustable for the backcalculation algorithm. As means of confining the solution search space, this latter set of sought parameters was bound to within the ranges defined in Table 3.

4.1. Minimization approach

An objective function, ψ_{ab}, was defined to express the difference between modelled and measured deflections as follows

$$\psi_{ab} = \sqrt{\frac{1}{b-a+1}\frac{1}{M}\sum_{k=a}^{b}\sum_{j=1}^{M}(D_k(t_j) - d_k(t_j))^2} \tag{25}$$

where $D_k(t_j)$ is the deflection measured by the k^{th} geophone at discrete times $t_j = t_1, t_2, ..., t_M$ and $d_k(t_j)$ is the corresponding deflection produced by the numerical model. The geophones included in the objective function are $k \in [a; b]$ where a and b are geophone numbers; $a = 1, 2, ..., 8$ and $b = 1, 2, ..., 8$ with $b \geq a$. As can be seen, ψ_{ab} represents the discrepancy between model and measurement across the entire simulated time for a group of sensors $a, a + 1, ..., b$ out of the entire available set. The overall goal of the backcalculation process is to minimize ψ_{18} within a total analysis duration t_M. As means of ensuring

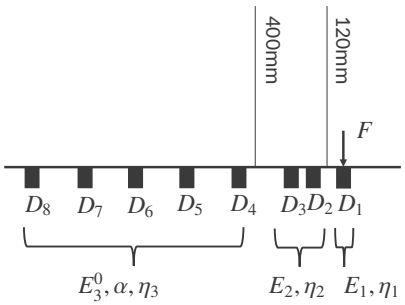

Figure 7: Grouping of geophones based on pavement layering for sequential minimization of ψ_{18} (see Equation (25)).

convergence into physically realistic results t_M was chosen to include the first part of the recorded deflections - about 60%. This analysis period covers the deflection rise-time, the peak, and a small portion of the decrease. This truncation is done because deflection recordings are known to be less reliable as time progresses (due to integration of geophone data), producing unrealistic deflection tails (e.g., Uzan, 1994).

Another effort for ensuring convergence into meaningful results involved performing the minimization in stages. Initially, parameter seed values were randomly chosen within the bounds given in Table 3. Then (Stage I) ψ_{48} was minimized with respect to E_3^0, α and η_3; in Stage *II* ψ_{23} was minimized with respect to E_2 and η_2; and in Stage *III* ψ_1 was minimized with respect to E_1 and η_1. This bottom-up approach is based on an engineering intuition that associates more distant geophone readings with deeper layer properties. The rational for the specific choices in the above stages is illustrated in Figure 7 in which the pavement layering is superposed over the geophone array configuration. Accordingly, $d_4 - d_8$ were deemed more sensitive to the subgrade parameters, $d_2 - d_3$ were deemed more sensitive to the base parameters and d_1 most closely associated with the AC parameters.

A gradient based method was used for the three stages with gradients calculated using a backward finite difference. In each stage the minimization process was restarted several times with new seed values to broaden the search space for a solution. The optimal (minimal) objective functions in stages I, II and III were denoted ψ_{48}^{min}, ψ_{23}^{min} and ψ_{11}^{min}. These entities were employed in the Min-Max sense (Osyczka, 1978) to perform an overall minimization for ψ_{18} with respect to all adjustable parameters (simultaneously). A general purpose unconstrained derivative-free nonlinear optimization algorithm was employed for this final minimization step (Stage IV) (for more details consult Madsen (2016)). A pseudo code for the above described procedure is presented in Algorithm 1.

5. Results

Included and discussed in this section are backcalculation results. First presented is the fitting obtained between modelled and computed deflection histories for Test 6 and for Test 8. Both drops were similar in terms of peak force but different with respect to pulse duration (see Figure 4 and Table 1). Geophone measurements and calculated deflections are superposed in Figures 8 and 9. The dashed vertical line indicate the analysis duration in each case (i.e., t_M). As can be graphically seen in both figures, the FE model was able to capture and reproduce both the magnitude and the overall shape of the deflections. Essentially similar charts were obtained for the other tests.

Presented in Table 4 is a summary of the backcalculation results for the eight FWD drops. For the AC layer, E_1 was found in the range 3065-4561 MPa and η_1 was found in the range of 2.1-4.1 ms. For the base layer, E_2 was found in the range 246-307 MPa and η_2 in the range of 0.6-1.1 ms. Finally, for the subgrade, E_3^0 was found in the range 99-153 MPa, η_3 in the range of 0.9-2.0 ms, and α in the range of 1.0-1.4. The latter corresponds well to the vane test results which indicated increasing stiffness profile for the subgrade. Across the different analysed cases, the coefficient of variation for the moduli values was relatively small, about 10%, while the coefficient of variation for the damping parameters was nearly three times larger. Overall, the backcalculated values are well within the bounds defined in Table 3 and are therefore reasonable from an engineering standpoint.

As means of investigating the influence of different FWD load-time histories on backcalculated outcomes, three charts were prepared (see Figure 10) by combining data from Table 1 with data from Table 4. Figure 10(a) cross-plots moduli values and pulse duration across all peak loads, Figure 10(b) depicts moduli values versus peak loads across all pulse durations, and Figure

Algorithm 1 Backcalculation approach

Random initial guess of $X_0 = [E_1, E_2, E_3^0, \alpha, \eta_1, \eta_2, \eta_3]$
Stage I:
minimize $\underset{x_I=[E_3^0,\alpha,\eta_3]}{\psi_{48}(x_I)}$ subject to $LB \leq x_I \leq UB$
Continue minimization until $\Delta\psi_{48}(x_I) \leq 10^{-6}$
Stage II:
Given result of stage I:
minimize $\underset{x_{II}=[E_2,\eta_2]}{\psi_{23}(x_{II})}$ subject to $LB \leq x_{II} \leq UB$
Continue minimization until $\Delta\psi_{23}(x_{II}) \leq 10^{-6}$
Stage III:
Given result of stage I and II:
minimize $\underset{x_{III}=[E_1,\eta_1]}{\psi_1(x_{III})}$ subject to $LB \leq x_{III} \leq UB$
Continue minimization until $\Delta\psi_1(x_{III}) \leq 10^{-6}$
Calculate weights for overall optimization
Stage IV:
Given result of stage I, II and III as initial guess:
minimize $\underset{x_{IV}=[E_1,\eta_1,E_2,\eta_2,E_3^0,\eta_3,\alpha]}{\psi_{18}(x_{IV})}$ using Matlab's fminsearch function
Continue minimization until $\Delta\psi_{18}(x_{IV}) \leq 10^{-6}$

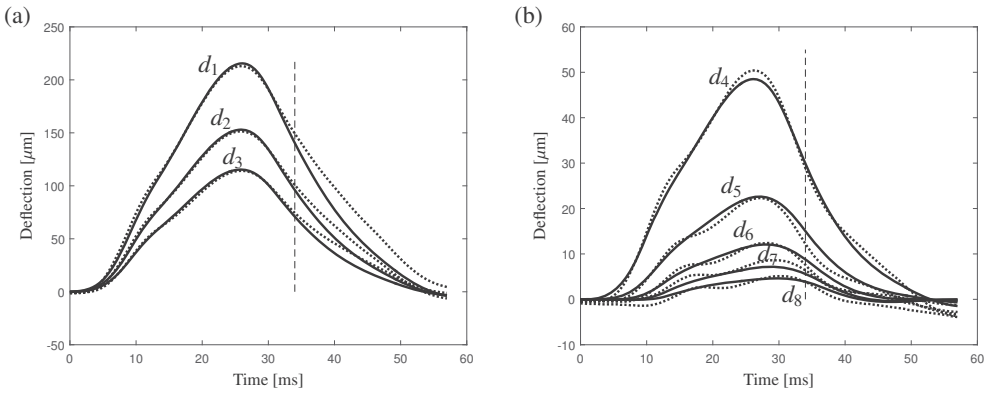

Figure 8: Measured (dotted) and modelled (solid) deflection histories for Test 6 (see Table 1).

10(c) cross-plots damping values and pulse duration. As can be graphically noticed in the charts, all backcalculated parameters are influenced by the FWD load-time history. Specifically, the AC modulus (E_1) displays slight decrease with increasing pulse duration and slight increase with increasing peak load levels. Similar sensitivity, but with opposite trends, is exhibited by the base and top of subgrade moduli (E_2 and E_3^0). As for layer damping, it appears that the AC is most sensitive, showing an increase in value with increase in pulse duration. Subgrade damping is slightly increasing with increase in pulse duration while base damping seem to be uncorrelated with FWD pulse duration.

The results of the investigation indicate that different FWD load-time histories produce different backcalculation parameters for the tested pavement. The trends appearing in the above discussed charts are not random in nature. In other words, the optimized values of the model parameters had to be readjusted to best match the measured deflections depending on the pulse attributes. If backcalculation parameters differ when FWD pulse attributes are allowed to vary, then essentially new constitutive information is exposed under the different loading situations.

A possible enhancement of the model is a better representation of AC viscoelasticity. To further demonstrate this point

	AC properties		Base properties		Subgrade properties			
Test	E_1 [MPa]	η_1 [ms]	E_2 [MPa]	η_2 [ms]	E_3^0 [MPa]	α [-]	η_3 [ms]	ψ_{18}^{min} [μm]
1	4211	2.5	247	0.6	99	1.2	2.0	3.6
2	4250	2.2	238	1.1	126	1.2	1.1	2.2
3	3786	2.8	272	0.9	151	1.1	0.9	1.0
4	3065	3.3	307	0.8	129	1.4	1.3	0.8
5	3492	4.1	285	0.8	143	1.1	1.9	1.0
6	3953	4.5	262	0.7	150	1.0	2.0	1.4
7	4085	3.1	246	1.1	153	1.0	1.5	1.5
8	4561	2.1	254	0.9	138	1.2	1.0	1.5
Mean	3925	3.1	264	0.9	136	1.2	1.5	1.6
CV [%]	12.0	29.0	8.7	22.2	13.2	8.3	33.3	56.3

Table 4: Backcalculation resutls with different load-time histories.

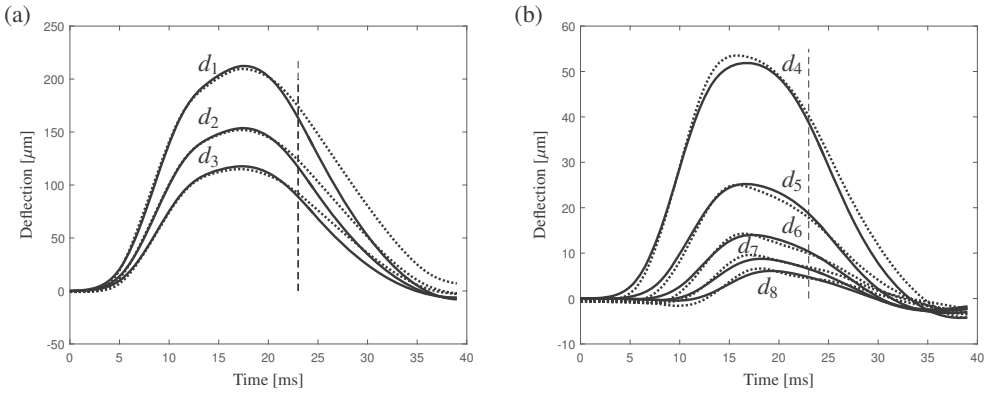

Figure 9: Measured (dotted) and modelled (solid) deflection histories for Test 8 (see Table 1).

consider the creep compliance function of the AC layer based on the Kelvin-Voigt representation

$$D_1(t) = \frac{1}{E_1}\left(1 - e^{-t/\eta_1}\right) \tag{26}$$

In Figure 11 this equation is plotted for all eight backcalculated results E_1 and η_1 from Table 4 (solid lines). Under the log-log scale, the resulting curves appear concave. Also included in this Figure is the laboratory-measured creep compliance function (dotted line), which is sigmoidal in nature and plots as an S shaped curve. The two functions are dissimilar and only match in the average sense within time-frame considered.

6. Conclusion

The aim of this paper was to investigate the influence of different FWD load-time histories on backcalculation outcomes. An experiment was designed and carried out wherein an asphalt pavement was exposed to a variety of FWD tests within a short time. The tests differed from one another by the device settings in terms of drop height, dropped mass, and number of buffers. Initially, a new semi-analytic FWD loading model was shown to match well the diverse load-time histories generated in the experiment. Then, a new dynamic FE code was applied to backcalculate layer properties from the deflection histories.

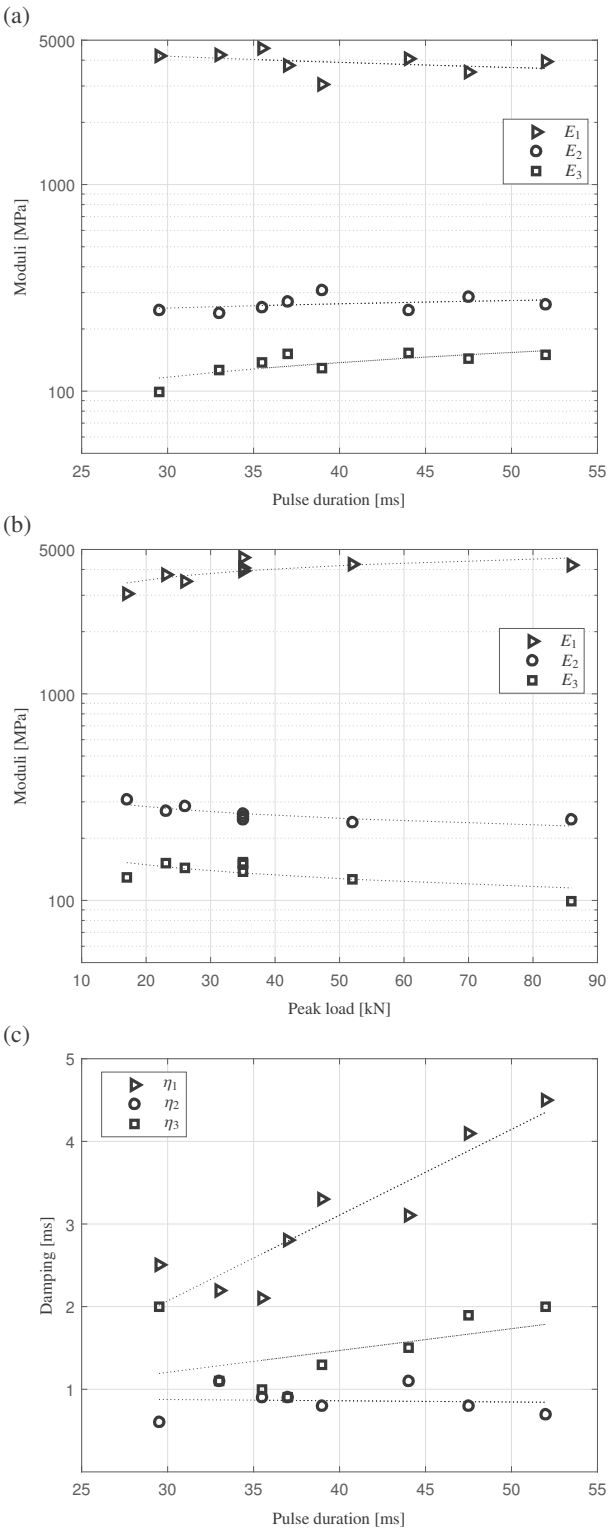

Figure 10: Backcalculation results: (a) moduli versus pulse duration, (b) moduli versus peak load, and (c) damping versus pulse duration.

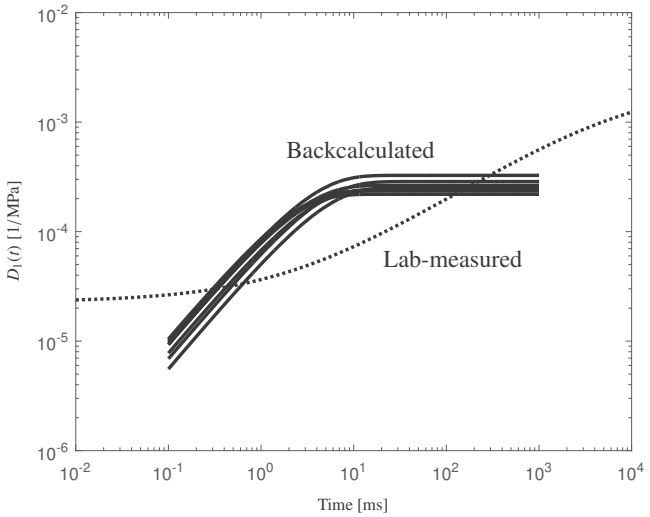

Figure 11: Creep compliance from FWD backcalculation (solid) and laboratory testing (dotted).

As a result of these two separate efforts, and despite the fact that one single pavement was experimentally investigated, some general conclusions can be made.

When an advanced dynamic FE pavement model is employed, combined with careful steps to ensure correct parameter convergence, backcalculated properties appear sensitive to the FWD pulse features. This finding suggests that modelling complexity is too simplified. The rational here is that if a more intricate pavement model is employed then inferred properties based on any deflection test will remain identical when backcalculated. Possible enhancements in this connection can include: better viscoelastic representation of the AC layer, allowance for nonlinear stress-dependent behaviour of the base and subgrade, and incorporation of anisotropic response. The downside here is that more unknown constitutive parameters will need to be evaluated.

However, the observed parameter sensitivity to FWD pulse attributes essentially means that new constitutive information is exposed under the different loading situations. Consequently, opportunity arises for increasing the modelling complexity as suggested above because a wider calibration set becomes available to reliably infer the new/additional constitutive parameters. To achieve this, the testing should first include diverse load-time histories, and the analysis should require simultaneous matching of all deflection histories. The new semi-analytic loading model that was offered herein for simulating FWD pulses should be utilized in this connection. Once calibrated, it can serve as an engineering tool to guide FWD operators in producing any load-time history of choice within the device capability range.

Consequently, based on the findings from this study, whenever advanced pavement layer characterization is sought, it is recommended that: (i) experimental attention be placed on generating diverse FWD pulse histories, and (ii) backcalculation be performed by the requirement to match all deflection histories, across all tested cases, simultaneously.

7. Acknowledgements

This work is supported by the Innovation Fund Denmark through the grant 'High-Speed Pavement Assessment Tool for Better and Safer Roads'. The FWD experiments were conducted in collaboration with Dynatest and laboratory testing was carried out with help from Matteo Pettinari at the Danish Road Directorate.

References

ASTM (2015). Astm d4694 - 09, standard test method for deflections with a falling-weight-type impulse load device. Technical report.

Bush, A. J., Baladi, G. Y., and society for testing, A. (1989). *Nondestructive Testing of Pavements and Backcalculation of Moduli*. ASTM.

Chatti, K., Ji, Y., and Harichandran, R. (2004). Dynamic time domain backcalculation of layer moduli, damping, and thicknesses in flexible pavements. *Transportation Research Record: Journal of the Transportation Research Board*, 1869:106–116.

Cook, R., Malkus, D., and Plesha, M. (2002). *Concepts and applications of finite element analysis*. Wiley.

Lee, H. S. (2014). Viscowave - a new solution for viscoelastic wave propagation of layered structures subjected to an impact load. *International Journal of Pavement Engineering*, 15(6):542–557.

Levenberg, E. and Michaeli, N. (2013). Viscoelastic characterisation of asphalt-aggregate mixes in diametral compression. *Road Materials and Pavement Design*, 14(S1):105–119.

Lukanen, E. O. (1992). Effects of buffers on falling weight deflectometer loadings and deflections (with discussion). *Transportation Research Record*, 1355:37–51.

Madsen, S. S. (2016). *Dynamic Modeling of Pavements with Application to Deflection Measurements*. PhD thesis, Technical University of Denmark, Kgs. Lyngby.

Osyczka, A. (1978). Approach to multicriterion optimization problems for engineering design. *Computer Methods in Applied Mechanics and Engineering*, 15(3):309–333.

Quintus, H., Bush, A. I., Baladi, G., and for Testing, A. S. (1994). *Nondestructive Testing of Pavements and Backcalculation of Moduli: Se- cond Volume*. ASTM.

Sebaaly, B., Davis, T. G., and Mamlouk, M. S. (1985). Dynamics of falling weight deflectometer. *Journal of Transportation Engineering*, 111(6):618–632.

Shao, K.-Y., Roesset, J. M., and Stokoe, K. H. (1986). *Dynamic Interpretation of Dynaflect and Falling Weight Deflectometer Tests on Pavement Systems*. Center for Transportation Research, University of Texas at Austin.

Tayabji, S., Lukanen, E., testing of pavements, N., STP., A., and for Testing, A. S. (2000). *Nondestructive testing of pavements and backcalculation of moduli. 3*. ASTM.

Ullidtz, P. (1998). *Modelling Flexible Pavement Response and Performance*. Polyteknisk Forlag.

Ullidtz, P. and Stubstad, R. N. (1985). Analytical-empirical pavement evaluation using the falling weight deflectometer. *Transportation Research Record*, pages 36–44.

Uzan, J. (1994). Dynamic linear back-calculation of pavement material parameters. *Journal of Transportation Engineering-asce*, 120(1):109–126.

Uzan, J. and Lytton, R. L. (1990). Analysis of pressure distribution under falling weight deflectometer loading. *Journal of Transportation Engineering*, 116(2):246–250.

DTU Mechanical Engineering
Section of Solid Mechanics
Technical University of Denmark

Nils Koppels Allé, Bld. 404
DK-2800 Kgs. Lyngby
Denmark
Phone (+45) 4525 4250
Fax (+45) 4593 1475
www.mek.dtu.dk
ISBN: 978-87-7475-462-6

DCAMM
Danish Center for Applied Mathematics and Mechanics

Nils Koppels Allé, Bld. 404
DK-2800 Kgs. Lyngby
Denmark
Phone (+45) 4525 4250
Fax (+45) 4593 1475
www.dcamm.dk
ISSN: 0903-1685